Computational and Experimental Studies of Microstructure-Scale Porosity in Metallic Fuels for Improved Gas Swelling Behavior

Project 14-6472

Final Report (FY 2017)

PI: Paul Millett, University of Arkansas
Co-PI: Sean McDeavitt, Texas A&M University
Co-PI: Chaitanya Deo, Georgia Institute of Technology
Co-PI: Robert Mariani, Idaho National Laboratory

SCOPE (FROM PROPOSAL)

This proposal will investigate the stability of bimodal pore size distributions in metallic uranium and uranium-zirconium alloys during sintering and re-sintering annealing treatments. The project will utilize both computational and experimental approaches. The computational approach includes both Molecular Dynamics simulations to determine the self-diffusion coefficients in pure U and U-Zr alloys in single crystals, grain boundaries, and free surfaces, as well as calculations of grain boundary and free surface interfacial energies. Phase-field simulations using MOOSE will be conducted to study pore and grain structure evolution in microstructures with bimodal pore size distributions. Experiments will also be performed to validate the simulations, and measure the time-dependent densification of bimodal porous compacts.

OBJECTIVES (FROM PROPOSAL)

The objective of this proposal is to scientifically investigate, using closely-integrated computational simulations and experiments, the underlying microstructural mechanisms that govern the relative resistance to densification exhibited by a bimodal pore size distribution in uranium alloy fuels. This research will advance the field in three ways: (i) we will confirm that such stability occurs in metallic uranium and its alloys (as previously demonstrated in UO_2), (ii) we will monitor, in detail, the complex microstructural morphology that occurs in high temperature annealing including the evolution of grain structure and pore distribution using multi-scale simulation and experiments, and (iii) we will develop a predictive approach to specifically design metallic fuel microstructures for optimal swelling resistance and fission gas retention. Developing this understanding will potentially lead to a new metallic fuel design paradigm that will enable better management of both swelling and fission gas release. Such knowledge will also be applicable to the design of accident tolerant fuels.

1. Overview

This project involves both computational and experimental research techniques, and the accomplishments for each institution are given below. The project supported three graduate students, one at each institution, as well as some PI/coPI summer time.

1.1 University of Arkansas:

The Univ. of Arkansas group (PI Millett and graduate student Bruce Berry) lead the effort to simulate metallic fuel sintering behavior using the MOOSE/MARMOT simulation environment. Student Bruce Berry has performed a parametric simulation study focused on the relationship between sintering rate and the distribution of pore size. Berry presented a poster presentation at the 2016 Materials Research Society (MRS) Fall meeting in Boston, Ma, and has published one journal paper titled "Phase-Field Simulations of the Impact of Bimodal Pore Size Distributions on Solid-State Densification" in the Journal of Nuclear Materials, vol. 491, pages 48-54. This published paper is available in **Appendix A** of this report. All data and numerical results from this portion of the project can be found there. Student Bruce Berry graduated with a MSME degree in 2017 from the University of Arkansas, and is now pursuing a PhD at the University of Central Florida. His MSME thesis is available in **Appendix B**.

1.2 Georgia Tech:

The Georgia Tech group (co-PI Deo and graduate students David Carroll and Alex Moore) lead the effort to atomistically simulate metallic Uranium interfacial properties relevant to sintering. The U-Zr phase diagram was investigated with atomistic methods. A semi-empirical Modified Embedded Atom Method (MEAM) is used in conjunction with molecular dynamics (MD) and Monte Carlo (MC) simulations to investigate the properties and equilibrium configurations of the high temperature body-centered-cubic (bcc) uranium-zirconium (U-Zr) alloys. All results from the GT group are compiled in a sub-report available in **Appendix C** of this report.

1.3 Texas A&M Updates:

The TAMU group (co-PI McDeavitt and graduate students Clifford Hart and Yesenia Salazar) lead the effort to experimentally fabricate porous metallic fuel compacts and investigate their re-sintering behavior. Alloy samples of U-10Zr and copper have been prepared by powder metallurgical methods. Both mono-modal and bi-modal pore distributions will be prepared for comparative evaluations of microstructural stability. Currently, we have prepared mono-modal pore distributions. Methods to create bi-modal porosity may include pressing and sintering coarse powders and mixtures of fine and coarse powders at moderate temperatures (e.g., 900°C to 1000°C) to evaluate the best path to achieve the desired microstructure.

The metal U and U-Zr powders have been prepared by hydriding and dehydriding and by rotary electrode atomization; both methods have been demonstrated at Texas A&M University. The initial powders were prepared from depleted uranium metal stock on-hand from the Y-12 National Security Complex but additional

uranium source material will be purchased; there is approximately 1 kg of depleted U rods in the current inventory and a purchase order for an additional 2 to 4 kg is in preparation.

The hydride-dehydride method is carried out inside an inert atmosphere glovebox (Fig. 4a). Very fine uranium metal powder flakes (~1 to 10 μm) are produced by exposing acid-washed uranium metal slugs (Fig. 4b) to flowing Ar-5%H_2 at 235°C. The metal forms uranium hydride powder (UH_3) via an exothermic reaction. After sufficient reaction time, the process vessel is evacuated and the temperature is raised to 325°C to remove the hydrogen via thermal decomposition. The uranium powder product (Fig. 4c) has very fine flake morphology with a nominal particle size on the order of 1 to 5 μm with larger agglomerates (Fig. 4d).

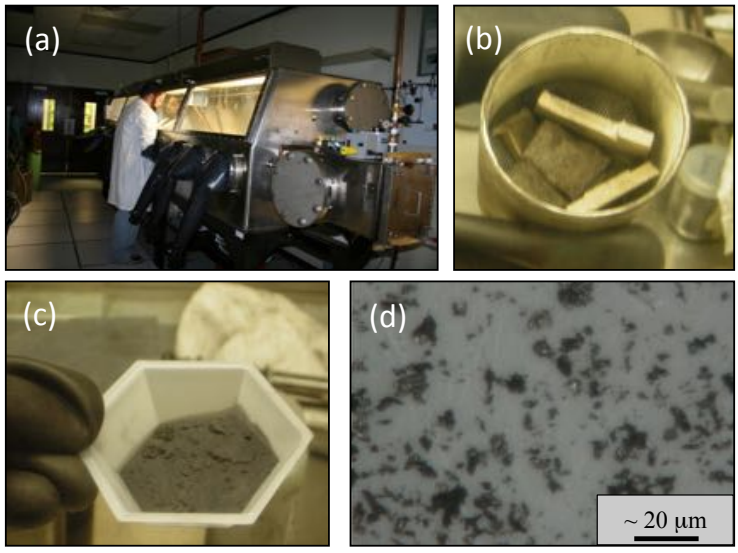

Figure 4. Images describing the production of uranium powder using hydride-dehydride process: (a) inert atmosphere glovebox with furnace, (b) Uranium metal slugs before hydriding (in glovebox), (c) Uranium metal powder produced from the slugs in Fig. 4b, and (d) optical image of hydride derived powders.

For coarse microspheres, atomization of U and U-10Zr rods (nominally 0.7 to 1.0 cm diameter) has been prepared using a rotating electrode system (Figs. 5a and 5b). The system operates by rotating the source rod at 10,000 to 20,000 rpm while arc melting the tip. Figures 5a and 5b show the system as it was being developed – it is now fully operational. Figures 5c and 5d show a set of U-10 Zr microspheres produced using this system. With sieving, multiple size distributions may be culled from the raw powder product. It is expected that microspheres on the order of 75 to 150 μm diameter will be used for this study; finer spheres may be added to optimize the packing density for the final sintered pellets.

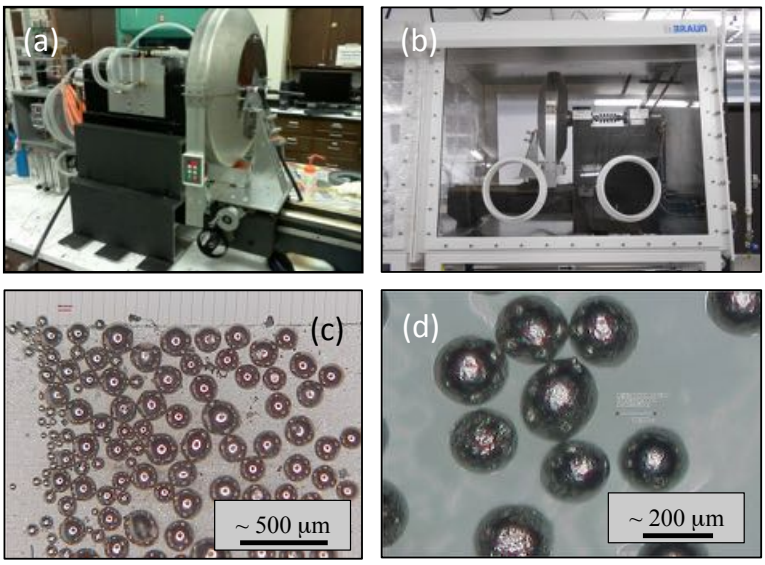

Figure 5. Images describing the production of uranium mirospheres: (a) rotating electrode system, (b) system installed in glovebox, (c) U-10Zr microspheres (low mag.), and (d) U-10Zr microspheres (higher mag.).

The material processing gloveboxes, rotating electrode system (RES), sintering furnace, and metallurgical examination equipment have all been installed in the D.L. Houston Building at the Texas A&M University. A new trolley/lift system was added to the RES to enable mounting and dismounting the catch pan within the glovebox. Figure 6 shows some images from the initial uranium powder production runs from this quarter.

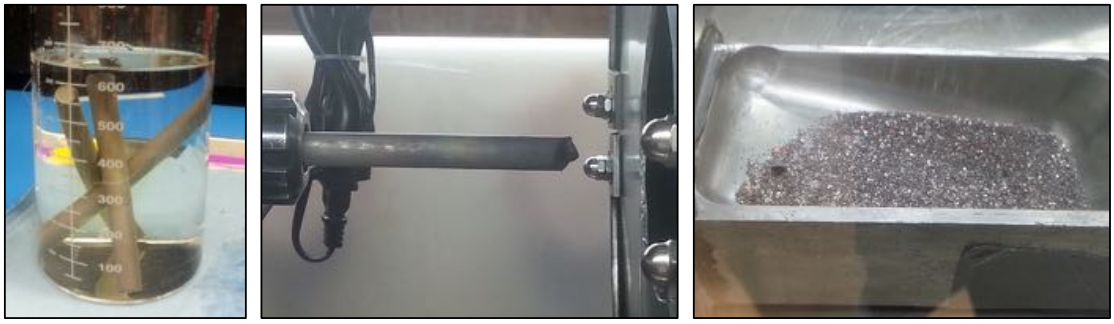

(a) (b) (c)

Figure 6. Uranium rods used to make powder at different stages in the process: (a) during acid treatment to remove surface oxidation, (b) after partial melting for powder production, and (c) powder in catch pan after production (not sieved to remove large pieces).

It was decided to use copper powder as a parallel demonstration method to perfect the pellet pressing and processing methods. Copper is a face-centered cubic metal, but should represent a reasonable cold surrogate for sintering uranium in the gamma phase (body centered cubic). Initial test copper pellets were fabricated using

a supply of available powder in the lab (Figure 7). Copper spheres with measurements between 300-425 µm were used. The following is an example of the pressing process: (1) 4.646 g of copper powder was poured into a cylindrical double-action dye. The height of the powder in the dye before pressing was 1.5 cm (0.586 in). (2) Pressure is applied up to 1.8 metric tons, (3) the pressed pellet was measured to be 0.94 cm (0.356 in) in height and 0.95 cm (0.374 in) in diameter with a mass of 4.544 g (~0.1 g loss). The initial pellets have been friable and have not been sintered. A set of copper powders have been ordered with certified chemical specifications and small, medium, and large particle sizes.

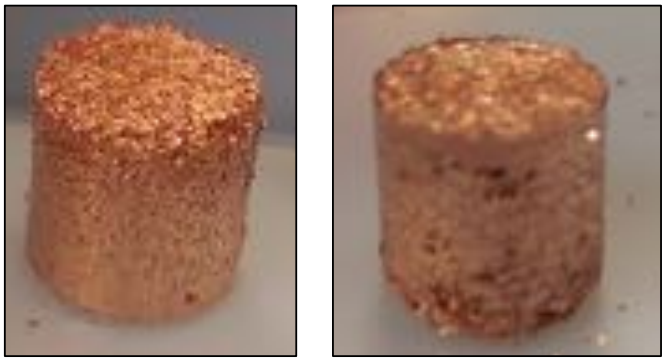

Figure 7. Pressed copper pellets made to shake down the powder pressing tools for metal sample production.

The TAMU team has now successfully fabricated compaction samples from U and U-10%Zr particles using compaction sintering at 900 ^{o}C. Images of the U-Zr compaction specimens are shown below in Figures 8 and 9.

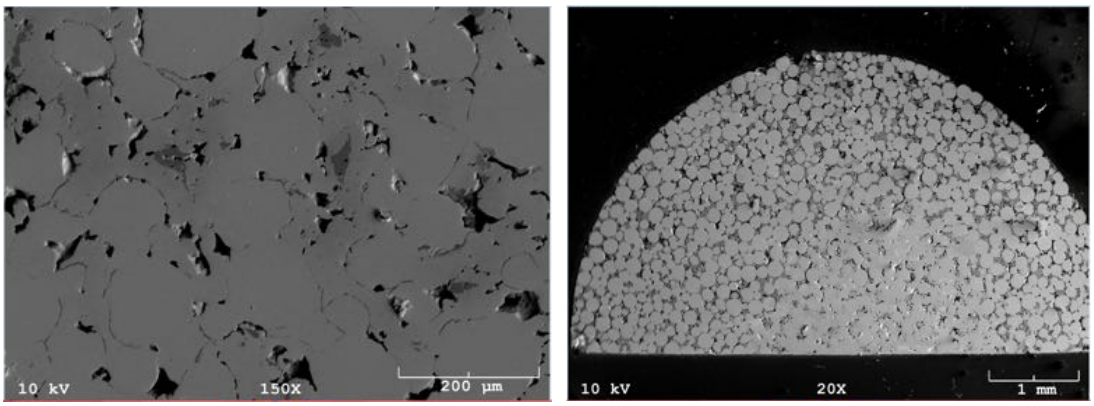

Figure 8. SEM images of U-10%Zr fuel pellets fabricated from particle compaction sintering for 10 hours at 900 ^{o}C. The left image shows a larger view of the variation in density with radius.

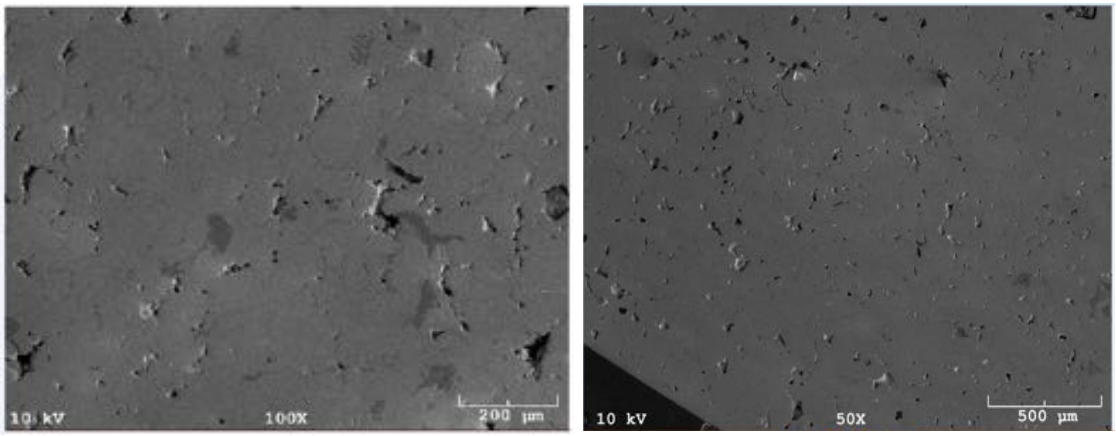

Figure 9. SEM images of U-10%Zr fuel pellets fabricated from particle compaction sintering for 12 hours at 900 ^{o}C.

Appendix A

Journal of Nuclear Materials 491 (2017) 48–54

Contents lists available at ScienceDirect

Journal of Nuclear Materials

journal homepage: www.elsevier.com/locate/jnucmat

Phase-field simulations of the impact of bimodal pore size distributions on solid-state densification

Bruce E. Berry, Paul C. Millett*

University of Arkansas, 204 Mechanical Engineering Bldg., University of Arkansas, Fayetteville, AR 72701, United States

ARTICLE INFO

Article history:
Received 22 February 2017
Received in revised form
19 April 2017
Accepted 26 April 2017
Available online 29 April 2017

ABSTRACT

The densification behavior of a porous body subjected to elevated temperature is relevant to many nuclear fuel performance metrics. The diffusional processes that govern such densification occur on microscopic length scales, and depend on the type of material and the nature of the porosity. In this study, we explore how bimodal pore size distributions impact diffusion-based densification relative to monomodal pore sizes for a given overall value of porosity. We utilize a Cahn-Hilliard phase-field model implemented with the MOOSE framework to simulate densification evolution with a range of overall porosities and a variety of porosity distributions between small and large pores. The results demonstrate that bimodal porosity can resist densification to a much greater extent than monomodal porosity. These findings have implications for the microstructural design of metallic nuclear fuels, in which an initial, bimodal porosity may resist early-stage densification and therefore provide collection sites for fission gases, thus reducing in-pile fission gas swelling.

1. Introduction

Oxide nuclear fuels (UO_2) have historically been the preferred formulation for use in power reactors throughout the world [1]. They were first used in 1955 by the Shippingport PWR, and are employed in many designs currently in operation. These forms typically offer satisfactory chemical and radiological behavior [2] and have been studied in depth as a result of their development and use. Unfortunately, their classification as a ceramic material results in lackluster thermal performance, in addition to a relatively low fuel atom density in comparison to other formulations. Additionally, UO_2's thermal conductivity is significantly influenced by temperature, and tends to decrease with temperature up to around 1600° C [3]. This imposes additional safety margins during design and operation to account for the occurrence of power and reactivity transients.

Metallic fuel forms have been used in a variety of research reactors, including EBR-II. This formulation offers considerable improvement in thermal conductivity and heavy metal density. They are of particular interest in liquid-metal-cooled fast reactors under current development, in part due to their chemical compatibility with sodium as a coolant [4]. Their application as next-generation fuels for advanced reactor designs has been a topic of on-going research [5].

Metallic fuel is generally fabricated by casting techniques; however, powder metallurgy followed by sintering processes are currently being developed [6–9], and the capacity to produce cylindrical pellets at a range of size scales has been demonstrated. Powder compaction/sintering fabrication allows one to intentionally insert a degree of porosity within the fuel. The pellets are pressed into a "green" compact and fired at temperature to induce grain coarsening and coalescence until a workpiece with the desired characteristics is produced [10]. The final workpiece is polycrystalline but chemically bonded, no longer being composed of many disparate particles. Sintering schedules for U-Zr have been produced that allow for the specification of an initial average grain size [11].

The in-pile performance of metallic nuclear fuel is commonly degraded by the onset of volumetric swelling driven by the formation and growth of fission-gas bubbles [12], which has prompted research programs focused on mitigating in-pile fuel swelling using compositional and/or microstructural design approaches [12–14]. We are interested in exploring the possibilities of an intentional porosity distribution in metallic fuels that may serve the purpose of collecting fission gas elements during service to minimize the in-

* Corresponding author.
E-mail address: pmillett@uark.edu (P.C. Millett).

http://dx.doi.org/10.1016/j.jnucmat.2017.04.050
0022-3115/

pile formation of large gas bubble structures that result in volumetric swelling. Such an initial porosity, however, would need to resist early-stage densification during service.

Maier et al. [15] experimentally investigated oxide fuel consisting of a unique porosity configuration in which the dominant pore sizes were bimodally distributed, and compared their densification rates with similar samples that contained only monomodally sized pores. Samples were sintered and measured for porosity loss. It was shown that the bimodal configuration exhibited heightened resistance to porosity loss. As the experiment did not involve the effects of radiation, the result was a sample with slower rates of densification.

In this study, we wish to further explore the nature of densification in porous solids subjected to isothermal annealing, and reproduce the results of Maier et al. [15] using numerical simulations. We consider the specific mechanisms associated with the relative resistance to shrinkage exhibited by bimodal pore structures, and seek to model this phenomenon in the hopes of predicting other microstructures that result in improved performance of nuclear fuel bodies. Fabrication routes for fuel pellets with this bimodal configuration are currently being pursued in conjunction with this work. The primary technique is described in Ref. [16], and utilizes "burnable" compounds that are added to the fuel powder before pressing. A pre-sintering step destroys these "pore formers", leaving large vacant regions within the green compact. The size of these regions can be controlled to produce bimodal pore configurations.

A variety of simulation methods can be utilized to study sintering processes, and many examples exist in the literature [17–20]. Sintering involves a combination of processes that co-contribute to the overall evolution of grain structure and density. One of the primary mechanisms to be considered is the bulk diffusion of vacancies to the surface of the system, which leads to the shrinkage of pores and the reduction of internal surface area. Two primary techniques exist that can simultaneously evolve pore surfaces and the concurrent diffusion of vacancies through a solid body: the Monte-Carlo-based Potts [21] models and phase-field models. We have used a phase-field model, as described below.

2. Methods

In this study, a phase field model [22–24] was used to provide a mathematical description of the densification process. Here, a continuously varying field variable ϕ is utilized to represent a porous body, and a Cahn-Hilliard (CH) equation [24] is solved in space and time to evolve the system. The CH equation takes the form:

$$\frac{\partial \phi}{\partial t} = \nabla \cdot M \nabla \frac{\delta F}{\delta \phi}. \tag{1}$$

Here, F is a free energy functional that describes the relative formation energies of a multi-phase system, which in this case includes solid fuel material and porous cavities, and M is a mobility parameter associated with ϕ. The variable ϕ represents the local density of the fuel and is defined as $\phi = c_U - c_V$ where c_U is a fractional concentration of uranium atoms on an assumed underlying lattice and c_V is a fractional concentration of vacancies on the same lattice. Assuming $c_U + c_V = 1$ (i.e. a monoatomic uranium alloy) reduces the degrees of freedom associated with concentration to one, e.g. ϕ. Within a porous fuel body, a local value of $\phi = 1$ corresponds to a solid region of fuel, whereas a value of $\phi = -1$ corresponds to a pore region within the fuel. The parameter ϕ transitions between values of $+1$ and -1 at free surfaces within the system. In our model, we adopt a polynomial form for the free energy functional:

$$F(\phi) = \int_V \left(\phi^4 \big/ 4 - \phi^2 \big/ 2 + \kappa \left| \nabla \phi \right|^2 \right) dV, \tag{2}$$

where the first two terms on the right-hand side define a double-well function that maintains a two-phase structure. The third term represents the interfacial free energy that arises at the phase boundaries.

To solve Eq. (1), we utilized the Multi-physics Object Oriented Simulation Environment (MOOSE) framework. MOOSE is a software package designed to provide scientists with a highly scalable and user-friendly interface to a variety of finite element meshing and solution tools [25,26]. This study required the development of a routine within MOOSE that could accept pore locations and sizes within the domain and apply appropriate initial values to the order parameter, ϕ.

Three different initial porosities of 4%, 6%, and 8% (corresponding to 96%, 94%, and 92% theoretical density (*TD*), respectively) were utilized. For each level of porosity, we further divided the porosity by assigning a certain number of small pores with diameter of 5 h and large pores with diameter of 50 h (h being the computational grid spacing). This ratio of large pore diameter to small pore diameter is roughly the same as that studied in the experiments of Maier et al. [15]. The relative fraction of porosity associated with small pores compared to the total porosity is represented by a parameter χ:

$$\chi = \frac{A_S}{A_S + A_L} \times 100 \tag{3}$$

where A_S is the total area of small pores and A_L is the total area of large pores.

A stochastic approach was utilized to generate the initial configuration of pores within a large, circular fuel body cross section. Pores are randomly assigned positions within the fuel body, as well as a diameter based on the partially constructed system's current χ value. If the current χ is below the target χ, a small pore is required, and the candidate pore assigned the small value of 5 h. If the system is above the target χ, a large pore is required, and the candidate pore assigned the value of 50 h. For each candidate pore addition, we insure that it does not overlap with any previously placed pore. To this effect, we iterate through the entire list of previously placed pores; a single overlap in area is sufficient to disqualify the candidate pore. Fig. 1 shows example pore configurations used in this work (see Table 1).

The simulations are two-dimensional, thus porosity volumes are calculated as areas. By assuming an isotropic value for the mobility, we induce symmetry in the z-axis of the system. Thus, the pores in our system are columnar rather than spherical. Nevertheless, two-dimensional studies are expected to provide comparable results to three-dimensional studies, with significantly less computational expense.

A rectilinear and uniform computational grid with 4096×4096 nodes was used, with a grid spacing of $h = 0.27$ reduced length units. The initial diameter of the fuel body is 1024 reduced units. The simulation time step was assigned a value of $\Delta t = 1.0$ reduced time units with a reduced mobility of $M = 16$ and $\kappa = 16$, and the systems were evolved for 50,000 time steps, or until concentration gradients were vanishing, signifying near steady-state conditions.

With the various values of χ, we can represent monomodal or bimodal pore configurations. A value of $\chi = 100$ represents a monomodal structure consisting of only small pores, whereas a value of $\chi = 0$ also represents a monomodal structure, but

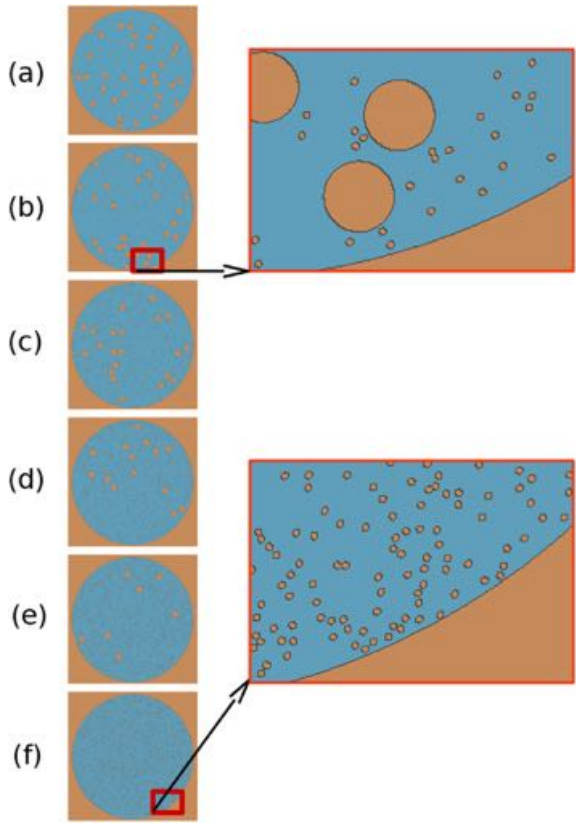

Fig. 1. Examples of the porosity configurations tested for an overall initial theoretical density of 92% and (a)–(f) corresponding to $\chi = 0$, 20, 40, 60, 80, and 100, respectively. The zoomed views show the relative sizes of the small and large pores for the bimodal configurations, and also indicate the range of small pore quantity as χ increases. There is some variation in the average distance between large pores for the different configurations. This variation was not found to contribute significantly to the densification rates in our analyses. The possibility of pore overlap is precluded according to the generation algorithm, and occasional verification by hand is performed to certify such.

Table 1
Initial porosity characteristics.

Parameter	Range
TD(%)	92,94,96
χ(%)	0,20,40,60,80,100

consisting of only large pores. At $\chi = 20$, 40, 60, and 80, we produce bimodal microstructures. In the results presented below, for the bimodal configurations, we specifically focus on $\chi = 40$ and 60, as these values represent the most even distribution of porosity between small and large pore categories. For each combination of ϕ and *TD*, five independent samples are simulated to provide a statistical sampling. All error bars presented indicate one standard deviation, calculated from within the five repeated runs for each configuration.

We seek to measure the relative densification rates of the various configurations as an indication of their performance in fuel applications. To accomplish this, we probe the values of ϕ along a few diameter cross-cuts of each configuration, recording the outermost transition to a pore region to determine the total cross-sectional area of the porous body at each time step. In the absence of fission-gas production, we expect all configurations to experience shrinkage as porosity is lost to the environment. Thus, configurations with the lowest rates of area change will be considered superior in the respect that such porosity may persist in the fuel long enough to collect a build-up of fission-gas elements.

3. Results

Fig. 2 gives a qualitative comparison of the porosity evolution within three porous bodies with values of $\chi = 0$, 60, 100 for an initial *TD* of 92%. Snapshots are taken of each configuration at equivalent simulation times to compare their relative evolution. Visually, $\chi = 60$ appears to follow the behavior of $\chi = 0$ (i.e. monomodal porosity with only large pores). For each system, most pores near the outer surface of the body quickly shrink and disappear as their vacancies migrate to the outer surface. On the other hand, pores in the interior persist for longer durations. After sufficient simulation time, all pore space is eliminated and the fuel is considered to be 100% dense. This occurs very early for $\chi = 100$, as the small pores possess a high surface area, and therefore dissolve quickly, creating large vacancy diffusion gradients (in the solid material) pointing towards the outer surface. In addition, it is interesting to note that $\chi = 60$ and $\chi = 0$ experience minor random deformations of the outer fuel body surface, whereas this behavior is not exhibited at $\chi = 100$. This is the result of large pores, initially located near the outer edge of the fuel, that upon shrinkage and disappearance, cause minor displacements of the fuel surface. The effect is not visually observable for smaller pores.

Figs. 3–5 provide data on the densification behavior versus time for various values of χ and initial theoretical density. Porosity distributions of $\chi = 100$ experience rapid porosity loss in all cases. This pore distribution can be considered typical of traditional sintering/compaction fabrication routes. Rapid vacancy transport to the outer fuel surface results in considerable reduction of the fuel body cross-sectional area. In our simulations, the fuel reached 100% density early in time and further evolution produced no changes. On the other hand, the densification of $\chi = 0$ was considerably slower, owing to much larger initial pore sizes. For this case, shrinkage continued up to the simulation limit, albeit at low rates.

Interestingly, bimodal porosities of $\chi = 40$ and $\chi = 60$ exhibited similar behavior to that of $\chi = 0$ in most cases, despite the significant fraction of smaller pores placed in the initial structure. At a theoretical density of 96% (see Fig. 5), the porosity loss of $\chi = 60$ was even slower than $\chi = 0$. At early times in the densification

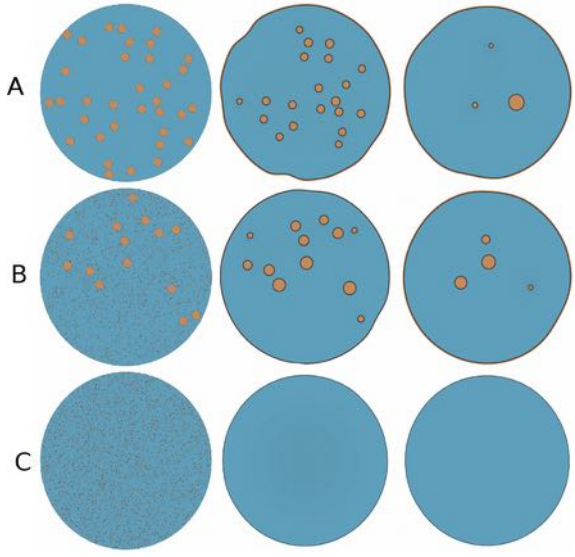

Fig. 2. Snapshots illustrating porosity evolution during densification for (a) $\chi = 0$, (b) $\chi = 60$, and (c) $\chi = 100$, at three different times: (left column) T = 0, (middle column) T = 20, and (right column) T = 80. The overall theoretical density here is 92%.

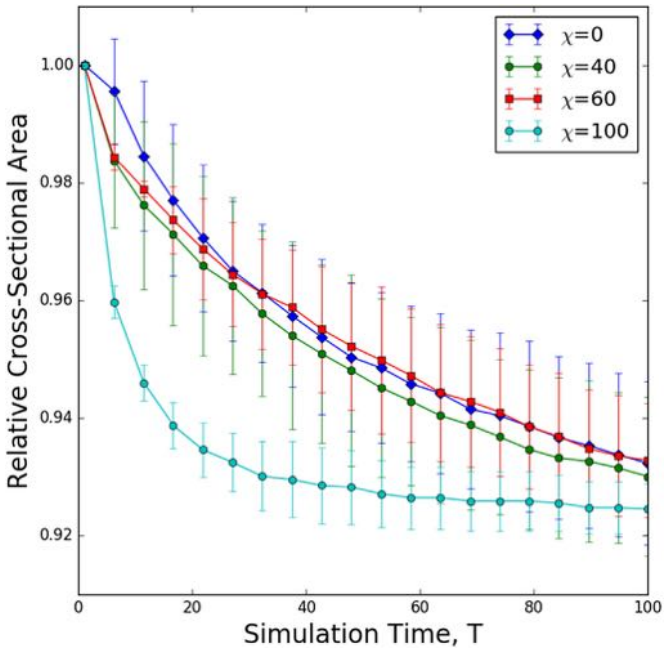

Fig. 3. Densification rates for samples with $TD = 92\%$ represented as the relative change in total cross-sectional area. Systems with bimodal pore distributions evolved similarly to the system with only large pores.

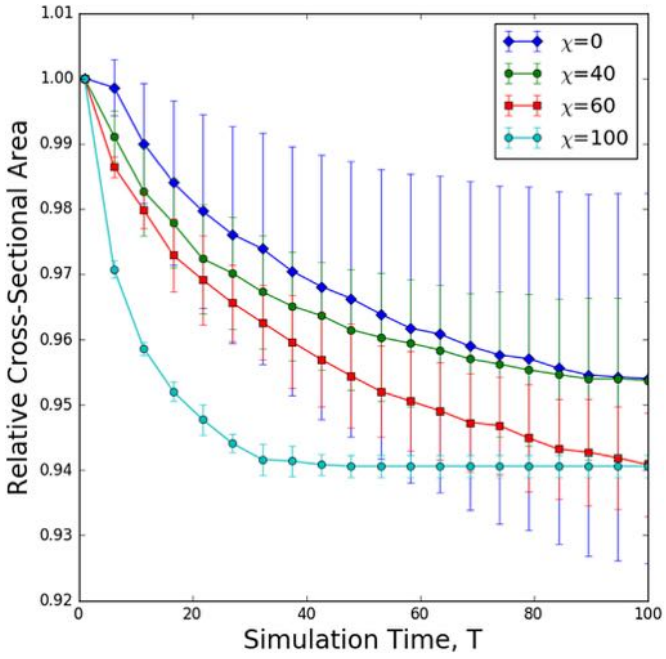

Fig. 4. Densification rates for samples with $TD = 94\%$ represented as the relative change in total cross-sectional area. The basic trends are the same as for the $TD = 92\%$ data, but larger error bars make exact determinations difficult.

process, bimodal porosities did experience early loss rates that were higher than the $\chi = 0$ case. This is the result of the rapid loss of small pores that are distant from large pores and relatively close to the outer fuel surface. Small pores in the center of the body also dissolve, however the associated vacancies from these internal pores do not have direct diffusion pathways to the outer surface. Rather, they feed larger pores within the solid body. This phenomenon retards the shrinkage process of the larger pores and

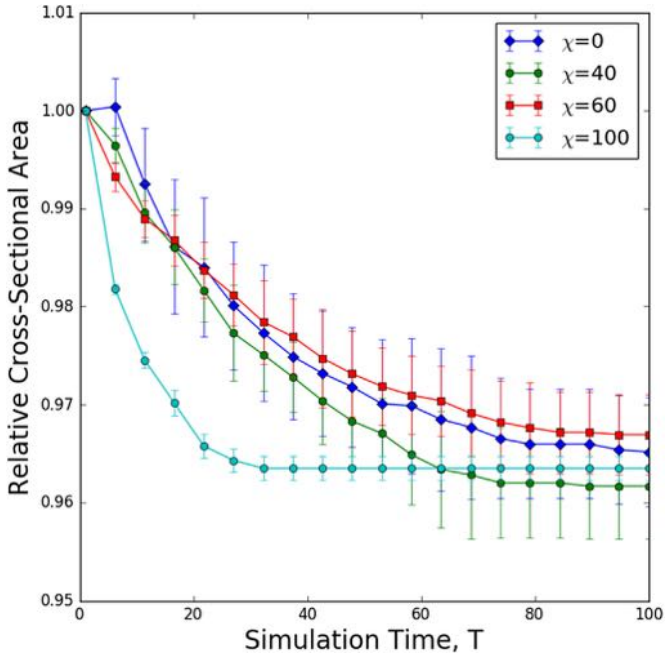

Fig. 5. Densification rates for samples with $TD = 96\%$ represented as the relative change in total cross-sectional area. At this overall porosity level, the $\chi = 60$ case exhibited the slowest densification rates.

seems to delay the densification process.

In some cases, with values of $\chi = 40$, 60, and 100, intermediate-sized pores form from a re-nucleation process in vacancy-dense regions. These pores are capable of temporary growth, consuming nearby vacancies that would otherwise migrate to the outer surface. Of course, over longer time periods, these intermediate-sized pores also shrink and disappear, as the pore's curvature (which determines its stability) will always be higher than that of the overall system. This will result in their elimination when under sintering conditions. However, their persistence for moderate time scales is also a contributing factor for the delayed densification exhibited by bimodal pore distributions.

4. Discussion

Large pores inhibit the long-range diffusion of vacancies to the outer surface of the fuel body. The release of vacancies initially associated with small pores, and their migration to the outer surface, is the primary mechanism by which early shrinkage occurs, with the large pores persisting for much longer time periods. Therefore when considering the short-term kinetics of the structure, we are concerned with the behavior of the small pores and their associated vacancies. Vacancies migrate to the outer surface via concentration gradient driving forces. As small pores dissolve and release vacancies into the fuel matrix (see Fig. 6 for snapshots at very early simulation times), the average vacancy concentration in the solid material increases temporarily to values as high as $c_v = 0.040$, as shown in Figs. 7–9. The system seeks to evolve to a configuration that both minimizes the interfacial energy by minimizing surface area, and simultaneously minimizing excess vacancy concentrations in the solid regions by gradient-driven diffusion processes. Systems with exclusively small pores ($\chi = 100$) quickly eliminate internal surface area and consequently cause a rapid increase in the internal vacancy concentration (as well as a rapid increase in the concentration gradients). These gradients result in a high flux of vacancies to the outer surface, and system

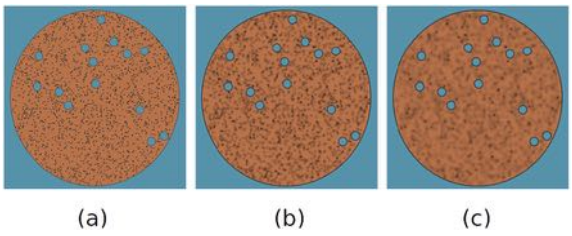

Fig. 6. With a reduced timestep of dt = 0.001, the diffusion of vacancies from the small pores becomes evident (the darker regions indicate a higher vacancy concentration). As vacancies diffuse throughout the system, the darker regions disappear. Figures from TD = 92% and $\chi = 60$.

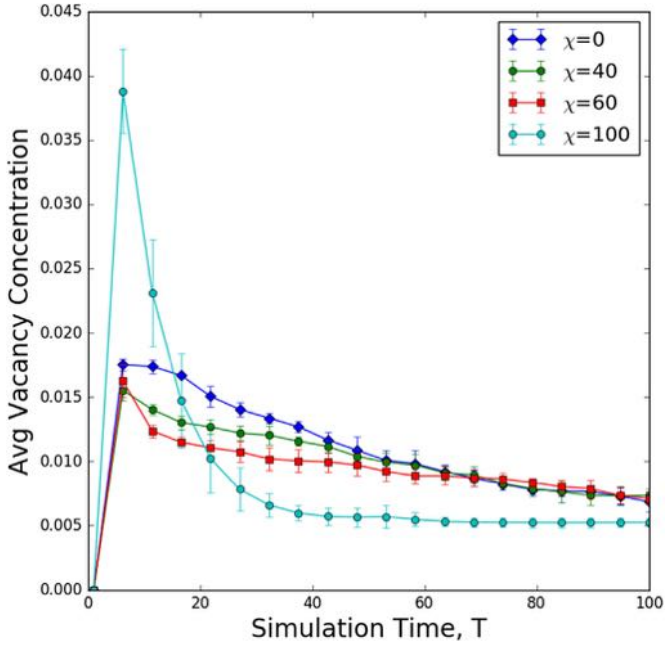

Fig. 7. The average vacancy concentration within the solid material throughout annealing for various χ values at an initial *TD* = 92%. The large (and more stable) pores act as intermediate collection sites for vacancies that are released from small pores that shrink and dissolve at early times, the consequence of which is a reduced spike in vacancy concentration at early annealing times.

densification is completed early. The introduction of large pores interrupts the pathways taken by the internal vacancies originally associated with small pores. Because of their larger size (and therefore lower surface curvature), the large pores can persist for much longer, with some pores temporarily growing as excess vacancies migrate to their surfaces. While the large pores will eventually be eliminated, the overall shrinkage rate is considerably reduced. Systems with large pores show reduced concentration gradients, and are slower to eliminate those gradients via vacancy transport.

It is unsurprising that in comparing configurations with $\chi = 40$ and $\chi = 60$, the second configuration showed faster early kinetics, owing to the greater initial quantity of small-pore vacancies. The long-term behavior, however, shows little variation when considering these two configurations. Indeed, the configuration with no initial small pores ($\chi = 0$) is also very similar in its long-term behavior. This suggests that small-pore vacancies are quickly absorbed at the relevant collection sites (large pores and the system's outer surface), and that the long-term behavior is entirely determined by how the large pores evolve in isolation. From a fuel design perspective, eliminating small pores during the compaction/

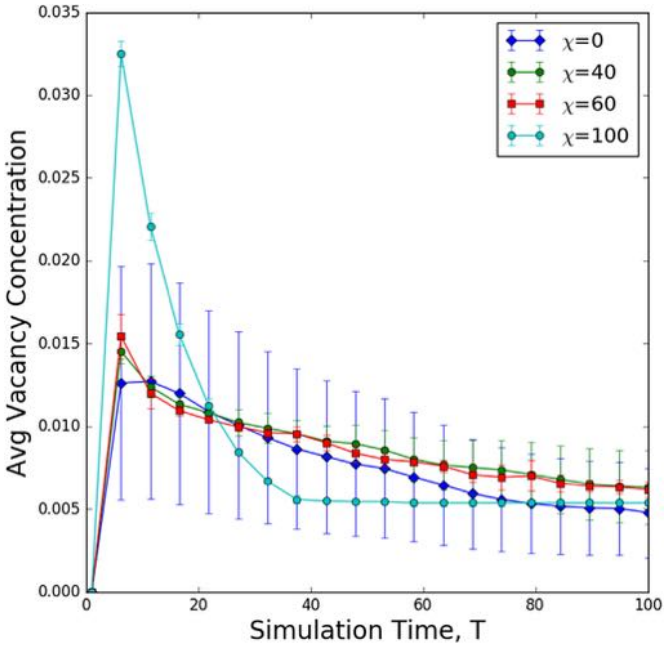

Fig. 8. At *TD* = 94%, high variance is exhibited in the $\chi = 0$ case. The bimodal configurations, however, demonstrated good precision, and were consistent with the trends observed in other initial TD values.

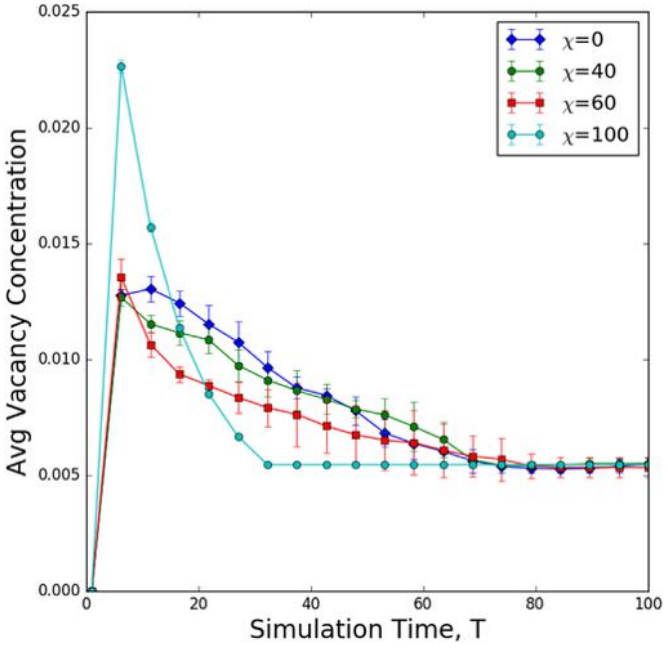

Fig. 9. Vacancy concentration at an initial TD of 96%. The behavior shows little departure from that of Fig. 7.

sintering fabrication process is difficult, but the introduction of large pores can be deliberately achieved. It is envisioned that the quantity and size of these large pores can be fine tuned to produce a material with a desirable long-term densification behavior.

Although there is consistency in the general trends at a variety of *TD* values, some variation is observed. In particular, the *TD* = 94% case shows a higher level of variance than either of the other configurations. The random placement of pores has the effect that some large pores are placed near the outer surface, in addition to

each other. In cases where this happens more frequently, behavior that departs from the "typical" case for that group can be expected. This effect would be expected to diminish for systems with much larger outer diameters relative to the large pore diameters, as would be the case for macroscopic fuel pellets. In the configurations used here, the ratio of the diameter of the fuel pellet to the diameter of the larger pores is not as high as an actual pellet, which is a consequence of the computational limitations when solving the Cahn-Hilliard model. Therefore, we give additional consideration to the system size utilized; specifically, does the relatively small ratio of system size to large pore size contribute to the positive effect observed for the bimodal cases? Simulation of a physically realistic system is intractable, as countless pores would be required to produce the initial porosity desired, and an excessive number of finite elements required to resolve them. In lieu of this, we can parameterize the system size while keeping the pore sizes constant. We execute three total fuel diameters (D): the original (D = 1024), a half-sized system (D = 512), and a double-size system (D = 2048). These cases are tested at $TD = 92\%$ for the $\chi = 0$, 60, and 100 cases. Fig. 10 displays the results for the larger diameter and Fig. 11 displays results for the smaller diameter. We observe that the smaller system densifies more rapidly in all configurations, in contrast to the larger system where densification is slowed. This result is intuitive, as the average distance vacancies must travel to escape the solid body is modified. Of greater interest is the fact that the comparative performance of the bimodal and monomodal configurations is consistent for each system size considered herein. Although the ratio of pore diameters to pellet diameter in our largest system is still not comparable with macroscopic fuel bodies such as those investigated by Maier et al. [15], this parametric analysis improves our confidence that the results are not highly system-size dependent.

In our attempt to reproduce the experimental results of Maier et al. [15], two features stand out. We observe that systems with exclusively small pores exhibit the greatest rates of porosity loss, in agreement with the results described in Ref. [15]. Although the bimodal structures contain a significant fraction of small pores, their behavior is markedly different from the monomodal case. This was also observed by Maier et al. In our study, we implemented the same size ratio between large and small pores as Maier et al., and we explored a variety of pore distributions. Although the current results should not be quantitatively compared with Maier's experiments, we do view this study as qualitatively valuable, in that it illuminates the mechanism by which these bimodal structures resist densification. This knowledge allows further, more focused studies on microstructures that may exhibit superior in-reactor performance.

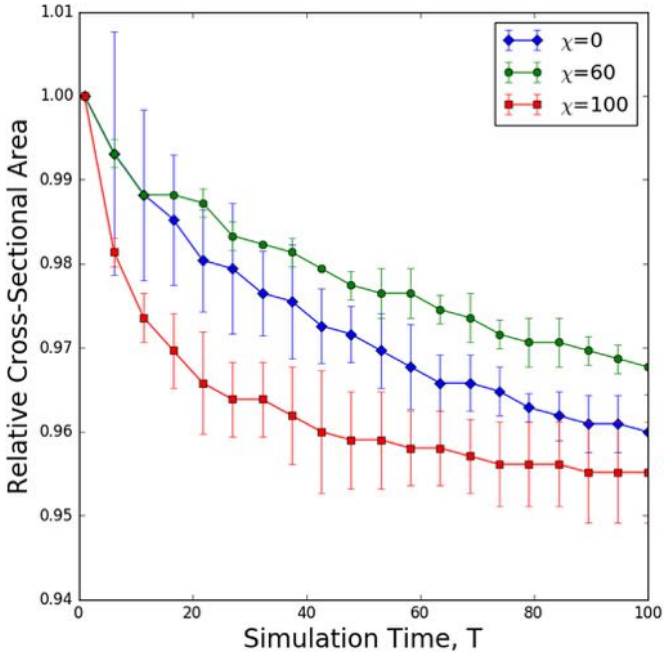

Fig. 10. Doubling the fuel pellet diameter (D = 2048), the bimodal configuration continues to outperform the monomodal case. In fact, the bimodal configuration displays even greater resistance to densification than the $\chi = 0$ case. The parameterization of the system size reduces concern that the bimodal advantage is derived from the system size selected in the study. Data shown at $TD = 92\%$.

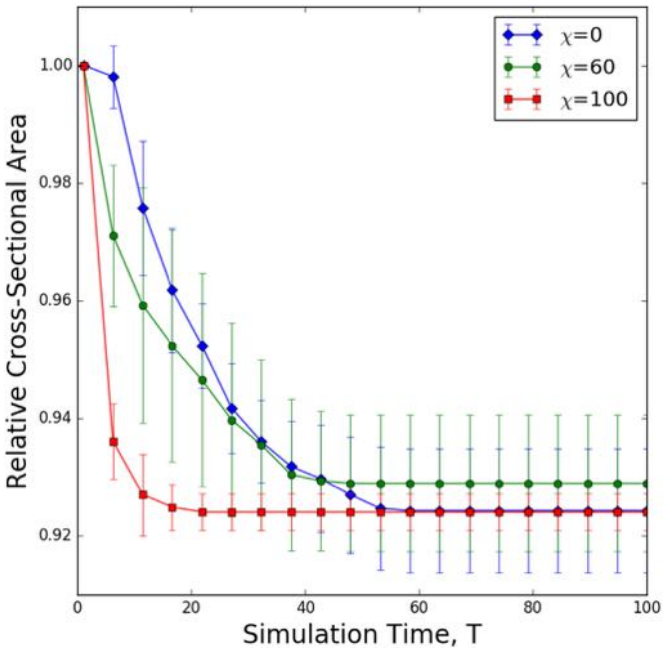

Fig. 11. At half the original system size (D = 512), the bimodal effect is again observed. In the case of such a small system, porosity loss is more rapid for all configurations, due to the reduced distance required for vacancies to migrate outward. Data shown at $TD = 92\%$.

5. Conclusion

This study has investigated the behavior of fuel densification with a variety of monomodal and bimodal porosity configurations. We have shown that bimodal configurations resist initial porosity loss when exposed to annealing conditions as compared to small monomodal pore distributions for exactly the same overall porosity. This resistance is observed over a variety of initial porosity levels and for multiple pore size ratios. We attribute this behavior to the energetic competition between minimizing internal surface area versus minimizing excess vacancy concentrations in the solid material. For a fixed porosity, the presence of both small and large pores lead to a mutual interaction with respect to their coarsening behavior, and the ultimate transport of internal vacancies to the outer fuel surface. In this paper, internal microstructural features such as grain boundaries and other crystalline defects were not considered, however their presence and their interactions with migrating vacancy fields may influence the kinetics of the observed processes.

A computational model has been developed that describes these porosity configurations. The model is flexible in that other future

configurations of interest can be readily considered. The implementation in MOOSE permits a highly scalable approach that can handle systems of considerable complexity and size. Future work will address the inclusion of fuel-cladding interface effects and how changing gap conditions will alter the morphology evolution of the fuel. The effects of in-situ pore creation as a result of in-pile irradiation will also be considered.

Acknowledgements

The authors acknowledge financial support from the Department of Energy under NEUP grant No. DE-NE0008309. Additionally, collaboration with other PI's on the work, S. McDeavitt (TAMU), C. Deo (GaTech), and R. Mariani (INL) is recognized. The resources and support of University of Arkansas' High Performance Computing group (AHPCC) is appreciated, as well as advice from various members of the MOOSE development team (INL).

References

[1] H. Bailly, C. Prunier, D. Ménessier, The Nuclear Fuel of Pressurized Water Reactors and Fast Neutron Reactors: Design and Behaviour, Lavoisier Pub, Paris, 1999.
[2] N.E. Todreas, M.S. Kazimi, Nuclear Systems, Taylor & Francis, London, 2011.
[3] D.D. Lanning, C.E. Beyer, K.J. Gellhood, Tech. Rep. NUREG/CR-6534 PNNL-11513, FRAPCON-3 Updates, Including Mixed-oxide Fuel Properties, vol. 4, 2005.
[4] Tanju Sofu, A review of inherent safety characteristics of metal alloy sodium-cooled fast reactor fuel against postulated accidents, Nucl. Eng. Technol. 47.3 (2015) 227–239 (Web).
[5] J. Rest, An analytical study of gas-bubble nucleation mechanisms in uranium-alloy nuclear fuel at high temperature, J. Nucl. Mater. 402 (2–3) (2010) 179–185 (Web).
[6] T. Mazzeu, et al., Obtaining of U-2.5Zr-7.5Nb and U-3Zr-9Nb alloys by sintering process, ABEN (2010) (ISBN:78-85-99141-04-5), http://www.iaea.org/inis/collection/NCLCollectionStore/_Public/43/046/43046308.pdf.
[7] A.A. Solomon, S.M. McDeavitt, Preparation of uranium-zirconium alloy nuclear fuel elements by PM, Metal. Powder Rep. 47 (11) (1992) 55.
[8] C.A. Thompson, €œA Rotating Electrode System for the Generation of Metal Alloy Microspheres,€, MSNE Thesis, Department of Nuclear Engineering, Texas A&M University, Dec. 2012.
[9] D.J. Garnetti, €œUranium Powder Production via Hydride Formation and Alpha Phase Sintering of Uranium and Uranium-zirconium Alloys for Advanced Nuclear Fuel Applications,€, MSNE Thesis, Department of Nuclear Engineering, Texas A&M University, Dec. 2009.
[10] S.M. McDeavitt, A.A. Solomon, Hot-isostatic pressing of U-10Zr by a coupled grain boundary diffusion and creep cavitation mechanism, J. Nucl. Mater. 228 (1996) 184.
[11] G. Helmreich, œCharacterization of Alpha-phase Sintering of Uranium and Uranium-zirconium Alloys for Advanced Nuclear Fuel Applications, MSNE Thesis, Department of Nuclear Engineering, Texas A&M University, Dec. 2010.
[12] Sangjoon Ahn, Sandeep Irukuvarghula, Sean M. Mcdeavitt, Microstructure of α-U and δ-UZr2 phase uranium–zirconium alloys irradiated with 140-keV He ion-beam, J. Alloys Compd. 681 (2016) 6–11 (Web).
[13] A.p. Moore, C. Deo, M.i. Baskes, M.a. Okuniewski, Atomistic mechanisms of morphological evolution and segregation in U-Zr alloys, Acta Mater. 115 (2016) 178–188 (Web).
[14] Gui-Yang Huang, B.D. Wirth, First-principles study of bubble nucleation and growth behaviors in İ± U€“Zr, J. Phys. Condens. Matter 24.41 (2012) 415404 (Web).
[15] G. Maier, H. Assmann, W. Dörr, Resinter testing in relation to in-pile densification, J. Nucl. Mater. 153 (1988) 213–220, http://dx.doi.org/10.1016/0022-3115(88)90213-9.
[16] H.Ö. Gülsoy, R.M. German, Sintered foams from precipitation hardened stainless steel powder, Powder Metall. 51.4 (2008) 350–353 (Web).
[17] M. Braginsky, V. Tikare, E. Olevsky, Numerical simulation of solid state sintering, Int. J. Solids Struct. 42 (2) (2005) 621–636, http://dx.doi.org/10.1016/j.ijsolstr.2004.06.022.
[18] Y. Wang, Y. Liu, C. Ciobanu, B.R. Patton, Simulating microstructural evolution and electrical transport in ceramic gas sensors, J. Am. Ceram. Soc. 83 (9) (2004) 2219–2226, http://dx.doi.org/10.1111/j.1151-2916.2000.tb01538.x.
[19] R.L. Coble, Sintering Crystalline Solids. I. Intermediate and Final State Diffusion Models, Sintering Key Papers, 1990, pp. 55–67, http://dx.doi.org/10.1007/978-94-009-0741-6_4.
[20] J. Pan, H. Le, S. Kucherenko, J. Yeomans, A model for the sintering of spherical particles of different sizes by solid state diffusion, Acta Mater. 46 (13) (1998) 4671–4690, http://dx.doi.org/10.1016/s1359-6454(98)00144-x.
[21] Veena Tikare, Michael Braginsky, Eugene A. Olevsky, Numerical simulation of solid-state sintering: I, sintering of three particles, J. Am. Ceram. Soc. 86.1 (2003) 49–53 (Web).
[22] G.J. Fix, in: A. Fasano, M. Primicerio (Eds.), Free Boundary Problems: Theory and Applications, Pitman, Boston, 1983, p. 580.
[23] J.S. Langer, Models of Pattern Formation in First-order Phase Transitions, Series: Series on Directions in Condensed Matter Physics. 1, World Scientific, Singapore, 1986, p. 165. Bibcode:1986SDCMP…1..165L.
[24] J.W. Cahn, J.E. Hilliard, €œFree energy of a nonuniform system. I. Interfacial free energy,€, J. Chem. Phys. 28 (1958) 258.
[25] D. Gaston, C. Newman, G. Hansen, MOOSE: a parallel computational framework for coupled systems of nonlinear equations, in: American Nuclear Society (Ed.), International Conference on Advances in Mathematics, Computational Methods, and Reactor Physics, 2009. Saratoga Springs, NY, May 3€“7 2009.
[26] M.R. Tonks, et al., An object-oriented finite element framework for multiphysics phase field simulations, Comput. Mater. Sci. 51 (2012) 20.

Appendix B

Numerical Simulation of Metallic Uranium Sintering

A thesis submitted in partial fulfillment
of the requirements for the degree of
Master of Science in Mechanical Engineering

by

Bruce Berry
Georgia Institute of Technology
Bachelor of Science in Nuclear Engineering, 2013

May 2017
University of Arkansas

This thesis is approved for recommendation to the Graduate Council.

Dr. Paul Millett
Thesis Director

Dr. Rick Couvillion
Committee member

Dr. Arun Nair
Committee member

ABSTRACT

Conventional ceramic oxide nuclear fuels are limited in their thermal and life-cycle properties. The desire to operate at higher burnups as is required by current utility economics has proven a formidable challenge for oxide fuel designs. Metallic formulations have superior thermal performance but are plagued by volumetric swelling due to fission gas buildup. In this study, we consider a number of specific microstructure configurations that have been experimentally shown to exhibit considerable resistance to porosity loss. Specifically, a void sizing that is bimodally distributed was shown to resist early pore loss and could provide collection sites for fission gas buildup. We employ the phase field model of Cahn and Hilliard, solved via the finite element method using the open source Multi-User Object Oriented Simulation Environment (MOOSE) developed by INL.

ACKNOWLEDGEMENTS

This work would not have been possible without the help of my advisor, Paul Millett. In addition, the frequent discussions with my lab coworkers proved to be invaluable. Support from family and friends is also greatly appreciated.

TABLE OF CONTENTS

LIST OF FIGURES

NOMENCLATURE

k - Thermal conductivity

TD - Percent theoretical density

ϕ - Phase field order parameter

M - Material mobility constant

κ - Interface constant

f_{loc} - Local free energy of mixing

E_d - Lumped forces term

F - Free energy functional

Ω - (Mathematical) hypothetical bounding volume

S - (Mathematical) hypothetical bounding surface

χ - Ratio of small to total pore space

D - Diameter

O - (Complexity) worst case execution cost

Ω - (Complexity) best case execution cost

Φ - (Complexity) tightly bounded execution cost

1 Introduction

1.1 Background

As humanity settles into the Information Age, we strive to apply new technologies to problems that were previously thought to be out of reach. These new challenges continually motivate us to reconsider how best to manage the resources available to us, including energy. We require more of our sources of energy, be it in the form of superior economics or through more sustainable operation. As our demands increase, infrastructure must be modernized to reflect these 21^{st} century needs. Improved nuclear power is expected to play an important role in tomorrow's energy mixture, and significant research and development is currently underway to develop systems that can satisfy future demands. The current research described here focuses on an improved fuel formulation intended for use in next generation reactors. The successful application of this fuel promises next generation reactors with greater safety, profitability, and sustainability, satisfying many of the projected requirements of a next-generation power source. Here we will give a brief overview of the concepts and systems being investigated in the current work and explain the technical motivations of the particular research area.

Nuclear power plants (NPPs) generate power via the splitting of fuel atoms in a self-sustaining chain reaction. The splitting generates significant heat within the fuel which is then removed and carried to steam generators via a coolant, such as water. The water is transformed into steam, and energy is extracted from the steam to produce electricity, in much the same way as coal and gas fired power plants generate power. The splitting of the

fuel atoms results in the production of lighter elements, many of which are radioactive over various time scales. Some of these elements are in the gaseous form, a fact that will be of some importance for this work.

Although very similar in overall operation to fossil fuel plants, NPPs must be additionally secured against the possibility of coolant loss to the fuel, as even when shut down the fuel produces significant residual heat (as a result of radioactive decay) that must be continually removed to avoid fuel melting and plant damage. Such an accident has been observed in operation in previous events - the Fukushima Disaster is a leading example - and significant effort is put into designing systems and operational procedures that minimize the risk of this occurring and mitigate damage should such an event occur. The leading designs for next-generation reactors prioritize passively safe behavior in accident scenarios, which currently employed designs lack in the most extreme situations (such as Fukushima).

Even considering this drawback, NPPs posses several advantages over fossil fuel power plants. They are among the most environmentally friendly power sources available, releasing far lower amounts of radiation than fossil fuel plants, and are rivaled only by hydroelectric power plants in their per capita carbon emissions. They have low sensitivity to fuel prices in comparison to fossil plants, and enjoy very high uptimes, resulting in a very predictable and reliable baseload power source.

Traditional reactors are powered almost exclusively by uranium oxide, UO_2. This formulation is classified as a ceramic material. It has good chemical compatibility with common structural and cooling materials, and like most ceramics possess a relatively high melting point. Not without drawbacks, oxide fuels have a fairly low thermal conductivity, and also exhibit conductivity reduction with increasing temperature for certain relevant temperature

ranges. This behavior imposes operational restrictions that reduce plant efficiency in order to avoid unsafe behavior should unexpected events occur. In addition, plant cycle times between refuellings are somewhat short, owing to the fact that oxide fuels have a rather low heavy metal density, the ratio of uranium (fuel) to other compounds (oxygen) in the fuel material. In somewhat simple terms, this limits the "potency" of the fuel after extended operation, and requires frequent refuellings to maintain a nuclear reaction.

Metallic uranium formulations exist that alleviate many of the problems of the oxide fuel forms. U-Zr alloys exhibit superior thermal conductivity at all temperature ranges, significantly relaxing operational restrictions in place to avoid fuel melting. While their melting point is lower than oxide formulations, their ability to remove heat much more efficiently allows for larger thermal safety margins while maintaining performance. This property lends a certain amount of intrinsic accident-tolerance to the fuel. In traditional reactors, the primary mechanism employed to avoid damage during an accident scenario is by restricting operation to ranges that fail gracefully, that is, by adopting operating procedures that make it difficult for the system to depart from nominal behavior. This technique has been widely successful, and contributes to nuclear power's impressive safety record. It is difficult for this method to secure against events that are highly unlikely, and more destructive than otherwise planned for. Accident tolerant fuels behave acceptably even during events beyond the traditionally designed-for range. Thermal behavior, while only one aspect of accident tolerance in fuels, is an important attribute, and metallic fuels perform admirably in this regard.

In addition to improved thermal performance and safety, metallic fuels posses high initial heavy metal density. This enables operation for longer duration than traditional oxide

fuels, and better total fuel consumption. This value, termed "burnup", is a measure of the utilization of the fissile material in the fuel. The burnup that can be attained is influenced by numerous factors, including the compositional and morphological changes that occur in the fuel as it is consumed. With longer operation between cycles, power plants tend to be more profitable, as refuelling periods are typically considered to be extremely expensive.

1.2 Motivation

The complexities of tomorrow's economy require advanced energy sources that promote growth. It is natural that as society progresses to tackle increasingly difficult problems, our infrastructure must evolve to support these efforts. Fossil fuels have proven invaluable in that they have enabled the cheap fueling of the industrial revolution, which has led to today's technological state. Not without their drawbacks, their continued use will become more expensive, as their extraction becomes more difficult. Additionally, externalities of their consumption will become more evident, both in their local and global effects on the environment.

It is clear that new sources of energy must power tomorrow's society. Next-generation nuclear power is expected to play a part in fulfilling this need. Among the goals in designing the next generation of NPPs, two focus areas emerge: improved safety and enhanced economics. We have already discussed some of the considerations when selecting a fuel for its safety performance. Any system in widespread deployment must be shown to be cost-competitive with alternatives. For nuclear power, upfront capital expenditure is a significant hurdle to adoption. Various solutions to this problem have been proposed, including the design of plants with significantly longer operational lives, enabling the recovery of capital

over longer periods. In addition to capital costs, utility companies are concerned with the frequency at which reactors must be shutdown for refueling and maintenance, as shutdowns are expensive. It is this area in which new fuel formulations become very attractive, as almost all current efforts seek to extend the duration for which fuel can be utilized.

Metallic fuel formulations, while beneficial from a safety standpoint, have behaved poorly during operation in that they experience rapid microstructure changes that inhibit their long term operation (where the microstructure is defined as structural details that are resolvable at the μm size). Specifically, they experience rapid swelling with high temperature operation that prematurely stresses the protective cladding surrounding the fuel pellet. This swelling occurs as a result of pore space elimination within the fuel, followed by fission gas creation as the fuel is consumed. The gases, which are initially contained within the fuel pellet, eventually migrate to the outer region of the fuel, and exert excessive pressure on the cladding. This requires early shutdown and prevents operation to high burnup. It is this particular problem that this research seeks to address, in particular, via microstructure configurations that resist pore loss, and provide space for the capture of fission gases. This modification is an important step in the design of metallic fuels that are suitable for use in NPPs.

1.3 Objectives

The first objective of this study is to develop an understanding of the changes that occur to metallic fuel microstructures as they are thermally annealed, that is, under conditions comparable to those experienced in power reactors. We examine the mechanisms by which the fuel densifies as void space within the structure is eliminated. Certain microstructure

configurations have been shown to behave differently in this regard, and we seek to understand the reasons behind this difference. We find direction for this study from experimental results showing a bimodally-distributed pore size configuration as exhibiting improved resistance to pore loss, and seek to develop computational models that duplicate this result. By developing an understanding into how metallic fuels respond to sintering conditions, it is hoped that future work will be able to design fuels that improve reactor economics and safely.

The operational environment that exists in an active fuel element is complex, and involves rapidly changing temperature, radiation, and stress components. In this work, we develop a model focusing on the behavior in response to thermal effects, but which is capable of extension to include other effects as well. The goal of such a model is to allow follow-on studies to add physical effects incrementally, at each step focusing on the fundamental mechanisms and their affects on the behavior of the fuel system.

1.4 Thesis Organization

This thesis is divided into five chapters. In the introduction, the necessary background knowledge for understanding the scope of this work has been given. The motivations are also presented. Chapter two, the literature review, summarizes the search of existing knowledge that was performed. This formed a starting point in developing a suitable model for the problem, and helped narrow the scope of the work to a particular field of inquiry that had not yet been pursued. In Chapter three, the methods used in developing the model of the problem are described in detail. The results of the work are presented in Chapter four, along with a discussion of them. Conclusions are drawn in Chapter five, in addition to

consideration of limitations and areas of future work.

2 Literature Review

2.1 Introduction

The literature review is primarily directed to three areas; a summary of the history and properties of fuel formulations (both metallic and oxide), the physical mechanisms relevant to fabrication and initial operation (materials science and engineering), and the mathematical models that exist to model these systems via computer simulation (phase field methods, finite element techniques).

2.2 History and Motivation

The first power reactors, and almost all since, have employed oxide formulations of uranium for their fuel source [1]. The ceramic oxides have shown excellent chemical compatibility and good radiological performance in Generation II and III reactors [2]. A fuel intended to replace UO_2 must be shown to be superior to the type currently used, making an understanding of UO_2's properties and performance important. [2] and [3] proved valuable in extracting figures of merit to consider in evaluating a fuel design. In particular, these resources were used to estimate UO_2's thermal conductivity, k, and how this parameter varied over a range of temperatures. It is understood that a significant drawback of these formulations is the low value of k and its tendency to be depressed at high temperatures. This typically results in operating restrictions to avoid unsafe thermally-induced feedback loops. Another figure of importance is in comparing the initial heavy metal density, also provided by these references. We will see that most oxide formulations

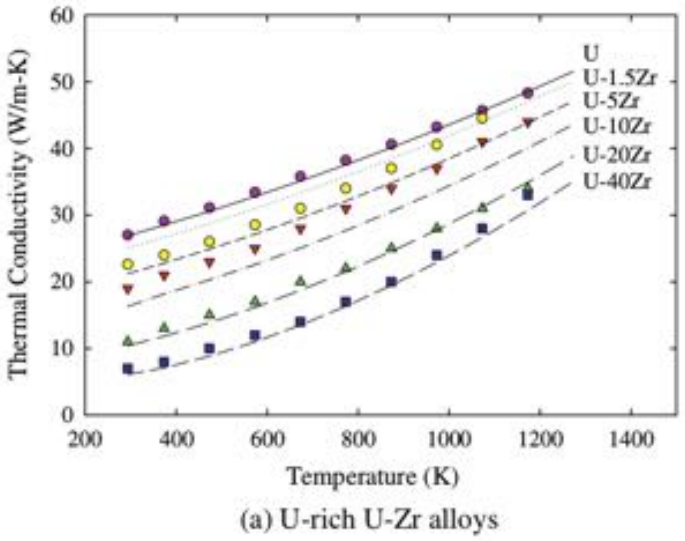

Figure 2.1: Thermal conductivity as a function of temperature for some experimental U-Zr alloys. Improvement with increasing temperature is observed, which is desirable in some accident scenarios. Image source [4]

suffer from a relatively low quantity of usable uranium in comparison to the metallic forms. While this study is motivated primary in developing an understanding of metallic fuels, the discoveries made may also be of use to the oxide fuel community. In the selection of simulation parameters, as will be discussed later, it is thus important to consider values that provide some benefit to both fuel types, making an understanding of UO_2's behavior important. In particular, [2] provides a typical value of $k = 5$ $[W/(m \cdot K)]$ for UO_2 fuels utilized in power reactors.

U-Zr alloys possess properties that make them thermally superior to UO_2 forms, and are chemically compatible with the less common, but much researched, sodium-based coolant systems [5, 6]. With superior conductivity, metal-fueled cores can be made more compact for a given thermal power output, possibly with a corresponding decrease in upfront capital investment. We see also from [4] that an improvement in conductivity occurs with an

increase in temperature. This is beneficial in unplanned overpower or transient conditions, where fuel melting becomes a concern. We also observe the metallic fuels as having superior initial heavy metal density to oxide fuels.

In [6], we find a detailed description of the testing of metallic fuel rods in research reactors, including various failure modes in response to irradiation. Specifically, we find evidence of the early swelling problem often resulting in cladding failure, even at moderate burnup. A solution to this problem is also described: an oversized fuel pin plenum and increased cladding and gap thickness survive fuel swelling until continuous vapor networks formed within the fuel pellet emerge, providing a venting path for the gases into the plenum and limiting further expansion. While this technique of over-strengthening the cladding and then venting all products into the plenum enabled high burnup operation (as high as 20 at.% for some cases), neutronic and thermal hydraulic considerations make this configuration undesirable, although an explanation of such is beyond the scope of this work. For this study, this undesirable swelling is the core issue we seek to remedy, or to at least understand the mechanism by which swelling occurs. Other considerations, such as phase segregation of the zirconium [6], fuel-cladding chemical interaction [5], and other fuel failure modes [6] are not considered herein.

2.3 Experiments

Techniques for the fabrication of metallic fuel forms are described in [7]. We see that traditional casting techniques have been used in the past, but that modern powder metallurgy methods are being developed that enable new capability in terms of microstructure specification for a given application. The formation of depleted uranium powders is

described, with the ability to specify average grain size. Of most interest is the use of an electric arc-discharge through a thin uranium-alloy wire. The wire is melted at the tip, and the molten component ejected into an inert chamber and subsequently solidified into small spheres, forming a fine powder. The distribution of sphere sizes can be controlled. The sintering process of metals is described in [8, 9, 10, 11]. A loose collection of particles is contact-pressure formed into a "green" part that is close to the final geometry of the desired part, but is not monolithic. Under various conditions (a combination of high temperature and pressure), this green part is then "sintered" to induce grain growth and coalescence, until the individual particles within the green part fuse. This process is analogous to the way pottery is produced in clay-based materials. Typically, the sintering temperature is much lower than the melting point of the material. While this is not of vital importance for uranium alloys, it proves essential for elements with high melting points, such as tungsten.

The initial porosity used for beginning our simulations was found to be an important parameter in the study. From the literature [2], this value (TD) is typically in the range 92-96% for UO_2 fuels. There were no articles found that specified this value for the various cast U-Zr alloys (although cast parts typically have minimal porosity), but the hot isostatic pressing process is know to produce metal parts with TD values >90% [12]. Indeed, with the various powder metallurgy techniques, a wide range of starting porosity values are feasible, with iron foams at TD = 20% having been produced [13]. Additionally, work in [14] demonstrated the ability to control both the average grain and pore size, as well as producing a distribution of pore sizes. The desire to produce systems with pores of various sizes adds additional requirements to the fabrication routes. As spheres are closely packed in the pressing step, the arrangement is such that small pores exist between these hard spheres

naturally. “Pore forming” compounds are added to the metal powder before cold pressing into the green form. The pore formers are typically much larger than the bulk material spheres. In a pre-sintering step, these pore formers are eliminated and escape the structure, leaving large voids within the green compact. Later sintering preserves these voids, and by careful pore former selection, it is possible to control the porosity distribution of the sintered piece. This technique provides an avenue for the production of the microstructures investigated in this work.

The work done in [15] proved to be of central importance in providing direction and parameters for the present work. In the article, the author details experiments in which UO_2 samples with different pore structures were sintered and their porosity loss compared. The discovery that the configuration with pores of two primary size ranges produced superior resistance to the otherwise rapid loss of pore space motivated a desire to understand the mechanism via simulation in the present work. As duplication is a valued goal in new domains, it was important to select parameters in this work that produced configurations comparable to those tested in [15]. We adopt similar ratios of large and small void size, as well as relative quantity of each. Additional, similar initial TD values are tested. The reference is similar to the present work in that only thermal effects were considered, not the effects of radiation. Here, we simulate extended annealing as a result of high temperatures exclusively.

2.4 Simulation

As computer systems have grown to enable the solution of larger and more complex problems, methods have been simultaneously developed to model physical systems in ways

that are amicable to solution via simulation. This trend has been maintained in the materials science domain, where computer simulation has been used to predict materials before they have been physically realized in the laboratory [16]. In order to represent the behavior of materials at the level of their microstructure, that is, at sizes that are not observable without magnification, new mathematical models have been developed that attempt to capture the different physical forces and interactions that are dominant.

The Monte-Carlo based Potts model of [17] was applied to the sintering process to address multi-grain growth in solid bodies in [18, 19]. The treatment of vacancies is probabilistic; a vacancy site is randomly relocated and the energy change measured. If the change is favorable, the relocation is kept and the system updated. Unfavorable changes are rejected, but a penalty term is applied that makes a future event more likely. The Potts model with such modification has been shown to provide a good overall description of the sintering process, but its handling of vacancy motion is problematic for this work, in which we expect vacancy motion to play a key role in controlling the densification kinetics. We are therefore motivated to select a model that effects vacancy motion in a more realistic manner.

The phase field family of models is used in this work, and will be described in detail in the methods section (Chapter 3). Their development in the literature is described here. The work of [20, 21, 22] introduced the method as applicable to a range of materials problems, and was applied to a binary alloy system to demonstrate the phase separation of two solids. Further development in [23, 24, 25] showed their application to the sintering process, and later continued annealing. The treatment of conserved and non-conserved entities, such as phase, grain orientation, and others through the use of a continuously varying "order parameter" lends well to discretization on a computational grid, a process which is commonly

performed in many fields. The ability to resolve phase interfaces is particularly advantageous, and various physical effects can be introduced by modification of the free energy functional with new parameters.

Several numerical techniques exist to solve coupled nonlinear systems such as those developed from the phase field methods. The finite difference approach is the most simplistic, but limited in handling complex geometries, and will not be considered further. Spectral techniques in development provide very fast and adaptable solution paths, but at this point in time require in-house development of the software, adding additional difficulties to the validation of simulation results. The finite element method, while relatively slow in the solution when compared to the other techniques, is extremely flexible with regards to problem geometry and physical time and length scales. The MOOSE project [26, 27] adds to this flexibility by providing a large codebase that combines high speed meshing and solution tools with physics packages, including modules for the phase field methods. This codebase allows the present work to sidestep most of the numerical implementation details, and instead focus on model development and interpretation of results. In addition, much of the MOOSE codebase is well validated, with many examples of its successful application to large, complex systems [28, 29]. MOOSE's organization and workings will be further described in the methods section (Chapter 3).

2.5 Densification Studies

Sintering as a process has been well studied, and accurate models exist that predict microstructure and material properties after a given sintering schedule has been performed. The further evolution of these pre-sintered systems in reactor environments is less well un-

derstood, owing to the difficulties created by handling highly radioactive fuel material. Experience with this process is necessary, however, in discerning the morphological changes that result in rapid densification and subsequent swelling of U-Zr alloy fuel formulations. In this regard, we refer to the process as re-sintering or densification studies (also, extended annealing), owing to the fact that the microstructure's starting point is not that of many spheres which are tightly packed, but a continuous structure with pores of various sizes existing within. Of primary interest becomes the phenomena of vacancy transport within the system.

3 Methods

3.1 Introduction

The main focus of this thesis is the execution of simulations that seek to represent the physics of extended annealing of solid bodies after they have been formed via powder metallurgy. We examine the changes that occur to the material's microstructure as thermal effects drive the evolution of the system. To this end, we need two tools to accomplish this goal; a computational model that represents the physics of interest, and a solution technique to transform our problem to one that is solvable on the computer. The phase field family of equations provides us this model, while the finite element method via MOOSE enables the solution via computer. Both of these tools will be described in this section, as well as the additional post-processing procedures utilized.

3.2 Modelling and Solution of Materials Problems

3.2.1 Phase Field Methods

We employ the phase field methods [22], originally introduced by Cahn and Hilliard. These methods are popular in solidification and phase separation problems. A common task of this model is in representing the phases present at a given point in the system (solid, gas, crystal structure, etc). Representation of this phase is done via a so called "order parameter" that is continuous throughout the system. The value of this order parameter (or order parameters) determines what phase is present at a given location. The order parameter takes on a singular value at a given point. Its variation in a two phase system, such as shown

in Figure 3.1, enables easy representation of both bulk and interface regions. Within the bulk of a phase, the order parameter, ϕ, takes on a value of +1 or -1, but interfaces assume intermediate values. The interface width is related to the rate of change of ϕ as it transitions to indicate a phase change.

In Figure 3.2, we show a description of the underlying lattice assumed by the Cahn-Hilliard model, which according to the evolution equation that we will shortly introduce, treats the discrete nature of vacancy transport as a continuous phenomena. Through this image, we can imagine a pore as a very large collection of uninterrupted vacancies in the lattice, contained within the larger fuel system. Individual vacancies can be released from this large collection and freely propagate throughout the lattice. Rather that discretely tracking the location of these vacancies at each lattice point, we use a single parameter whose value varies in accordance with the species (vacancy or atom) present at each point.

$$\frac{\partial \phi}{\partial t} = \nabla \cdot M \nabla \frac{\delta F}{\delta \phi} \tag{3.1}$$

$$F(\phi) = \int_V [f_{loc}(\phi) + \kappa |\nabla \phi|^2 + E_d] dV \tag{3.2}$$

Equation 3.1 is the Cahn-Hilliard equation, cast in the form suitable for the solution of binary systems. ϕ is the order parameter representing the phase at a given location. In our case, we take $\phi = 1$ as representing fuel material and $\phi = -1$ as denoting the existence of a void space. F is the free energy functional, determining the driving forces in the system's evolution. M is a proportionality value known as the mobility with units $[L^2][T^{-1}]$. To constrain ϕ to the range [-1,1], we cast F to include a double well potential, taking the

form given in Equation 3.2. This ensures that the two phases (fuel and void) will evolve to separate when given the proper driving force, which in this case is the thermal energy provided by the annealing process. Here, f_{loc} is the local energy of mixing (the double well), the κ term the interface energy, and E_d a lumped parameter including any additional energy sources (electric, stress, etc). We require that the annealing process be isothermal, enabling a uniform value for the mobility. Furthermore, we do not consider thermal profiles that would enable a non-homogeneous mixture of the two constituents (uranium and zirconium), nor do we allow precipitation of alternative phases. With this, we can declare the mobility as constant.

In its fully general form, F is given by Equation 3.2. Of interest to us are the energies of mixing and the interfacial energy. Thus, we only consider the f_{loc} term along with the interface term to arrive at the specialized form used here, Equation 3.3. We also specialize the local free energy term to encourage phase separation, as provided by the double well.

$$F(\phi) = \int_V (\phi^4/4 - \phi^2/2 + \kappa|\nabla\phi|^2)dV, \tag{3.3}$$

Often, we model mixing and subsequent phase separation of two immiscible phases. The problem of vacancy transport in a one phase system can be imagined as such. Figure 3.4 shows the evolution of a two phase system that is immiscible, such as oil and water. The two phases are initially intimately mixed, indicated by the uniform light blue color in the first image. As the system evolves in time, small pure regions of each phase are formed (or nucleate), and then grow as nearby material is transported into these nucleated regions. These separate regions can interact with other pure regions to form larger pure bubbles, or

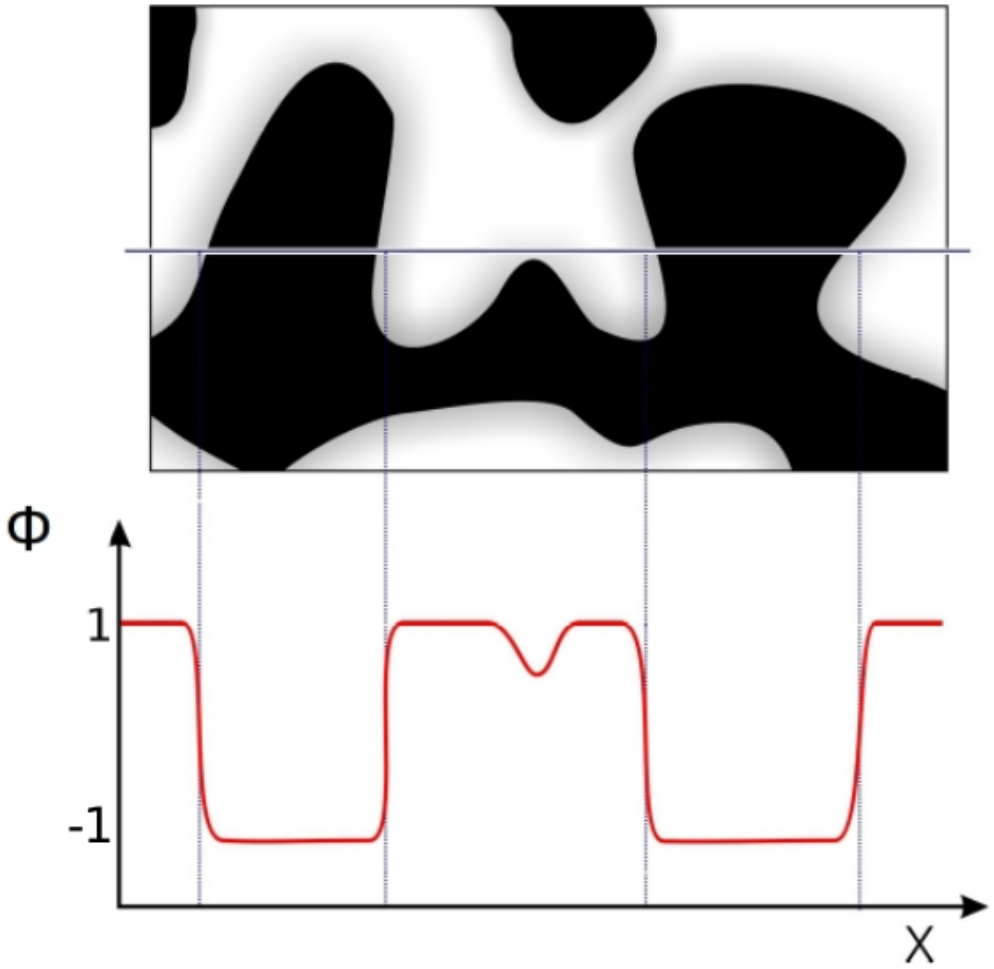

Figure 3.1: Example system containing two phases undergoing separation. The order parameter (ϕ) takes a value of 1 in the white region and -1 in the black region. The value changes rapidly, but smoothly, at the interfaces. Image source [30].

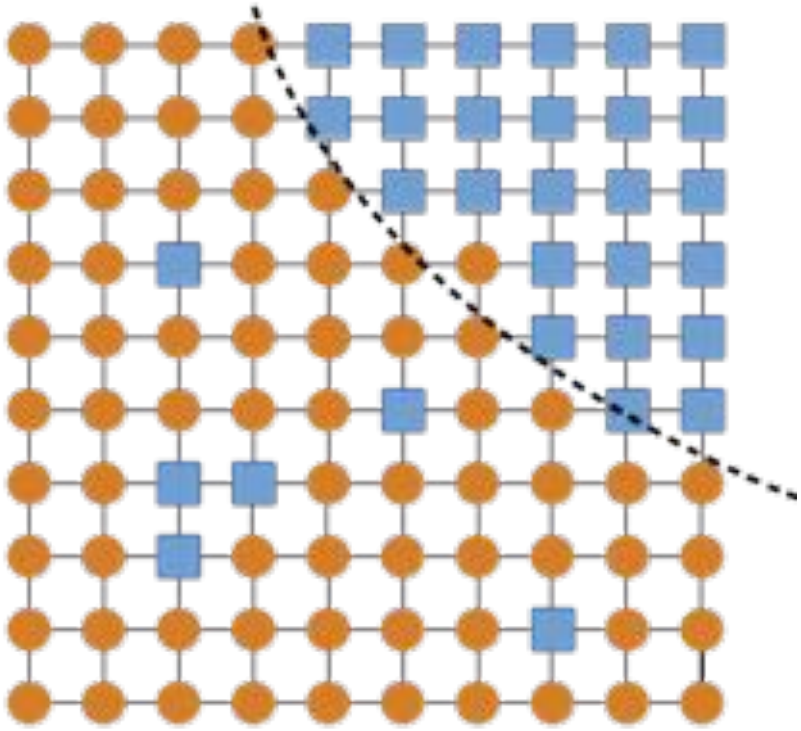

Figure 3.2: An illustration of the assumed atomic lattice, with orange circles denoting sites occupied by atoms, and blue squares representing a vacancy in the lattice. The dashed line represents the boundary of a pore contained within the system. Vacancies can travel through the lattice, exchanging places with nearby occupied sites. Through this mechanism, vacancies are able to exit the system during the densification process. We note here that the pore size is not to scale, but merely representative.

merely grow by diffusion of like components from nearby mixed regions to the surface of the nucleated bubble. This process will continue until only two regions of pure material exist, as such a configuration has the lowest interface area. As a large surface area is energetically unfavorable (the interface, not being pure, is energetically difficult to maintain), the configuration with minimum surface area is preferred.

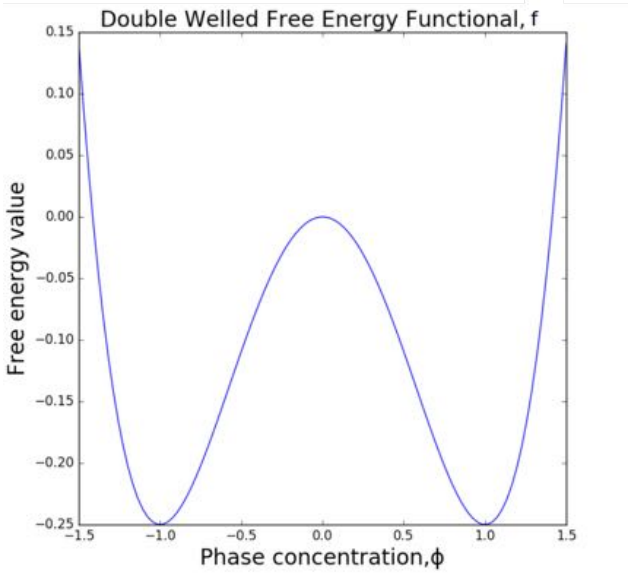

Figure 3.3: Double-welled free energy functional, f_{loc}. Minima at $\phi = \pm 1$ mean that full phase separation is most energetically favorable, and the system will attempt to evolve into such a configuration.

3.2.2 Polynomials by Example

Equations such as Equation 3.1 are difficult to solve on computers in general. It is usually necessary to cast such equations into an algebraic form that can be solved via basic operations, a task at which digital computers perform admirably. To this effect, we decompose the system we are trying to simulate (the fuel pin) into many smaller elements that are interconnected. By using sufficiently small elements, we can solve each individual location using simple algebraic relations, providing a good approximation of the true solution. This concept forms the basis of the finite element method, as we will now describe.

The concept of polynomial curve fitting provides a good starting point in describing the finite element method. In producing a polynomial that approximates a function, we take a set of points from the function, and seek a polynomial that passes through each point. There are many polynomial forms, with perhaps the simplest of the form:

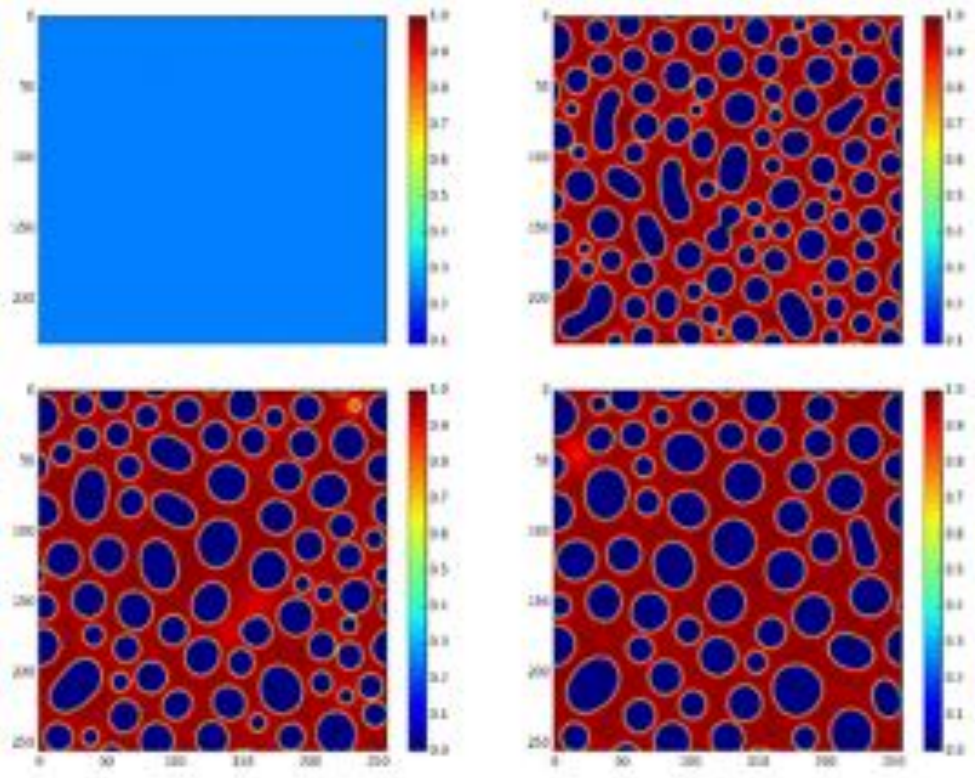

Figure 3.4: Evolution in time of a binary phase system. Initially well mixed, small bubbles of the blue phase nucleate and grow. After sufficient time, the two phases will entirely separate, leaving only a single interface. This configuration is energetically favored when using f_{loc} in a double welled form, as given in Equation 3.3.

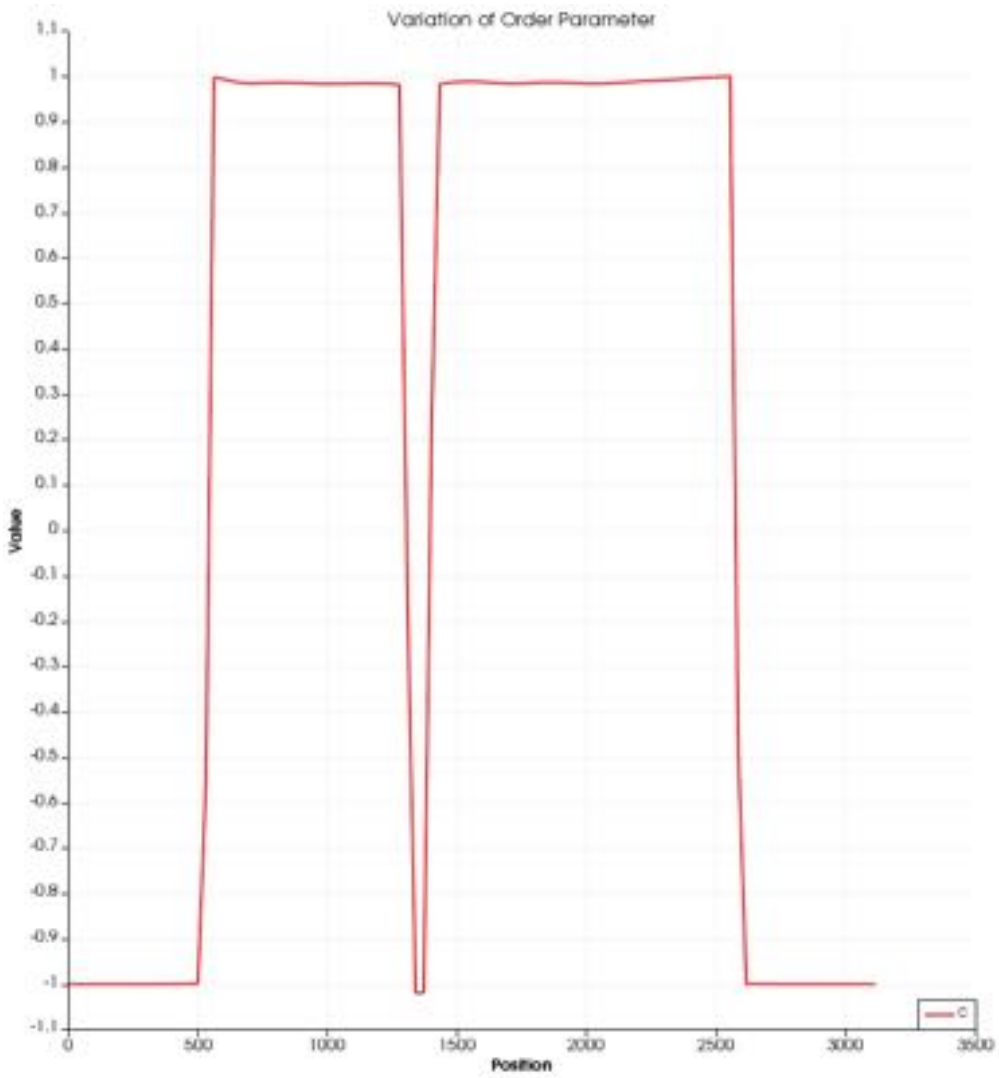

Figure 3.5: Variation of ϕ over a fuel/void system generated in this study. ϕ assumes a value of +1 within the fuel material, but rapidly changes to -1 over a few elements at the fuel/void interfaces. In this image, the region sampled starts at the boundary of the fuel, passes through a single void, and leaves the fuel region.

$$f(x) = \sum_{i=0}^{d} c_i \phi_i(x) \tag{3.4}$$

where the c_i form the coefficients and the ϕ_i are the basis functions. It is common for the basis functions to be of the form:

$$\phi_i(x) = x^i \tag{3.5}$$

We solve Equation 3.4 to obtain the values of the c_i's. If we are given n points, then selecting $d = n - 1$ (where d is the highest degree of the polynomial) will guarantee that $f(x)$ is unique and interpolary. It is best to illustrate the concept with a simple example. Consider the collection of points:

$$x_1, y_1 = (1, 2)$$

$$x_2, y_2 = (2, 1)$$

$$x_3, y_3 = (3, 2)$$

From Equation 3.4, our system of equations will be

$$y_i = c_1 + c_2 x_i + c_3 x_i^2, i = 1, 2, 3 \tag{3.6}$$

Keeping in mind our goal of solving for the coefficients c_i, we obtain the linear system:

$$\begin{bmatrix} 1 & 1 & 1 \\ 1 & 2 & 3 \\ 1 & 4 & 9 \end{bmatrix} \begin{bmatrix} c_1 \\ c_2 \\ c_3 \end{bmatrix} = \begin{bmatrix} 2 \\ 1 \\ 2 \end{bmatrix} \tag{3.7}$$

The solution to which is:

$$\begin{bmatrix} 5 \\ -4 \\ 1 \end{bmatrix} \tag{3.8}$$

This results in the solution function,

$$f(x) = 5 - 4x + x^2 \tag{3.9}$$

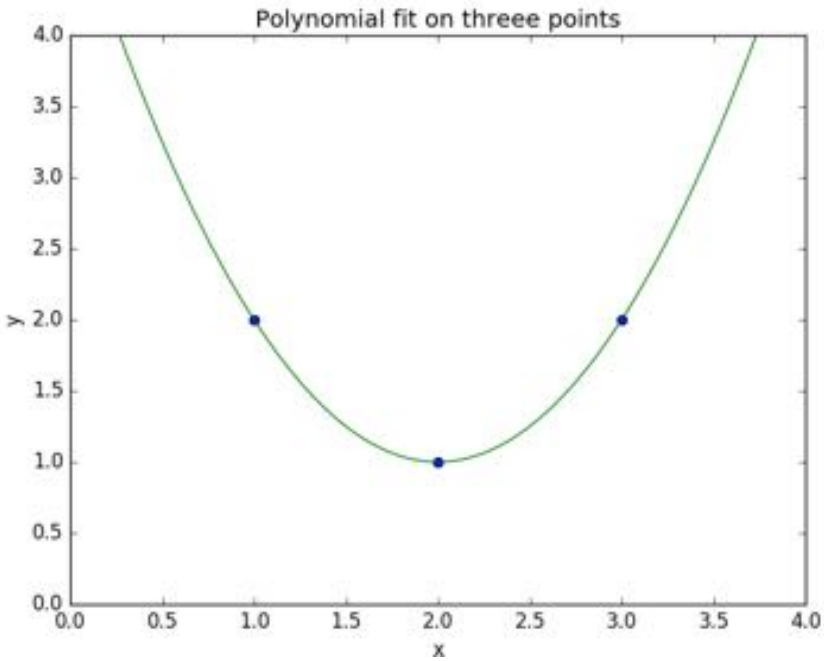

Figure 3.6: Polynomial fit of 3.4 to the points. Interpolation of the points is guaranteed, but accuracy outside of the point range is not.

Polynomial fitting as in the given example is expanded to be applied over the solution domain, with each polynomial being a globally valid component of the solution, but only providing a nonzero result at the element for which it represents. The domain is subdivided into many discrete parts, which are themselves represented by the original physical equation.

In order to allow the solution of these approximated elements, we must cast the original equation in its weak form.

3.2.3 Weak Formulations

With polynomial fitting, we can approximate continuous solutions with piecewise systems of equations. This enables us to solve difficult partial differential equations via solution of an algebraic system of equations. As an example, consider the 1-D steady-state conduction equation with a known source term,

$$-\nabla \cdot k\nabla u = f \tag{3.10}$$

We begin by recasting this equation in its weak form, that is, by reducing the degree of derivatives present and multiplying by a test function, to allow numerical flexibility. Start by rearranging all terms to one side:

$$-\nabla \cdot k\nabla u - f = 0 \tag{3.11}$$

Then, multiply each term by a test function, ψ:

$$-\psi(\nabla \cdot k\nabla u) - \psi f = 0 \tag{3.12}$$

Now integrate 3.12 over the problem domain, Ω:

$$-\int_{\Omega} \psi(\nabla \cdot k\nabla u) - \int_{\Omega} \psi f = 0 \tag{3.13}$$

It is useful here to recall Gauss's Divergence Theorem from vector calculus,

$$\int_{\Omega} \nabla \cdot \vec{g} dx = \int_{\partial\Omega} \vec{g} \cdot \hat{n} ds \tag{3.14}$$

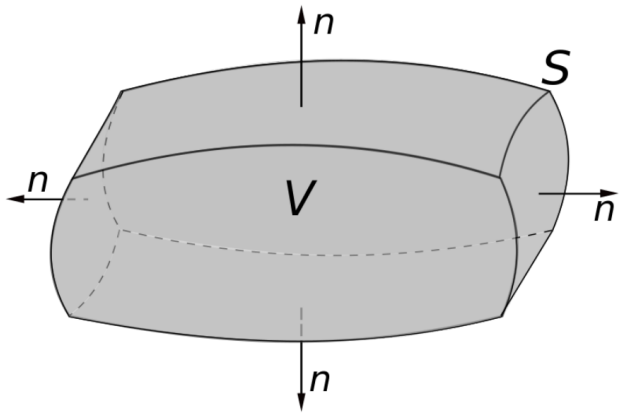

Figure 3.7: Divergence Theorem volume and surface. The time rate of change taken over the entire volume is equivalent to the total net flux across the surface, for a conserved vector field quantity. Image source [31]

Finally, we apply Equation 3.14 and the chain rule to the first term in Equation 3.13:

$$\int_{\Omega} \nabla\psi \cdot k\nabla - \int_{\partial\Omega} \psi(k\nabla u \cdot \hat{n}) - \int_{\Omega} \psi f = 0 \tag{3.15}$$

This constitutes the weak form of Equation 3.10. It is common to rewrite this equation using inner product notation, as will become useful when applied to MOOSE,

$$(\nabla\psi, k\nabla u) - < \psi, k\nabla u \cdot \hat{n} > -(\psi, f) = 0 \tag{3.16}$$

The next step to be performed in making the model suitable for solution via computer is by discretizing the domain, representing the points with interpolating polynomials. That is, we expand our solution variable,

$$u \approx u_h = \sum_{j=1}^{N} u_j \phi_j \tag{3.17}$$

where h is a nodal point on the finite element grid, and N is the number of nodes used. This is analogous to the expansion used in Equation 3.4, and by selecting the same functional form for ψ and ϕ, we arrive at the Galerkin finite element method. The weak form permits easier solution of the constituent equations, but is not strictly accurate. Thus, our problem changes from one of an exact solution to one of error minimization. We thus rewrite Equation 3.16 to reflect this fact:

$$R_i(u_h) = (\nabla\psi_i, k\nabla u_h) - < \psi_i, k\nabla_h u \cdot \hat{n} > -(\psi_i, f) \text{ for i = 1,...,N} \tag{3.18}$$

where $R_i(u_h)$ is the residual error vector.

By Equation 3.17, we have discretized all components except for the integrals appearing in Equation 3.15. In order to solve these on the grid, we relate the integral of a function to the sum of its element integrals,

$$\int_{\Omega} f(\vec{x}) d\vec{x} = \sum_{e} \int_{\Omega_e} f(\vec{x}) d\vec{x} \tag{3.19}$$

where Ω_e is a physical element in the domain.

The technique given here for the conduction equation can be extended to a large class of problems commonly encountered in science and engineering, including the Cahn-Hilliard equation (with some modification). Still remaining is a description of how it is implemented in MOOSE under the phase field physics module. In addition, we must specify the type of basis function we select to represent the solution. Also, the numerical algorithm chosen to

solve the system of equations is of some importance, as the equation system is large. These details will be explained after MOOSE is introduced, next.

3.3 MOOSE

3.3.1 MOOSE Basics

As taken from the mooseframework.org homepage,

> The Multiphysics Object-Oriented Simulation Environment (MOOSE) is a finite-element, multiphysics framework primarily developed by Idaho National Laboratory. It provides a high-level interface to some of the most sophisticated nonlinear solver technology on the planet... [32]

The purpose of MOOSE is to improve scientists' and researchers' access to advanced solution tools that utilize the finite element method. In the past, users typically had two options. While finite element meshing and linear algebra solution libraries were available, their use was complicated, being encumbered by the complexity of application development and the difficulties of parallel programming (if large problems were of interest). As an alternative, users could purchase licenses for expensive professional software, but these packages were often not sufficiently domain-specific to support the wide range of cutting edge research being performed.

MOOSE attempts to provide an alternative that is simultaneously open, capable, and easy for the user to modify. MOOSE implements the finite element method in a way that enables modular addition of physical phenomena at varying length and time scales. It provides a framework upon which users can specify the geometry and initial conditions of problems, invoke the appropriate physics packages already included, and specify solution techniques that lend well to their available hardware and particular problem type. The

addition of new physics kernels is also relatively straightforward, and typically does not require modification of any other part of MOOSE. MOOSE harnesses many modern software practices to improve collaboration with other researchers, and has an active community of users.

In this work, two main points of interaction with the MOOSE system were required to develop the capability of modeling annealed microstructures. The first involved the specification of the values of the field parameter, ϕ, to represent fuel and voids, respectively. We implement this with an initial condition class, denoted PorosityIC, to place voids at the desired locations for each microstructure configuration of interest. We will also need to invoke the appropriate phase field equations to solve ϕ over our domain. In MOOSE, physics "kernels" enable turn-key activation of various physical partial differential equations, including the Cahn-Hilliard equation.

3.3.2 Phase Field Implementations

The MOOSE phase field kernels (as we describe shortly) expect instruction on how to initialize the order parameter at each nodal point. The so called "CompactDataReader" class was written for this purpose. It takes a list of pore regions in the format

```
x-position , y-position , radius
```

and builds a list in MOOSE memory, which is then handed to PorosityIC. In the data file, we reserve the first entry to denote the location of the entire system, and assign a value of 1 to ϕ in this region to denote fuel. All other entries represent pores (or the exterior of the fuel) and receive an initial value of -1. Details of the algorithm used to select the pore

sites are discussed in Section 3.4.2.

In SmoothCircleBaseIC, the base class for initial conditions containing circles or spheres in MOOSE, the method "value()" is used by the mesh to assign ϕ's starting value at every nodal point. PorosityIC overrides value()'s operation with the following pseudo-code:

```
def value(gridPoint p):
    val = outval                        # given as -1, void
    dist = distance(p,circles[0])
    if (dist < circles[0].radii)        # within fuel, check for void
        val = inval                     # given as +1 by input file
        for (circle in circles[1:]):    # loop over all but first
            dist = distance(p,circle)
            if (dist < circle.radii):
                return outval           # in a void
    return val
```

This method is eventually called by MOOSE for every nodal point, p, in setting the initial value of ϕ. We store the boundary of the fuel in the first entry of "circles", with all subsequent entries being used to denote void locations. The cost of the void check is $O(N)$ (for each point p) in the worst case. For this work, the cost of the finite element calculations (eg. after initialization) was found to completely dominate this step.

The most general form of the Cahn-Hilliard equation used by MOOSE is given in Equation 3.20. We will specialize it to ignore additional external driving forces (E_d), and to consider only a single concentration variable ϕ.

$$\frac{\partial \phi_i}{\partial t} = \nabla \cdot M_i \nabla \left(\frac{\partial f_{loc}}{\partial \phi_i} + \frac{\partial E_d}{\partial \phi_i} - \nabla \cdot (\kappa_i \nabla \phi_i) \right) \tag{3.20}$$

In solution of Equation 3.20, ϕ is fourth-order in terms of its derivative. Thus, the usual technique of preparing PDE's for use with MOOSE is often modified. Introducing the chemical potential μ as the energy absorbed or released during a phase transition, we split the Cahn-Hillard equation into two parts, with the first seeking to solve ϕ w.r.t μ, and the second solving μ w.r.t ϕ. By flipping back and forth, we can update ϕ in time without explicitly needing the higher order derivatives. In MOOSE, this results in the following residual equations (where we have made the additional simplifications mentioned above),

$$\begin{aligned} R_\mu &= \left(\frac{\partial \phi}{\partial t}, \psi_m \right) + (M \nabla \mu, \nabla \psi_m) - \langle M \nabla \mu \cdot \vec{n}, \psi_m \rangle \\ R_\phi &= (\nabla \phi, \nabla (\kappa \psi_m)) - \langle \nabla \phi \cdot \vec{n}, \kappa \psi_m \rangle + \left(\left(\frac{\partial f_{loc}}{\partial \phi} - \mu \right), \psi_m \right) \end{aligned}$$

where f_{loc} is the double well potential. The parameters M and κ represent the vacancy mobility and interface coefficient, respectively, and are specified by the user in the MOOSE input file as material properties. All systems simulated were given a value of $M = \kappa = 16.0$.

With this splitting, the residual equation is formed by employing the process as described earlier to generate a weak form. Each term of the residual equation corresponds to a separate class, or "kernel", in MOOSE. The components are combined to generate the system of equations to be solved. In Table 3.1, the names of the kernels used are given, where we have simplified F to model our binary system. Also important is the boundary condition utilized in the solution of 3.21. The fuel bodies produced are surrounded by a slightly larger bounding box (which represents the environmaent) in which no fuel material

Name	Residual Term	Variable	Required Params
CoupledTimeDerivative	$(\frac{\partial \phi}{\partial t}, \psi_m)$	μ	-
SplitCHWRes	$(M\nabla\mu, \nabla\psi_m)$	μ	M
SplitCHParsed	$(-\kappa\nabla^2\phi) + \frac{\partial f_{loc}}{\partial \phi})$	ϕ	κ

Table 3.1: MOOSE Kernels invoked during solution of the binary system.

is present. No-flux boundary conditions are applied at the edges of this box.

3.3.3 Finite Element Implementations

Solution of the residual equation (Equation 3.18) requires the specification of two additional details. First, the interpolation functions must be specified. MOOSE supports a wide variety of shape functions. In many cases, the default "QUAD9" 2-D element is accurate and efficient. Its behavior is shown in Figure 3.8.

The second detail of necessity is the method by which the system of equations generated will be solved. While a deep understanding of the numerical techniques is not required to understand the results of this work, a short summary of the technique employed in MOOSE will be included here for completeness.

Newton's method is an iterative technique to finding an approximate root of a real valued function. In a single variable, it uses the derivative of the function and an evaluation at the current root guess to generate a better approximation, according to

$$x_{n+1} = x_n - \frac{f(x_n)}{f'(x_n)} \tag{3.21}$$

Newton's method has very good convergence properties for many problems, and is simple to implement. When the function's value and derivative are easily obtainable, it is an excellent choice for root finding. It can also be extended to a system of nonlinear equations and used to solve the residual equation given earlier, where the function roots minimize the residual error (in this case, the 2-norm of the error vector formed from each u_h component in the solution). In comparison to the other solution tools available in MOOSE, Newton's method has the best consistent performance on our particular problem, although the memory requirements were somewhat increased due to the need to store the Jacobian matrix. It was selected over the other primary nonlinear solver available in MOOSE (the Jacobian-Free Newton-Krylov method).

The extension of Newton's method to a nonlinear system is again best demonstrated by example. Consider the following nonlinear system in two dimensions,

$$f_1(x_1, x_2) = e^{x_1+x_2}$$

$$f_2(x_1, x_2) = sin(x_1)$$

We use a Taylor expansion around a point x_0,

$$\vec{F}(\vec{x}) = \vec{F}(\vec{x_0}) + \vec{J}(\vec{x}) * (\vec{x} - \vec{x_0}) + \Theta(x^2) \tag{3.22}$$

where $\vec{J}$ is the Jacobian,

$$\vec{J}(\vec{x}) \equiv DF(\vec{x}) = \begin{bmatrix} \frac{\partial f_1}{\partial x_1} & \frac{\partial f_1}{\partial x_2} \\ \frac{\partial f_2}{\partial x_1} & \frac{\partial f_2}{\partial x_2} \end{bmatrix} \tag{3.23}$$

Dropping the truncation term (which makes the technique second-order accurate), we rearrange Equation 3.22 to solve for $\vec{x}$, the updated root approximation,

$$\vec{x} = \vec{x}_0 - (\vec{J}(\vec{x}_0))^{-1}\vec{F}(\vec{x}_0) \tag{3.24}$$

We can avoid taking the inverse of $\vec{J}$ by observing that there exists an s such that

$$\vec{J}(x_k)s = -\vec{F}(x_k) \tag{3.25}$$

Then, we use Gaussian elimination to obtain an updated x,

$$x_{k+1} = x_k + s \tag{3.26}$$

There are a wide range of techniques in solving the system from Equations 3.25 and 3.26 , which is large, sparse, non-symmetric, and linear. The Generalized Method of Minimum Residuals (GMRES), itself an iterative method, is fast and flexible, but requires preconditioning to be effective, as it belongs to the family of Krylov subspace methods. This is not a major issue, as we already posses the Jacobian for the nonlinear Newton solve, and can use this as a preconditioner. GMRES is the default choice in MOOSE, although others are supported. In summary, the overall solution process is as follows,

1. Produce the weak form of the nonlinear PDE to be solved.

2. Discretize the system and solution into nodal elements.

3. Rearrange the discretized system to a residual problem, in which we solve a system of nonlinear equations such that an error metric is minimized.

4. Use multivariate Newton's method as a root finder to find an approximate solution to the residual equations.

5. At each nonlinear Newton iteration, solve a linear system of equations, taking advantage of the Jacobian matrix as a preconditioner, via GMRES.

6. One time step has been solved, repeat for each time step.

3.4 Analysis

3.4.1 Parameters and Figures of Merit

Two key parameters were used to define the microstructure configuration. The first was the total initial porosity in relation to fuel material, expressed as a percentage,

$$TD = (1 - \frac{A_{pores}}{A_{system}}) * 100 \tag{3.27}$$

where

$$A_{pores} = A_{small} + A_{large} \tag{3.28}$$

This parameter is often referred to as the Initial Theoretical Density in the nuclear industry, and for oxide fuel pellets, a typical value is 92%. We expect configurations with a lower TD to require longer annealing times in order to remove all void space. We are not

Parameter	Range
$TD(\%)$	92,94,96
$\chi(\%)$	0,20,40,60,80,100

Table 3.2: Initial porosity characteristics.

sure, however, how bimodal systems will respond to varying TD values, so we simulate a range of configurations.

The second parameter that specifies microstructure configuration determines the ratio of small pores to all other pores in the compact, defined as

$$\chi = \frac{A_{small}}{A_{small} + A_{large}} * 100 \tag{3.29}$$

With this parameter, we control the degree to which the microstructure is bimodal. Configurations with $\chi = 100$ contain only small pores. These configurations are what are deemed to be comparable to fuel structures fabricated via traditional sintering methods, without any attempt at porosity control. As we decrease χ, we add more and more large pore regions, presumably via addition of pore formers that are subsequently eliminated during sintering. At $\chi = 0$, the only pores present are those with the larger diameter. This configuration is not necessarily realizable in practice, but is useful for comparison purposes (as will be seen in the results section). The combinations of TD and χ form our configuration space, and is enumerated in Table 3.2.

3.4.2 Initial Porosity Generation

At this point, it is important to mention that the MOOSE simulations are executed in two dimensions rather than three. Thus, spherical pores are reduced to circular pore regions. This approach is common in problems where the mechanisms are independent of the direction of propagation. In our case, a uniform and constant Mobility allow this simplification to hold. We will not consider 3-D geometries further, in the interest of avoiding undue computational expense.

We seek to model circular fuel pin geometries with two phases (fuel and void space). To generate systems with differing void placement, we adopt a stochastic approach in selecting the location of the voids. We randomly select a location to place a void within a defined bounding area. Keeping track of the quantity of small and large voids already placed, we select a size that keeps us close to our objective mixture, while also ensuring that the new void does not overlap with an existing void or go beyond the surface of the system. Once these criteria are met, we restart the procedure, adding pores until our desired initial porosity is reached. A simplified description of this algorithm is given in pseudo code below.

```
voids = []
small = large = 0
while ((small + large) < targetArea):
    chiCurrent = small / (small + large)
    if (chiCurrent < chiTarget):
        addVoid(small_r)
        small += pi*small_r**2
```

```
        else
            addVoid(large_r)
            large += pi*large_r**2


    addVoid(radius)
        x_pos = rand()
        y_pos = rand()
        if (!overlap(voids,x_pos,y_pos,radius)):
            voids.add(x_pos,y_pos,radius)
        else:
            addVoid(radius)
```

Occasionally, the system will be just short of the target porosity, but require a large void to meet the χ requirement. This results in a large pore being placed and causing the system to have a slightly lower porosity than expected (this can occur for small pores as well, but the effect is not as pronounced). We quantify this behavior by tracking the percent error between the expected and actual porosity. The error found here was never more than 3%, and was typically much smaller. A similar analysis is performed to ensure that the actual χ value is close to what is expected. We also note that in the implementation of the void placement algorithm, a limit is set on the number of times to try placing a void of either size, as in the extreme, highly porous systems may not have any space for another void. This resulted in the occasional failure to generate a configuration, which was always recoverable by simply running the algorithm again, with a different random number seed.

We note that the algorithm is $\Omega(N^2)$ in the best case, and can be worse, depending on the density of voids. While these simulations keep N at a tractable level (given the impressive speed of modern computers), larger simulations would require an improved algorithm for void placement. Such algorithms were briefly investigated and found to be promising, with expected complexities of $\Theta(NlogN)$.

3.4.3 Post-Processing

As the fuel compacts are evolved, we expect void space to move from the interior of the fuel structure to the surface. This has the effect of reducing the radius of the fuel cross section, a behavior we can directly measure as a means of comparing the shrinkage rates between different configurations. To this affect, we developed an analysis tool that tracks this change, using Paraview's [34] built-in LineSampler to record the extent of the fuel compact at each simulation time step. The general algorithm employed is as follows;

1. Sample a diameter of the fuel compact.
2. Record the outermost points at which ϕ transitions (based on the point at which ϕ goes below 0).
3. Measure the distance between the points as the fuel diameter.
4. Repeat a few times for each sample to average out small fluctuations, and produce an area.

The system sizes for each configuration are measured at each time step and then plotted for comparison. We also keep track of the error at two levels of granularity. By

averaging over a few line samples per test, we reduce our measurement error, which is important when fuel surface deformations occur. At a higher level, multiple runs for each configuration are averaged to account for "configuration" error, which arises due to the random placement of voids and the systems' relatively small size. Our error metric utilized here is the standard deviation.

In addition to a line sample, which produces shrinkage rates, we will also be interested in the average concentration of vacancies within the fuel region. By recording the value of ϕ at every point within the fuel, and ignoring void regions, we can average these measurements to arrive at the average vacancy concentration in the entire system. This average is not useful for understanding which particular regions of the system are vacancy rich, as we expect significant increases near pores and depression in pore-sparse areas. It is insightful, however, in measuring the overall vacancy transport gradient that is generated by the dissolution of the small pores into the fuel matrix. This will prove useful in comparing the behavior of the monomodal and bimodal configurations. A postprocessor was developed that measures this metric at each time step, again averaging over each run.

A brief description of the Paraview [34] software is warranted. This open source visualization package enables researchers to access powerful visualization and analysis tools. Its open and modular nature encourages extension; this fact proved valuable when developing the particular analysis techniques used for this work, as all the actual data extraction was abstracted by Paraview. We were solely responsible, therefore, for interpretation of the data returned. Paraview is developed by Kitware and Sandia National Laboratory.

3.4.4 Metaparameters

In development of the analysis tooling, a few parameters emerged as being important to the analysis itself, but not the results in particular. Some of those parameters are described here.

The system size is limited in practice by the number of nodes that could be reasonably simulated on the available computer hardware, and is selected to be as large as possible while still giving good grid resolution. Keeping the node count constant, a larger system would be resolved in less detail in comparison to a small system, but smaller systems were expected to be more sensitive to surface effects. A practical node count limit was found to be 4096 X 4096. A system size of 1100 x 1100 units is used, resulting in around 4 nodes per simulation length unit ($\Delta x = 0.268$).

Small pore regions were given a size of 5 units, and large pores 50. While the ratio of the two pore sizes is similar to that used in [15], the absolute size of the pores in comparison to the system diameter is impossible to replicate with the small finite system used. In this study, the ratio of large pore size to system size was 10^{-1}, whereas for physical fuel elements it is much smaller. This contributed to surface effects (as we will expound upon in the results section), but is not expected to detract from the validity of the results. Additionally, a parameterization of the system size is carried out to assess the impact this relatively low ratio has on the system evolution.

Each configuration enumerated in Table 3.2 was repeated 5 times for statistical reliability, with the intent of measuring surface effects. This count, referred to as N, was deemed to be sufficient, given the resource constraints.

3.4.5 Automation and Reusability

The entire process of fuel compact generation, MOOSE simulation, and the various data analysis steps is scripted to require minimal user management. Indeed, entirely new datasets, complete with analysis and graphical results, can be generated by adjustment of the desired parameters and only a few commands. The automated tasks include (in order of execution):

1. Generate system compacts for the combination space of TD and χ desired, with each configuration repeated N times for statistical soundness. This was automated via a bash shell script loop used to call the CompactGeneration routine. In this step, occasional compact generation failures required manual re-running of the offending member. In a typical batch of 90 samples, a few failures are expected.

2. Submit the samples to the HPC queue for simulation in MOOSE. A base MOOSE input file is read by the submission script and modified to point to the relevant compact file. All jobs are then submitted to the HPC job queue and executed by MOOSE.

3. After all the jobs have completed, the log files are checked for errors, rerun if necessary, and the results copied back to local storage for analysis. This step is manual.

4. Each configuration is line sampled twice at each time step. The results of the line samples are averaged and saved for analysis in the next step.

5. The averaged system diameters are converted to areas and the standard error for each configuration group computed. These values are then plotted, with user options

available to specify which configurations should be shown. This option is provided to make it easy to generate figures for analysis or publication.

6. A Paraview script is used to enumerate all points in each system, and compute the average concentration of vacancies in the non-pore regions at each time step. Again averaging for each configuration group, the results are plotted to figures.

7. Optional routines generate and display various error metrics used during analysis of the data. These error metrics are displayed over the time steps simulated.

A flowchart visualizing the process is given in Figure 3.10

3.4.6 Execution Costs

For a full configuration space run with N=5 samples per configuration, the 90 MOOSE simulations require around 1 week of real time on the Millett Research Group queue (32 Intel Xeon-equipped nodes). Each job is typically run on 4 nodes. The compact generation step is completed for all configurations in minutes, and the post-processing step in a few hours. Once postprocessing has been completed, plots can be reconfigured in a few seconds. Each sample requires around 2GB of storage space, or around 180GB for the entire experiment.

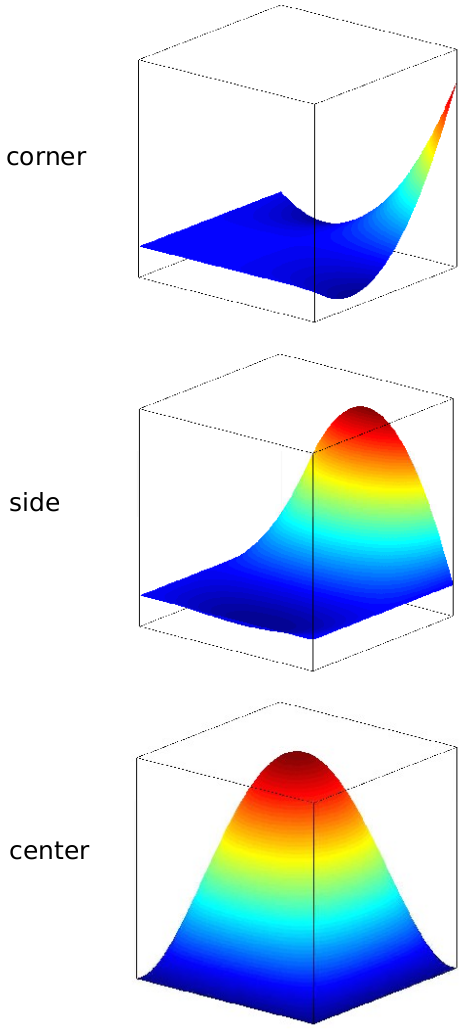

Figure 3.8: Bi-quadratic Lagrange Shape functions in 2-D, showing 3 of the 9 nodal types used for a finite element. Image source [33]

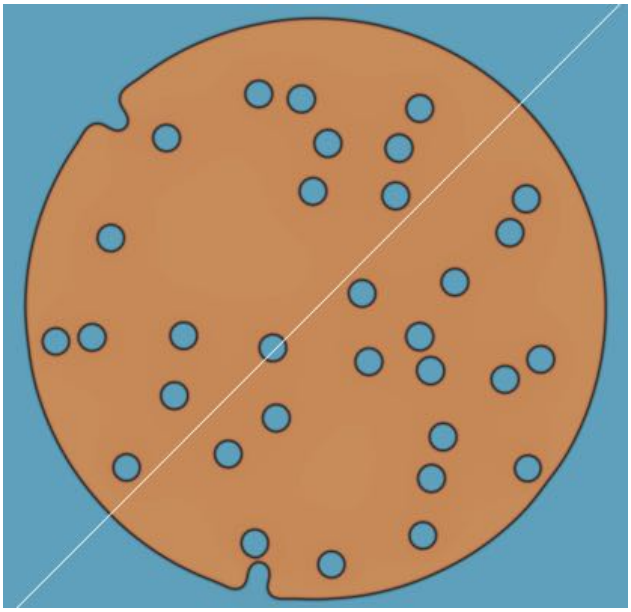

Figure 3.9: Example line sample object in Paraview. The value of ϕ is sampled along the white line at each time step. The outermost points at which ϕ goes to a depressed value are used to compute the size of the system.

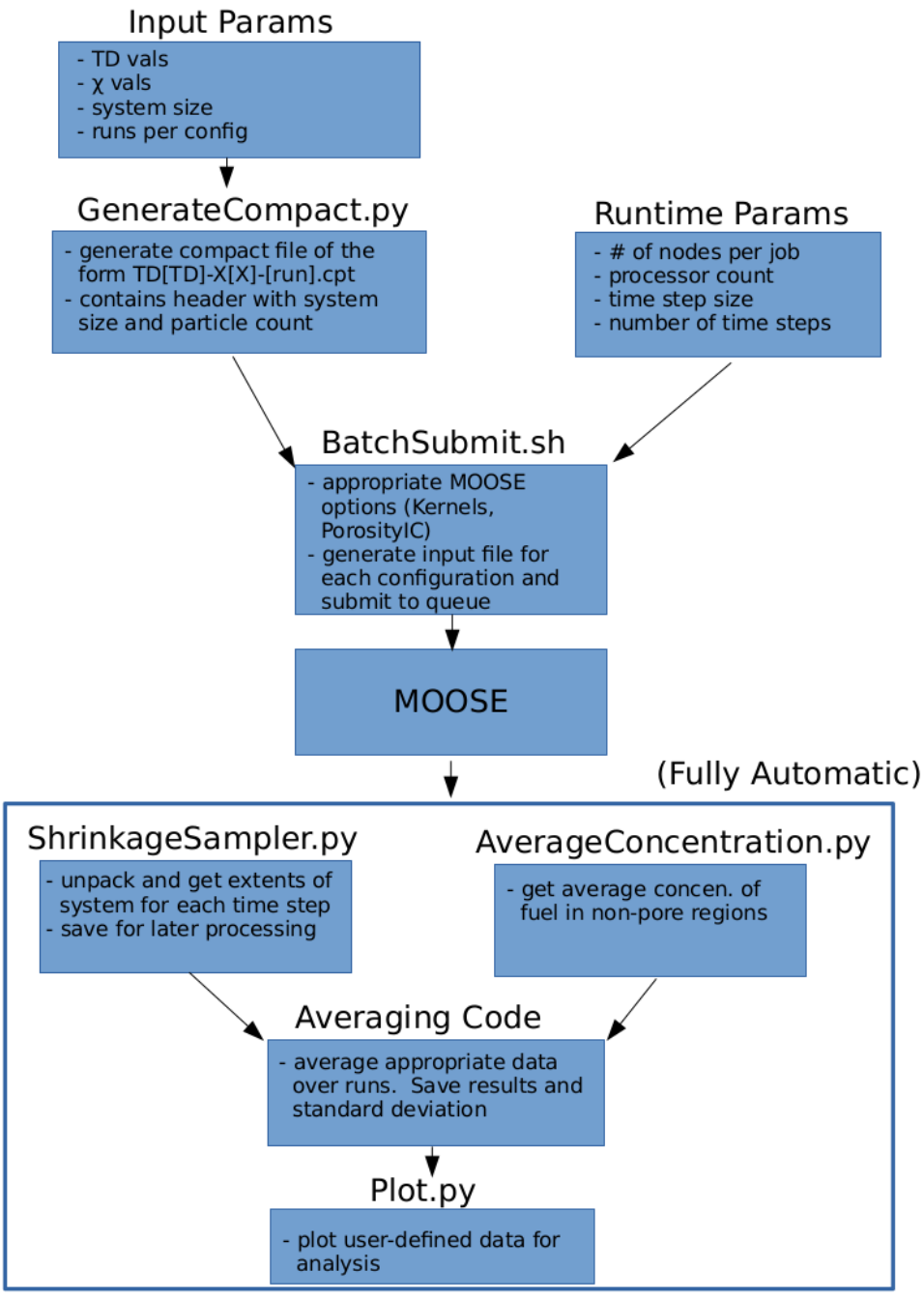

Figure 3.10: Steps involved in the generation, execution, and processing of the simulations.

4 Results

4.1 Introduction

This section summarizes the results obtained from the simulations, and provides an interpretation of them. On the whole, it is shown that the introduction of the bimodal pores greatly improves the ability of the microstructure to resist porosity loss. The time required to reach an equivalent fully dense state in comparison to microstructures without bimodal pores is extended. The greatest relative improvement is seen late in the annealing process. We present here selected results, primarily focused on the $\chi = 100, 60, 40$ and 0 cases. We consider $\chi = 100$ the baseline monomodal configuration fabricated via traditional techniques. The $\chi = 40$ and 60 cases are the most intriguing bimodal configurations. At $\chi = 0$, the configuration is comparable to the $\chi = 100$ case, but with larger pores present. It is useful in benchmarking the behavior of the other configurations. As a preliminary note, most images follow the color scheme of orange corresponding to fuel material, and blue to pore regions or the fuel exterior.

4.2 Qualitiative Results

4.2.1 Compact Generation

In Figure 4.1, a sampling of the microstructures generated for MOOSE by the compact generation algorithm are shown at the $TD = 92\%$ value. Here, we see both the size of the pores in comparison to that of the overall structure and the ratio of the two pore sizes. On close inspection of Figure 4.2, we observe that a few large pores have been placed near

the outermost surface of the fuel by random chance. This behavior is observed in many configurations, and during evolution contributes to deformation of the fuel surface. The pores produce sharp surface features on the fuel body, which are then smoothed out with continued evolution. This deformation behavior is not easily observable for structures with a majority of small pore regions, owing to their small size and subsequent reduced ability to modify the surface.

From the images, we become convinced that the systems are sufficiently random for our needs. The images shown indicate the ability to generate microstructures with the two parameters of interest (TD and χ) for the ranges given in the parameter space.

We are also concerned with the choice of grid resolution, as it is important that interfaces be resolved over a few elements. In Figure 4.4, we see that the interfaces are only resolved over one node; this is to be expected, as we assign the order parameter discretely at each point, and do not initially interpolate its value. By T=1, however, the interfaces have extended to the desired width (see Figure 4.5), and continue to maintain this size throughout the rest of the simulation. Note that when we parameterize the system size (near the end of the results section), the element count is adjusted to maintain the desired resolution, although a graphic of such will not be shown.

4.2.2 Shrinkage Behavior

Several example evolutions of the different microstructures are presented in Figure 4.6. The systems are first shown in the initial configuration, and then at equivalent time steps later in the simulation. In this image, all configurations displayed are at the same total initial porosity ($TD = 92\%$), but by T=80 it is clear that $\chi = 100$ has experienced almost complete

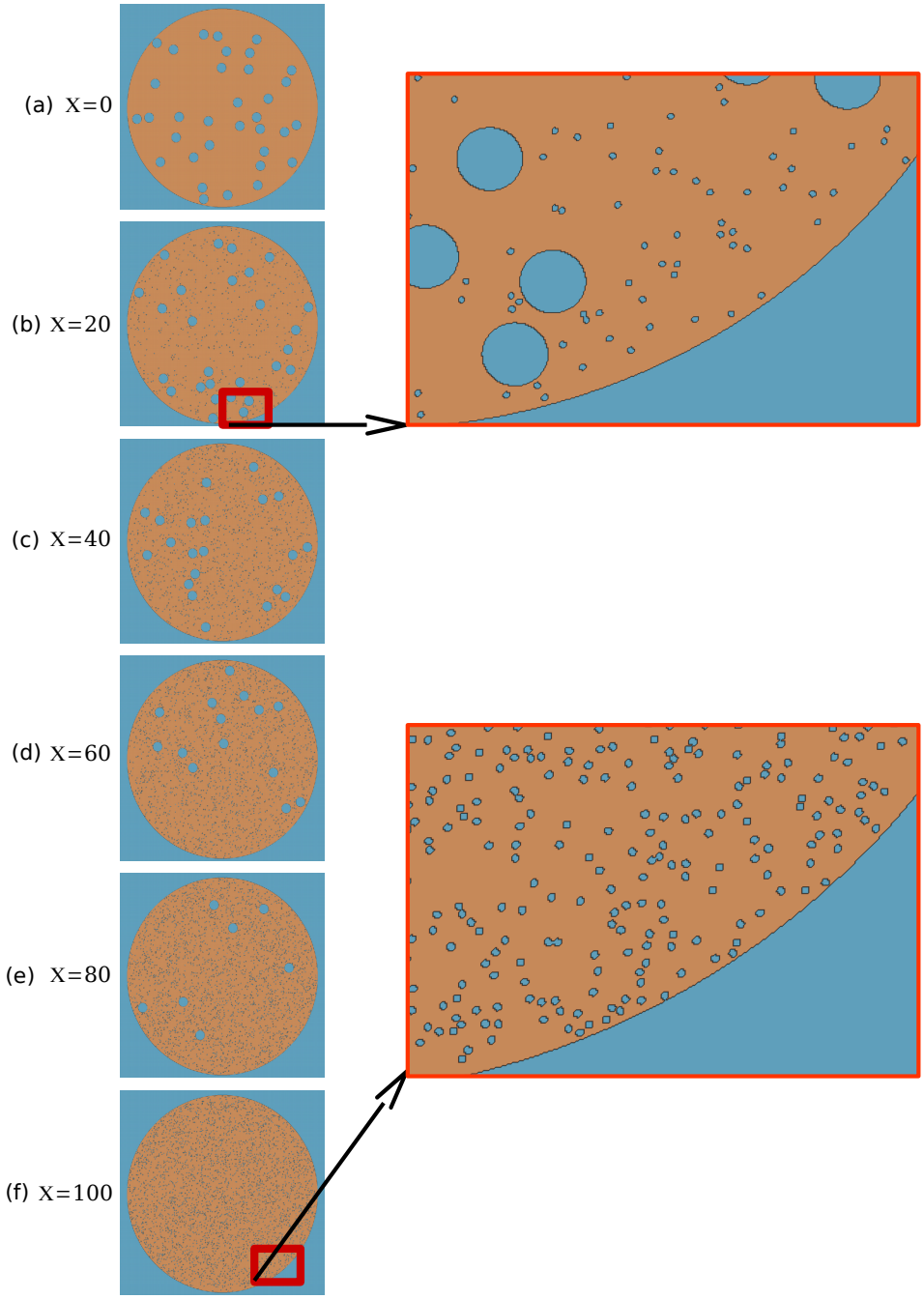

Figure 4.1: Example configurations generated by random void placement. Each configuration has convincingly random placement, based on visual inspection. Zoomed views highlight the relative sizes of the pores.

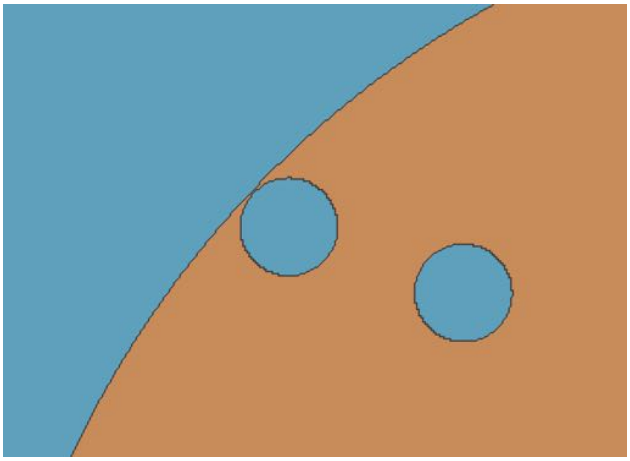

Figure 4.2: Zoomed view of a large pore in close proximity to the outer surface. The edge of the pore is only a few grid spacings from the fuel material termination. This often resulted in surface deformation, requiring several diameter samples to produce a reliable area estimate.

porosity loss, shown by the elimination of the yellow regions. The other configurations have persisting pores. This is evident at the remaining TD values as well, with the evolution to fully dense in general occurring in a shorter period of time, owing to the decreased total pore space that must be eliminated. The small vacancy sites, initially concentrated in the small pores, are rapidly dissolved into the fuel matrix, and by T=1, they are mostly hidden from visual inspection, as shown in Figure 4.7. This is in part due to the time step value used, as a reduction shows greater persistence of these pores. As the generation algorithm employed resulted in sharp interfaces between the pores and fuel (the interface is initially resolved over only a single element), the corresponding interface free energy is excessively large, and simulation in time will immediately eliminate these pores except in the smallest of time steps. This fact was not found to be problematic, however, as simulation at a reduced time step (see Figure 4.8) did not result in significantly different behavior. The coarse time step was therefore adopted for computational expediency.

In some cases, especially for structures with many small pores, it is observed that

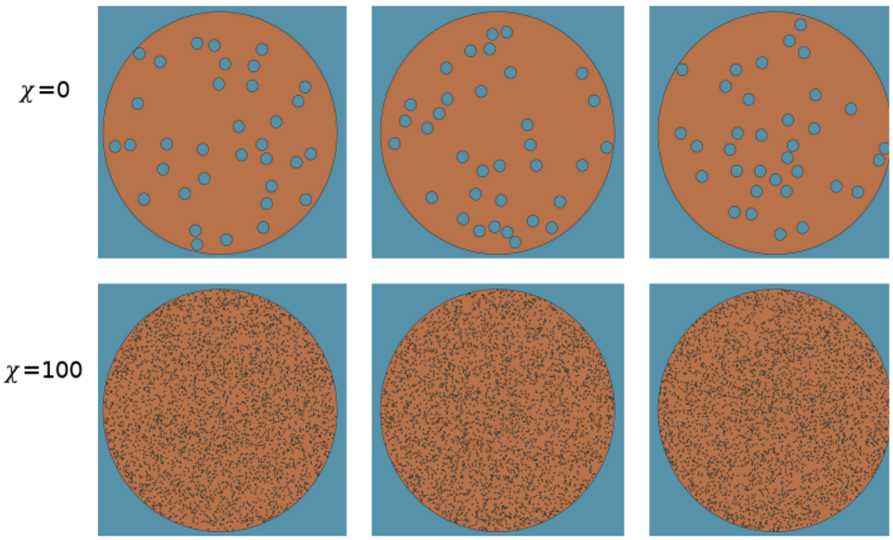

Figure 4.3: Several configurations at T=0 highlighting the random placement of pores. With sufficient samples for each configuration, a reasonably averaged spatial behavior is obtained, especially for the configurations with large χ.

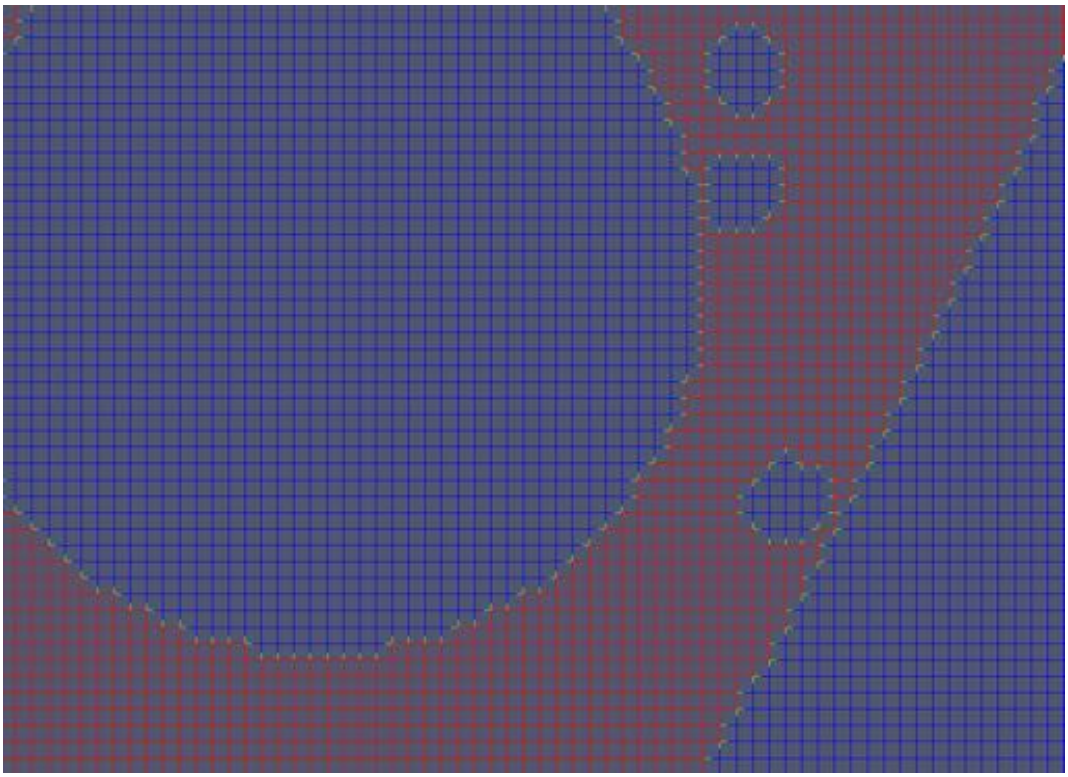

Figure 4.4: In the image, the finite element grid is shown overlaid on the concentration parameter. The bottom right of the image is the outer boundary of the fuel compact, with pores of both sizes visible within. Initially, the interfaces are sharp, owing to the method by which ϕ is assigned in PorosityIC. Here, we have adjusted the color scheme to make the grid easier to see, with blue denoting a pore and red fuel.

intermediate sized pores would occasionally nucleate and grow for some time before eventually being eliminated (Figure 4.9). The high density of mobile vacancies sourced from the small pores makes such nucleation feasible, and once it occurs, temporary growth can be energetically favorable, as this reduces the curvature and hence the interface energy of these nucleated regions. While growth can occur, no nucleated region will posses lower energy than the system's outer surface, resulting in the eventual elimination of the temporary void. We can observe a similar effect for structures with large pores, some of which are also capable of temporary growth Figure 4.10. The vacancies sourced from small pore regions, having been

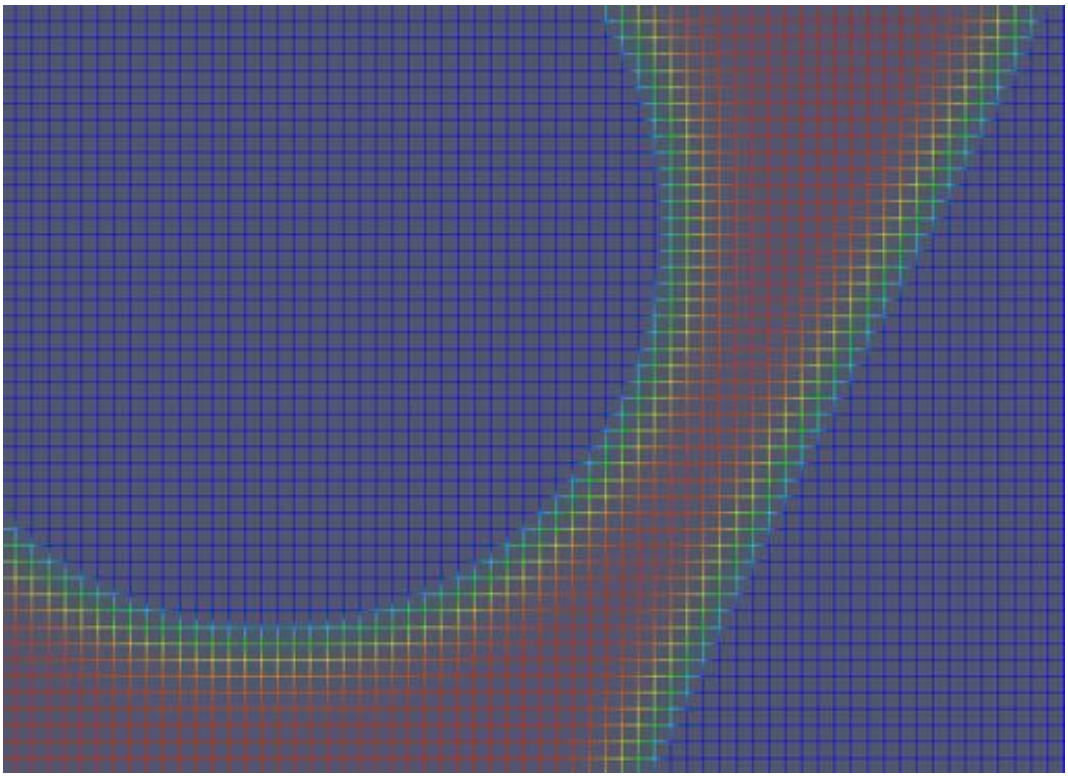

Figure 4.5: By T = 1, the interfaces have widened to the point at which they are resolved by around four grid elements. We know this to be sufficient in capturing the details of the Cahn-Hilliard model. Again, blue denotes pore space and red fuel, with intermediate values observed at the interfaces.

rapidly dissolved, migrate to the surface of the fuel but are interrupted by these large pore regions. Some thus contribute to large pore growth. These pores are again temporary, but on average persists for longer in the simulation than the intermediate nucleated sites, owing to their larger size.

4.3 Quantitative Results

4.3.1 Shrinkage Behavior

Plots are given comparing the shrinkage rates of selected configurations, along with the standard error bars, in Figures 4.11, 4.12, and 4.13. It is immediately evident that the

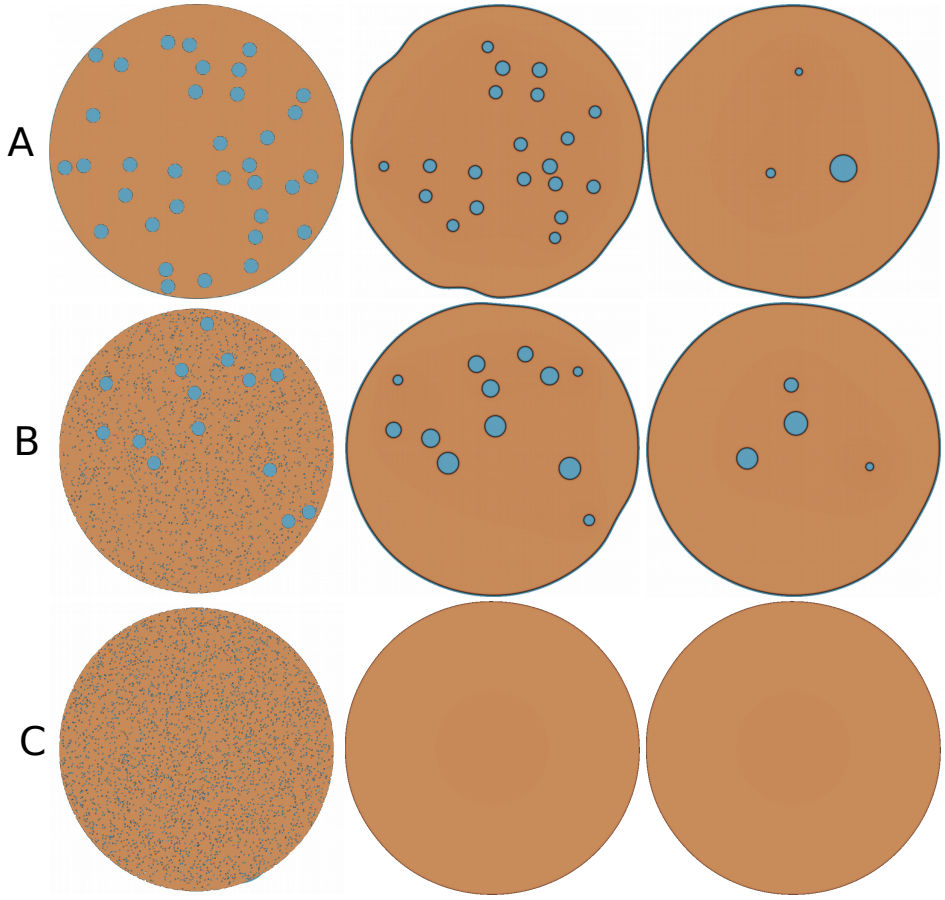

Figure 4.6: Evolution of three configurations ($\chi = 0, 60, 100$) at $TD = 92\%$. At T=0 (left column), the systems have not begun evolution. T=20 (middle column) shows the small pores have completed dissolution within the fuel matrix, with some surface deformation apparent for $\chi = 60$ and 0. At T=80 (right column), significant void space is lost for all configurations.

(a)

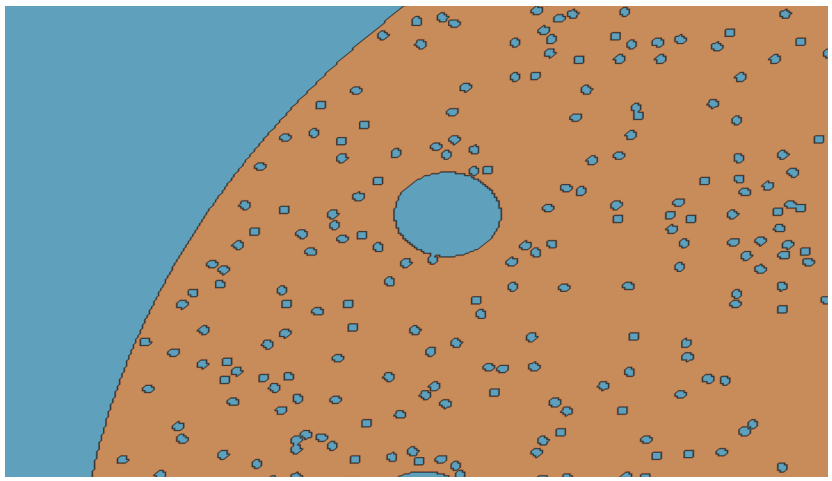

(b)

Figure 4.7: At T=0 (a), the theoretical as-fabricated condition is shown. One time step later, all visual evidence of the existence of the small pores has disappeared. Despite this fact, the bimodal configurations exhibited different behavior versus the monomodal structures.

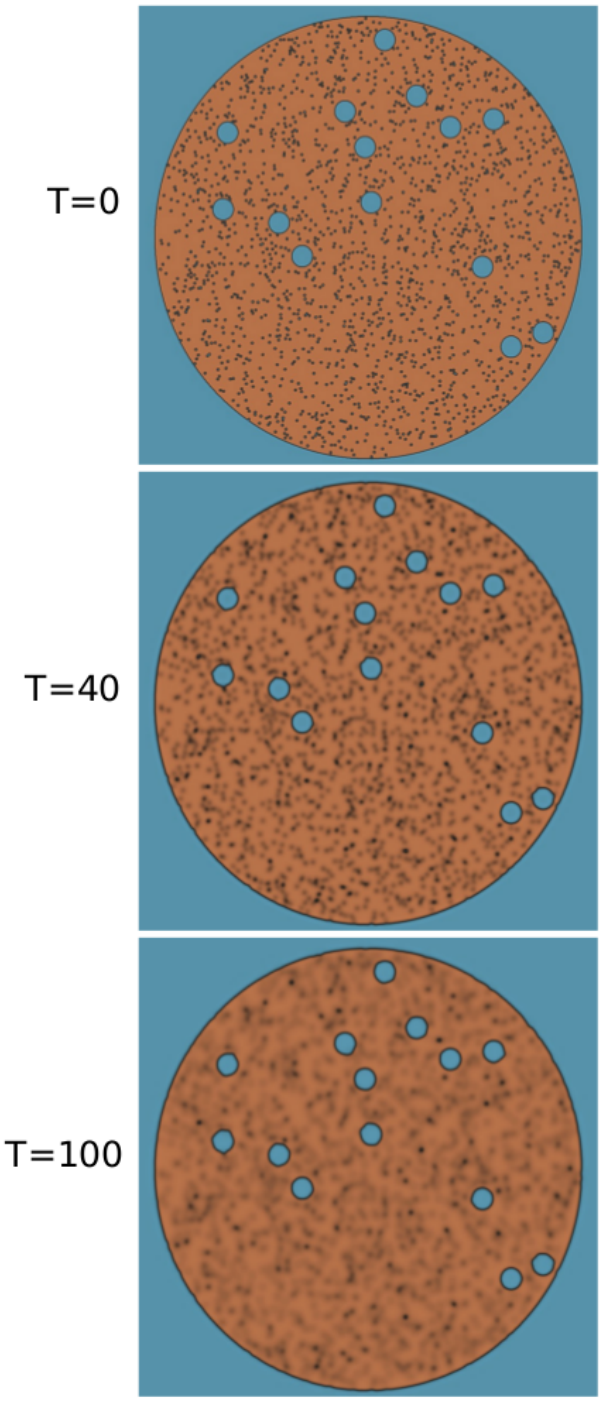

Figure 4.8: At a reduced time step of dt=0.001, vacancy dissolution from the small pores is captured in greater detail. The blurred features are evidence of early diffusion, which is required for absorption in the extremely vacancy rich region directly surrounding the small pores. Figures from $TD = 92\%$ for $\chi = 60$.

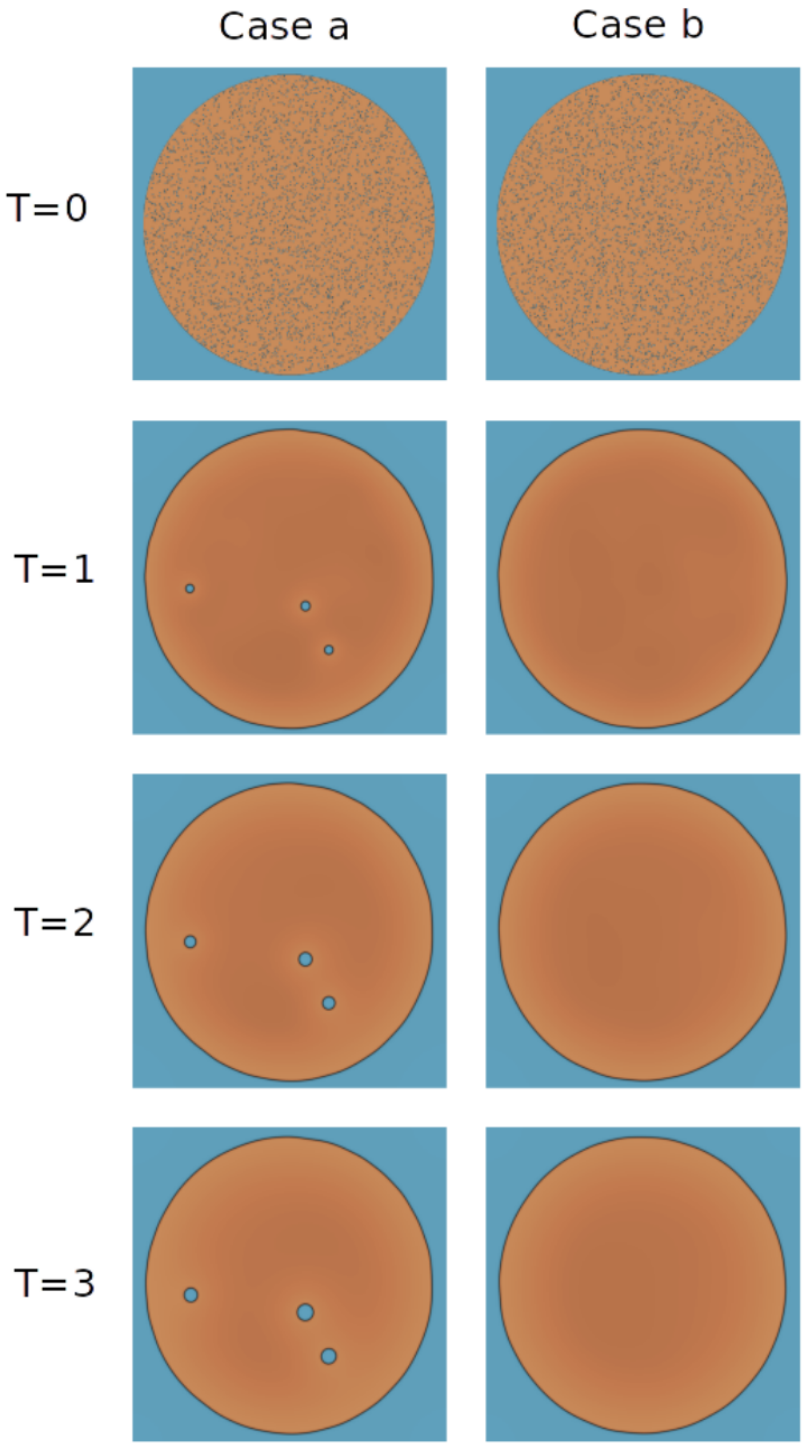

Figure 4.9: Nucleation of intermediate pores from vacancy diffusion. Two cases are exhibited here: in (a), pores are nucleated from vacancies soured from the small pore regions. In (b), no pores are nucleated.

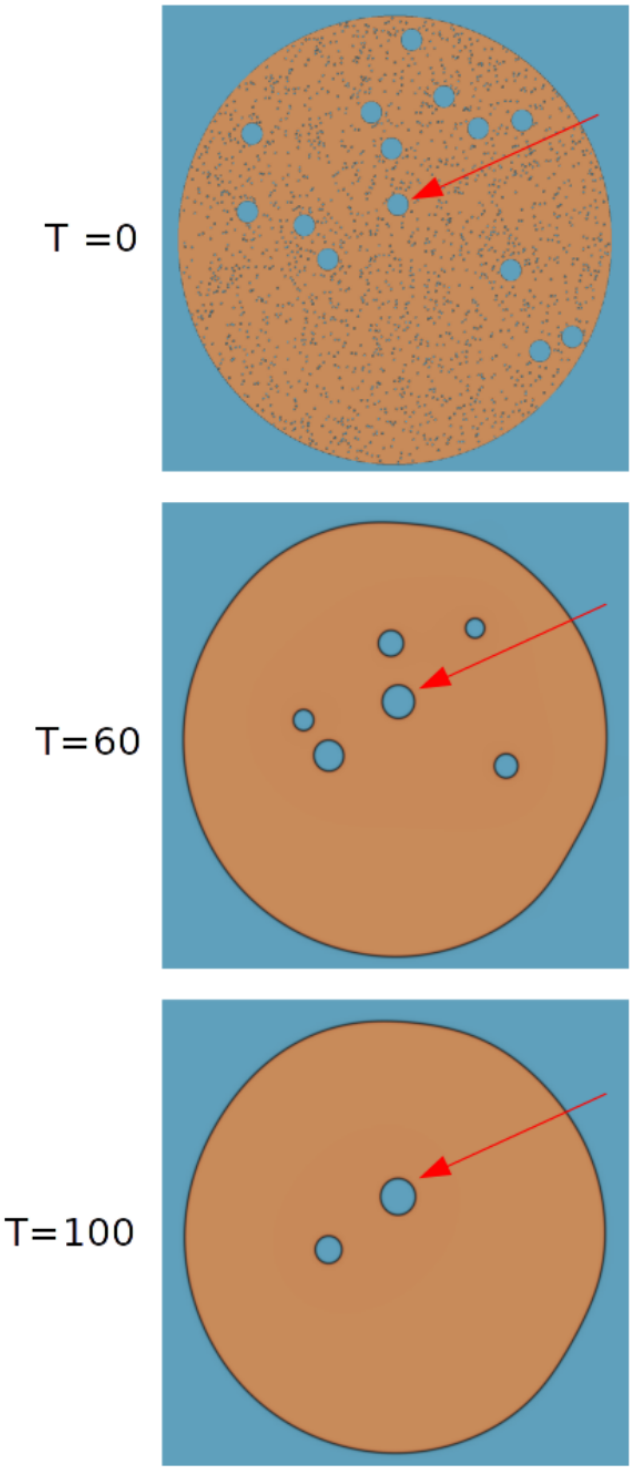

Figure 4.10: A large pore grows, partially as a result of free vacancies sourced from small pores. The evolution here is common in the bimodal configurations and is believed to contribute to their superior resistance to densification. Images from $TD = 92\%$ and $\chi = 60$.

$\chi = 100$ configuration experience rapid porosity loss across the configuration space. This is consistent with real-world behavior at annealing conditions; the elevated temperatures drive vacancy diffusion until eventually all pore space is lost. In the $\chi = 0$ case the behavior is the same, but the larger initial pore sizes mean that the interfaces are more energetically favorable than the smaller ones, resulting in more annealing time required to eliminate them. In fact, we observe that many systems at this χ value do not reach the fully dense state by the end of the simulation time. The bimodal configurations, best exemplified by the configurations with $\chi = 40$ and $\chi = 60$, in all cases outperformed the baseline monomodal structures ($\chi = 100$) in regards to their porosity loss rates.

At $TD = 94\%$, significantly larger error bars for $\chi = 0$ made comparison between it and the bimodal configurations difficult. The error observed is attributed to two primary effects. The first is concerned with the random placement of the voids, captured in two error parameters. The first of these parameters is the average spacing between pores (Figure 4.14). For the $TD = 94\%$ case, the variance in this parameter is greatest, and is believed to help contribute to the variation in observed shrinkage rate. Another parameter of interest is the average distance of pores to the surface of the fuel (Figure 4.15). Again, the $TD = 94\%$ cases exhibits the greatest variability.

While these parameters explain some of the noise exhibited in the data, the primary cause is believed to be the simulation size and corresponding surface effect. Because the diffusion path is relatively short, any deviation among configurations will have a strong influence on the overall kinetics of the system. To remedy this problem, more samples of the current size could be run, in the hopes of establishing a more consistent dataset. Also investigated is an increased system size, but hardware limitations require a reduced

parameter space. Given the current analysis, the trends are sufficiently resolvable among the configurations of greatest interest that additional runs were not strictly required.

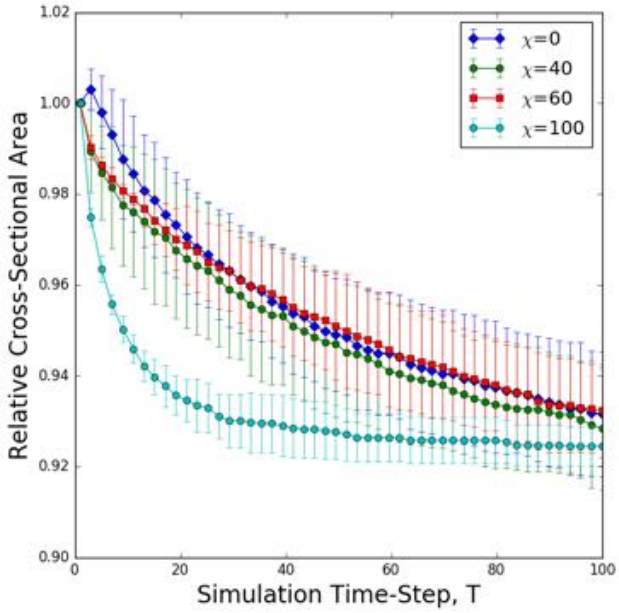

Figure 4.11: Area change rate at $TD = 92\%$. The $\chi = 100$ case experiences rapid loss of porosity in comparison with $\chi = 0$, owing to the smaller pore size. The intermediate cases, $\chi = 40$ and 60, follow the $\chi = 0$ behavior, although significant pore area is taken by the small pores.

4.3.2 Vacancy Concentration

In Figures 4.16, 4.17, and 4.18, the vacancy concentration throughout the entire system is averaged, excluding regions that are classified as pores. With this, we have a measure of the solution concentration of vacancy sites within the fuel body, and can make observations about the diffusion of these vacancies and their subsequent transport. Starting again with the $\chi = 100$ case, we see a rapid initial spike in the dissolution concentration, followed by a reduction to a small constant value as nearly all the vacancies migrate to the fuel's outer surface. At this point (around T=40 for most cases), the systems have reached

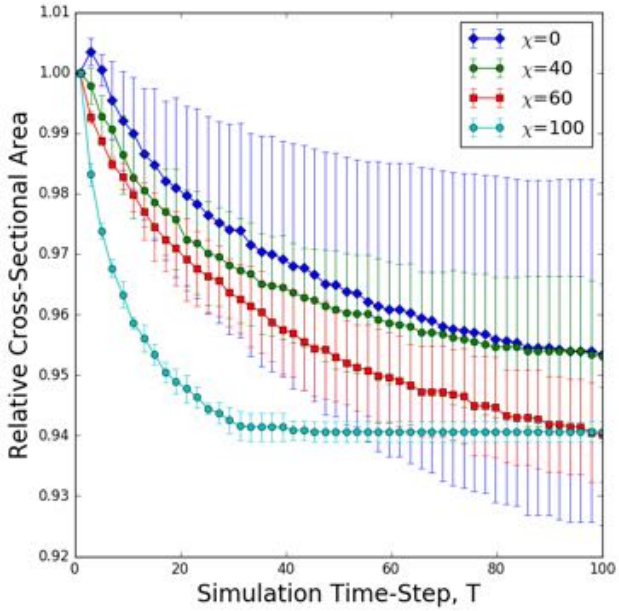

Figure 4.12: At $TD = 94\%$, there is significant noise in the $\chi = 0$ case. Trends for the other χ values at this TD are consistent with their analogues, however.

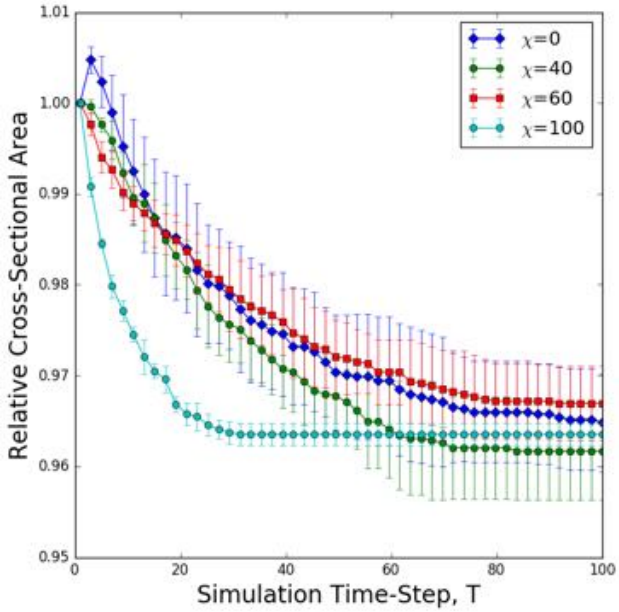

Figure 4.13: $TD = 96\%$ shows bimodal configurations that outperform the $\chi = 0$ case in long term behavior. Here, the $\chi = 100$ experiences the most rapid loss of porosity.

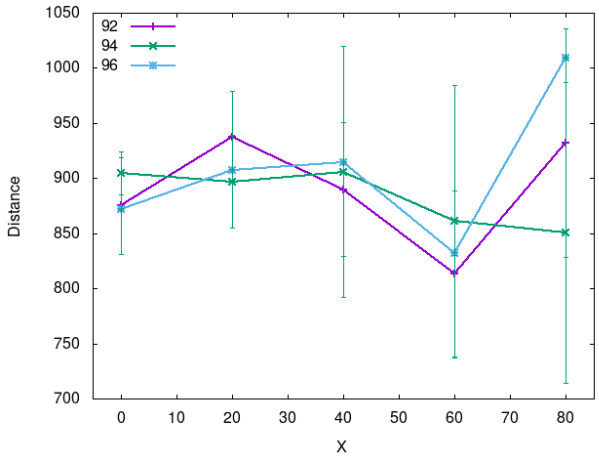

Figure 4.14: The interpore error metric, showing the average variation on the distance between large pores at initialization for each configuration. The variation shows little applicability to shrinkage kinetics, but highlights the $TD = 94\%$ case in that the greatest variability is seen here. This helps elucidate the noise seen in the shrinkage behavior for this case.

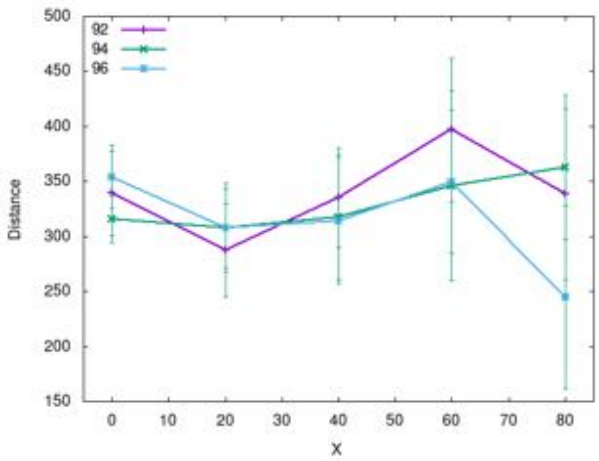

Figure 4.15: Here, the average distance of a large pore to the surface of the system is shown at initialization. Again, the greatest variance is seen for the $TD = 94\%$ case.

the fully dense state, with very few vacancies remaining.

This behavior is contrasted with the $\chi = 0$ case, where the sharp increase in concentration is subdued, and a longer "tail" exists where the vacancies remain dissolved within the fuel for some time. A spike is expected, of course, owing to the sharp interface created by the initialization algorithm. An interpretation of this behavior considers the surface of the pores at the initial state. High gradients drive the vacancy sites from the pore surface into the bulk fuel region. As these vacancies migrate away, the pore surface area decreases, resulting in progressively lower available reaction surface area, slowing pore shrinkage. As the system is evolved, more and more vacancies are removed from the pores, until with sufficient annealing time all are lost and the pores are destroyed. The fact that these large pores are capable of persisting for extended periods of time is noted.

At intermediate χ values, the advantage provided by the large pores is remarkable. Specifically, the bimodal configurations show spiking that is very similar to the magnitude experienced by $\chi = 0$, even though half of the pore area is occupied by small pore regions. As the small pores dissolve (a fact that is visually evident), the vacancies sourced from these regions are not immediately lost to the environment. The fact that the average vacancy concentration is higher suggests one of two behaviors: the vacancies congregate at the large pores, or quickly escape the fuel system. The compacts' exhibiting lower shrinkage rates seems to negate the second idea, and the frequent growth of the large pores supports the first theory. Furthermore, the long term behavior of the vacancy concentration is also similar to the $\chi = 0$ case. This indicates that considerable void space still exists within the fuel, and is being removed at considerably lower rates.

In all but one data series, the error observed here is minimal. The exception is with

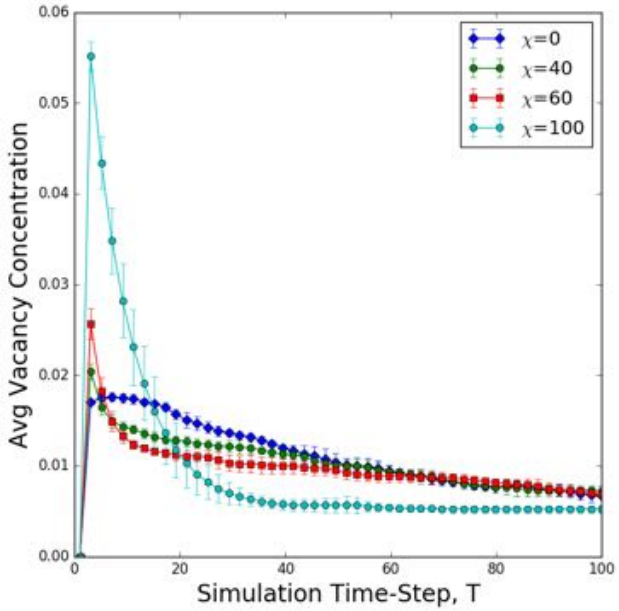

Figure 4.16: Measured in non pore regions, the average vacancy concentration spikes at early time steps in the $\chi = 100$ case, leading to large vacancy diffusion gradients and subsequently rapid transport. The effect is not as pronounced for the other configurations. The persistence of porosity is evidenced by the higher sustained vacancy concentration at extended time steps. Data shown for the $TD = 92\%$ case.

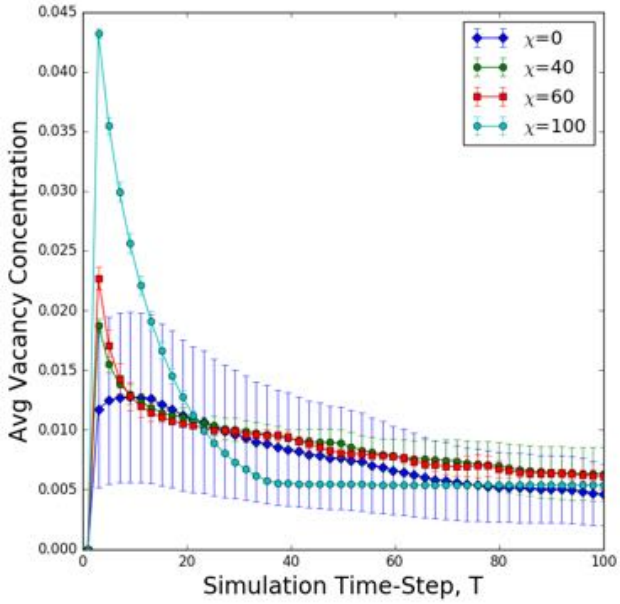

Figure 4.17: At $TD = 94\%$, high variance is again observed for the $\chi = 0$ case. The other configurations show good precision, however. The behavior otherwise follows the $TD = 92\%$ case.

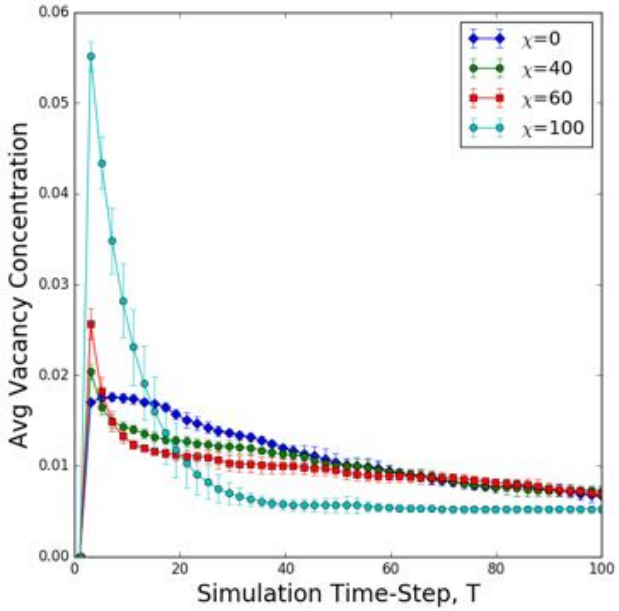

Figure 4.18: The bimodal configurations ($\chi = 40$ and 60) perform as good or better than the $\chi = 0$ case at $TD = 96\%$. Full densification occurs earlier than the other TD cases (when the plots reach an asymptote), owing to the low total initial porosity.

the $TD = 94$, $\chi = 0\%$ case. This error is again attributed to the random placement of the pores and small relative system size.

4.3.3 System Size Parameterization

All results shown to this point are for systems with the same Diameter, namely D = 1024 (dimensionless length units). We have stated previously that the size ratio between the large pores and the total system size is low (10^{-1}), and wish to explore other system sizes to understand if surface effects are contributing to our observation of the bimodal effect. Table 4.1 describes the configurations simulated; specifically, systems with sizes both halved and doubled in comparison to the original size are simulated.

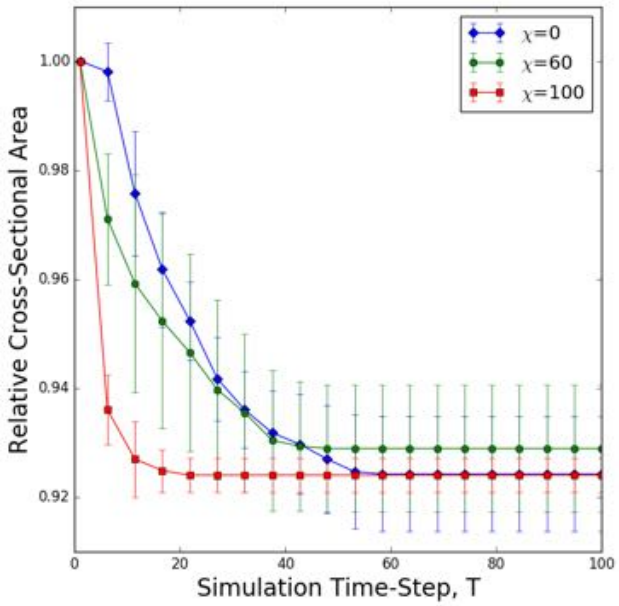

Figure 4.19: At a reduced system size of D = 512, rapid densification for all systems is observed. This is expected, as the average distance a vacancy must travel to escape the system is reduced. The bimodal configuration ($\chi = 60$), continues to follow the behavior of $\chi = 0$.

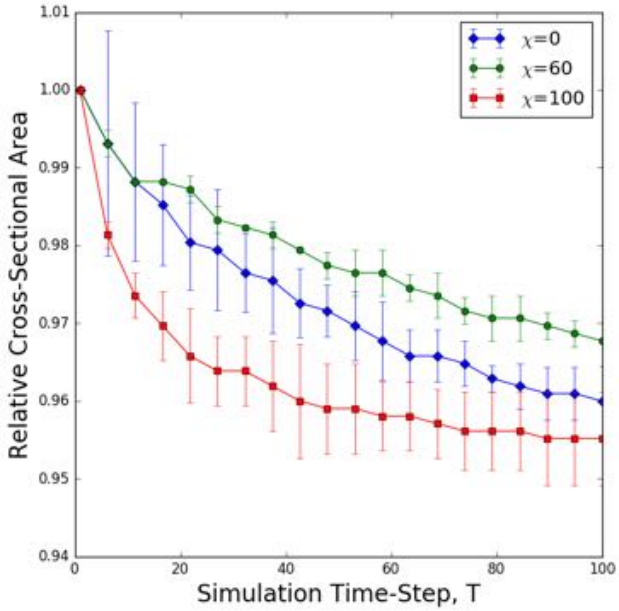

Figure 4.20: Doubling the system size (D = 2048) shows the bimodal configuration continuing to outperform the monomodal case. All systems exhibit slower kinetics than the base system size, owing to the much large diffusion path required.

System Size	Parameters
D = 512	TD=92, χ = 0,60,100
D = 1024	All configs.
D = 2048	TD=92, χ = 0,60,100

Table 4.1: Size parameterization space.

4.3.4 Discussion

Configurations with only small pores represent a microstructure that can be fabricated using standard sintering techniques. Densification in these configurations is rapid, both from experimental experience, and from the results of this simulation. The initial high total surface area of the pore-solid interface results in considerable excess interfacial energy. This imbalance drives the production of large diffusion gradients that enable rapid vacancy dissolution and subsequent transport to the surface of the body. Because regions of pore re-nucleation are relatively sparse (in terms of the area they subsume, rather than their frequency of occurrence), the diffusion pathway for vacancies is rather direct, and combined with large diffusion gradients results in rapid transport and the resulting densification.

With purely large pores, we again consider the location of vacancies, but must be reminded that most of them are located in the interior of the large pores. Thus, the quantity of vacancies available for diffusion is limited by surface area of the evolving pores. Furthermore, relative stability of the lower curvature interface results in pores with greater longevity. The corresponding total driving force given to the transport of the vacancies is considerably lower for the duration of the simulation, resulting in lower densification rates.

This result is also intuitive; larger pores are expected to require longer annealing times to eliminate. Occasional re-nucleation of intermediate pores or temporary growth of existing pores is observed, and further slows the densification process.

The bimodal cases of greatest interest are at $\chi = 40$ and 60. Here, we see that the small pores present in these systems are quickly eliminated, just as for the $\chi = 100$ case. The existence of large pores in these structures inhibits transport of their vacancies in two ways. In the first, vacancies that are bound for the surface of the system are often interrupted in their straight-line path out of the system. This has the effect of increasing the diffusion length required for their removal. Secondly, some vacancies are absorbed into large pores after being dissolved in the fuel matrix. Clearly, these vacancies will require much longer to complete their diffusion out of the system, as large pores are often stable for considerable time. We can see from Figures 4.16, 4.17, and 4.18 that at $\chi = 100$, a considerable spike in vacancy concentration is associated with the large diffusion gradients and rapid transport of the vacancies. These spikes are considerably subdued in the bimodal cases, even though significant total pore volume is occupied by the small pores. This fact, that the existence of large pores impedes the ability of vacancies sourced from small pores to freely diffuse within the system, is the key benefit of the bimodal pore structures simulated. The bimodal configurations also show increased values of vacancy concentration at extended simulation time. The result here is somewhat counter-intuitive: the existence of gradients, while detrimental at early time steps, is evidence of continued porosity transport at longer annealing time. The bimodal configurations are slower to eliminate these gradients, and thus densify over a much longer period of time than the $\chi = 100$ case.

The results of the size parameterization study are encouraging. The systems originally

simulated have on the order of 1000 total pores (in the case of $\chi = 100$), whereas realistic fuel pellets have millions of pores to reach the equivalent porosity. This discrepancy is a cause of concern in that the systems simulated may be exhibiting the improved densification behavior purely as a consequence of surface effects. From Figure 4.19 and 4.20, we continue to observe the bimodal configurations outperforming those with no porosity control. Particularly, we see no trend in the improvement as the system size is varied. Interestingly, the bimodal configuration outperforms the $\chi = 0$ case by a significant margin. The cause of this is not clear, although we caution that in the parameterization, fewer total runs are performed.

Fabrication routes for production of the bimodal configurations are under current research, as mentioned in the literature review. The elimination of small pores from the fuel compacts is difficult (barring samples that are already fully dense), but the addition of large pores through the pore forming technique can be deliberate. With this, we envision configurations analogous to the $\chi = 40$ or 60 case, and with the corresponding densification performance comparable to the values found in the results. The ability of the bimodal configurations to outperform the monomodal small configurations motivates further study of other configurations that may provide even greater benefit.

4.4 Validation

An important step in any study is validation of results. For physical experiment, quantification of error is necessary but not sufficient in testing a theory of some phenomena. Often, simulation is used to verify a model and ensure that the theory is sound, rather than just correct on the given data by chance. In simulation, the burden is perhaps greater, as the complex interactions that make up the physical world are greatly simplified into a model

that is computationally tractable. Thus, results on the computer, while they may be correct from the standpoint of a given model, may not extend into the real world if sufficient care is not taken in understanding that model's assumptions and applicability. In addition to the model being correct, we must also verify that a given program used in implementing a model does so honestly, that is, no programming errors must exist that give erroneous results. These two sources of error must be considered in any computational study.

The code correctness problem is well considered by the choice of MOOSE as the primary analysis tool. The finite element method is well developed, both mathematically and in software. The particular physics packages utilized from MOOSE are also validated by several external studies. In addition, the large community surrounding MOOSE and continual development on it provides considerable confidence that results generated by MOOSE are a faithful and accurate reproduction of the model described in the methods section, which is itself mathematically well supported.

Consideration of the model's applicability to the problem at hand is more difficult. Certainly, the Cahn-Hilliard equations have been applied with considerable success before. Some assumptions made in simplifying the annealing process are cause for concern, these assumptions are addressed in the discussion on future work. We are encouraged to consider the results as insightful, although perhaps not directly applicable to a specific fuel design. We are fortunate in that in tandem with this computational study, a fabrication effort is underway that seeks to reproduce our results in depleted-uranium fuel pins. Cooperation with this work has enabled both studies to advance in similar directions, which will considerably improve the ability to make direct comparisons and validate each group's results.

5 Conclusion

5.1 Summary

There is considerable interest in both academia and industry directed towards next generation nuclear power systems. These systems are expected to operate at lower cost, and to do so with a greater degree of reliability and safety. Additionally, they are expected to be free of some of the restraints imposed on current systems. Closing the nuclear fuel cycle, either in part or in whole, is a major goal, and key to this goal is the design of systems that enable significantly higher burnup. Metallic fuels exhibit an attractive combination of utility and efficiency, owing to their advantageous combination of high initial heavy metal density and excellent thermal conductivity in comparison to oxide fuel forms. This combination makes them a viable candidate to consider in a next-generation design.

Zirconium-alloyed uranium fuels have been used in research reactors in the past, and significant operating experience with them is possessed. Although good chemical compatibility with some reactor designs is enjoyed, their tendency to swell excessively at high temperature has made their adoption in power reactors problematic, with the primary mitigation strategy (increase in the fuel pin plenum size) leaving much to be desired. Further development is necessary in order to realize the greatest benefit of these fuels.

Modern material design is often driven by control of material morphology and behavior at the μm length scale, known as the microstructure. Control of microstructure features through novel fabrication routes, such as powder metallurgy and sintering, allows for precise specification of various material properties. In this work, we specifically target the size and

distribution of porous regions within the fuel. Previous work by [15] has experimentally demonstrated oxide fuel formulations with bimodal pore size distributions as exhibiting superior resistance to densification during sintering and subsequent extended annealing, partially reproducing the environment expected in high power reactor operation. This fact, if extensible to metallic fuel formulations, could provide a pathway to fuel formulations with specific microstructure specifications that alleviate the aforementioned limitation, and enable their use in production reactors.

We have developed a computational model capable of simulating the extended annealing of solid porous bodies that can be easily extended to specific metallic fuel formulations. The Cahn-Hilliard equation of the phase field family of methods provides a mathematical description of the annealing problem, and its implementation in the MOOSE finite element framework provides flexibility and scalability. Analysis tools utilizing Paraview's visualization capability were developed that are capable of quantifying the relative densification rates of a range of microstructure configurations, including monomodal configurations typical of standing casting and sintering techniques, and bimodal microstructures with intentional porosity added. A large parameter space is explored, with consideration of statistical variation included.

It is shown that bimodal configurations provide superior resistance to late stage densification in comparison to structures with monomodal small pores. The addition of large pores is thought to inhibit the transport of vacancies to the outer surface of the system, which follow diffusion pathways with the purpose of minimizing the surface free energy created by phase boundaries (fuel-pore interfaces). Without large pores, the vacancies are free to propagate to the fuel surface, and densification to near theoretical maximum levels occurs

quickly. Large pores obstruct these pathways, both extending the distance over which diffusion must occur and providing collection sites that are energetically favorable for temporary pore vacancy accumulation. While these enhanced pore regions are eventually eliminated, their persistence at extended annealing times is valuable in preventing rapid densification.

5.2 Future Work

Future work will address the influence of crystallographic orientation and size of grains within a metallic fuel configuration. The grain boundaries of the material are expected to have some effect on the diffusion pathways presented to vacancies, as it is common for the mobility of vacancies along grain boundaries to be considerably enhanced. Thermal gradients as a result of nuclear heat generation and convective cooling of the fuel pin surface will alter the kinetics of vacancy transport, primarily by adjustment of the effective mobility of the vacancies, but also considering compositional changes of the U-Zr alloy across the body cross section. The inclusion of a temperature gradient is a straightforward addition within the given MOOSE framework, but consideration of compositional changes and crystal orientation will require some development. Additionally, the inclusion of radiation-induced dislocation production will also act to modify vacancy mobility. Simulation of such behavior is possible within MOOSE, but its development is still limited. Fission gas production should be investigated through irradiation experiments. A follow on study for this, as well as physical irradiation of example fuel pellets is planned.

The work that has been described herein is part of a broader Multiscale study involving multiple members (Deo, Georgia Institute of Technology as P.I. 2, Mcdeavitt, Texas A&M as P.I. 3, Mariani, Idaho National Laboratory as P.I. 4). Microstructure parameters

that are realistic for a depleted-uranium alloy fuel will be provided by P.I. 2 in a continuing study to produce more realistic predictions. The fuel configurations of greatest interest will be fabricated and annealed by P.I. 3 for verification of results, and eventual irradiation with P.I. 4.

Bibliography

[1] H. Bailly, D. Mnessier, C. Prunier, and S. Simpson, *The nuclear fuel of pressurized water reactors and fast neutron reactors design and behaviour*. Lavoisier, 1999.

[2] N. E. Todreas and M. S. Kazimi, *Nuclear systems*. Taylor & Francis, 2011.

[3] G. K. J. Lanning D. D., Beyer C. E., *FRAPCON-3 updates, including mixed-oxide fuel properties*. The Commission, 2005.

[4] Y. e. a. Kim, "Thermal conductivities of actinides (u,pu,np,cm,am) and uranium-alloys (U-Zr, U-Pu-Zr, and U-Pu-TRU-Zr)." *Journal of Nuclear Materials*, vol. 445, p. 272, 2014.

[5] T. Sofu, "A review of inherent safety characteristics of metal alloy sodium-cooled fast reactor fuel against postulated accidents." *Nuclear Engineering and Technology*, vol. 47, no. 3, pp. 227–239, 2015.

[6] S. B. Walters L.C., Kittel J.H., "Performance of metallic fuels and blankets in liquid-metal fast breeder reactors," *Nucl. Technol.; (United States)*, vol. 65:2, May 1984.

[7] A. Solomon and S. Mcdeavitt, "Preparation of uranium-zirconium alloy nuclear fuel elements by pm," *Metal Powder Report*, vol. 47, no. 11, p. 55, 1992.

[8] W. D. Kingery and M. Berg, "Study of the initial stages of sintering by viscous flow, evaporation–condensation, and self-diffusion," *Sintering Key Papers*, pp. 367–382, 1990.

[9] D. L. Johnson and I. B. Cutler, "Diffusion sintering: I, initial stage sintering models and their application to shrinkage of powder compacts," *Journal of the American Ceramic Society*, vol. 46, no. 11, pp. 541–545, 1963.

[10] R. Raj and R. Bordia, "Sintering behavior of bi-modal powder compacts," *Acta Metallurgica*, vol. 32, no. 7, pp. 1003–1019, 1984.

[11] E. Arzt, "The influence of an increasing particle coordination on the densification of spherical powders," *Acta Metallurgica*, vol. 30, no. 10, pp. 1883–1890, 1982.

[12] H. Atkinson and S. Davies, "Fundamental aspects of hot isostatic pressing: An overview," *Metallurgical and Materials Transactions A*, vol. 31A, 2000.

[13] H. . Glsoy and R. M. German, "Sintered foams from precipitation hardened stainless steel powder," *Powder Metallurgy*, vol. 51, no. 4, pp. 350–353, 2008.

[14] S. Mcdeavitt and A. Solomon, "Hot-isostatic pressing of U-10Zr by grain boundary diffusion and creep cavitation. part 2: Theory and data analysis," Jan 1997.

[15] G. Maier, H. Assmann, and W. Drr, "Resinter testing in relation to in-pile densification," *Journal of Nuclear Materials*, vol. 153, pp. 213–220, 1988.

[16] W. J. A., D. R. Mumm, and A. Mohraz., "Microstructural tunability of co-continuous bijel-derived electrodes to provide high energy and power densities." *J. Mater. Chem. A*, vol. 4, no. 3, pp. 1000–007, 2016.

[17] R. B. Potts, "Some generalized order-disorder transformations," *Mathematical Proceedings of the Cambridge Philosophical Society*, vol. 48, no. 1, pp. 106–109, Jan 1952.

[18] V. Tikare, M. Braginsky, and E. A. Olevsky, "Numerical simulation of solid-state sintering: I, sintering of three particles," *Journal of the American Ceramic Society*, vol. 86, no. 1, pp. 49–53, 2003.

[19] M. Braginsky, V. Tikare, and E. Olevsky, "Numerical simulation of solid state sintering," *International Journal of Solids and Structures*, vol. 42, no. 2, pp. 621–636, 2005.

[20] M. P. Fix G.J., Ed. A. Fasano, *Free Boundary Problems: Thoey and Applications*. Pitman, 1983.

[21] L. J.S., "Models of pattern formation in first-order phase transitions," pp. 165–186.

[22] J. W. Cahn and J. E. Hilliard, "Free energy of a nonuniform system. i. interfacial free energy," *The Journal of Chemical Physics*, vol. 28, no. 2, pp. 258–267, 1958.

[23] L.-Q. Chen, "Phase-field models for microstructure evolution," *Annual Review of Materials Research*, vol. 32, no. 1, pp. 113–140, 2002.

[24] Y. U. Wang, "Computer modeling and simulation of solid-state sintering: A phase field approach," *Acta Materialia*, vol. 54, no. 4, pp. 953–961, 2006.

[25] Y. Wang, Y. Liu, C. Ciobanu, and B. R. Patton, "Simulating microstructural evolution and electrical transport in ceramic gas sensors," *Journal of the American Ceramic Society*, vol. 83, no. 9, pp. 2219–2226, 2004.

[26] M. R. Tonks, D. Gaston, P. C. Millett, D. Andrs, and P. Talbot, "An object-oriented finite element framework for multiphysics phase field simulations," *Computational Materials Science*, vol. 51, no. 1, pp. 20–29, 2012.

[27] D. Gaston, C. Newman, G. Hansen, and D. Lebrun-Grandi, "Moose: A parallel computational framework for coupled systems of nonlinear equations," *Nuclear Engineering and Design*, vol. 239, no. 10, pp. 1768–1778, 2009.

[28] A. Jokisaari, P. Voorhees, J. Guyer, J. Warren, , and O. Heinonen, "Benchmark problems for numerical implementations of phase field models," *Computational Materials Science*, vol. 126, pp. 139–151, 2017.

[29] X.-M. Bai, M. R. Tonks, Y. Zhang, , and J. D. Hales, "Multiscale modeling of thermal conductivity of high burnup structures in UO2 fuels," *Journal of Nuclear Materials*, vol. 470, pp. 208–215, 2016.

[30] Cenna, "Phase field order parameter."

[31] Chronholm144, 2006.

[32] "Moose framework," http://mooseframework.org/.

[33] D. Schwen, "Moose workshop: Moose-pf/marmot training," Nashville,TN, 2015.

[34] Ahrens, James, Geveci, Berk, Law, and Charles, "Paraview: An end-user tool for large data visualization, visualization handbook," pp. 1000–007, 2005.

[35] K. Asp and J. gren, "Phase-field simulation of sintering and related phenomena a vacancy diffusion approach," *Acta Materialia*, vol. 54, no. 5, pp. 1241–1248, 2006.

[36] R. L. Coble, "Sintering crystalline solids. i. intermediate and final state diffusion models," *Sintering Key Papers*, pp. 55–67, 1990.

[37] R. M. German, "Prediction of sintered density for bimodal powder mixtures," *Metallurgical Transactions A*, vol. 23, no. 5, pp. 1455–1465, 1992.

[38] G. L. Messing and G. Y. Onoda, "Sintering of inhomogeneous binary powder mixtures," *Journal of the American Ceramic Society*, vol. 64, no. 8, pp. 468–472, 1981.

[39] E. A. Olevsky, "Theory of sintering: from discrete to continuum," *Materials Science and Engineering: R: Reports*, vol. 23, no. 2, pp. 41–100, 1998.

[40] J. Pan, H. Le, S. Kucherenko, and J. Yeomans, "A model for the sintering of spherical particles of different sizes by solid state diffusion," *Acta Materialia*, vol. 46, no. 13, pp. 4671–4690, 1998.

[41] F. Wakai, M. Yoshida, Y. Shinoda, and T. Akatsu, "Coarsening and grain growth in sintering of two particles of different sizes," *Acta Materialia*, vol. 53, no. 5, pp. 1361–1371, 2005.

[42] O. Tange, "Gnu parallel - the command-line power tool," *;login: The USENIX Magazine*, vol. 36, no. 1, pp. 42–47, Feb 2011. [Online]. Available: http://www.gnu.org/s/parallel

[43] D. C. Crawford, D. L. Porter, and S. L. Hayes, "Fuels for sodium-cooled fast reactors: Us perspective," *Journal of Nuclear Materials*, vol. 371, no. 1-3, pp. 202–231, 2007.

[44] A. Moore, C. Deo, M. Baskes, and M. Okuniewski, "Atomistic mechanisms of morphological evolution and segregation in U-Zr alloys," *Acta Materialia*, vol. 115, pp. 178–188, 2016.

[45] G.-Y. Huang and B. D. Wirth, "First-principles study of bubble nucleation and growth behaviors in α U-Zr," *Journal of Physics: Condensed Matter*, vol. 24, no. 41, pp. 415–404, 2012.

[46] J. Rest, "An analytical study of gas-bubble nucleation mechanisms in uranium-alloy nuclear fuel at high temperature," *Journal of Nuclear Materials*, vol. 402, no. 2-3, pp. 179–185, 2010.

[47] S. Ahn, S. Irukuvarghula, and S. M. Mcdeavitt, "Thermophysical investigations of the uranium–zirconium alloy system," *Journal of Alloys and Compounds*, vol. 611, pp. 355–362, 2014.

[48] A. Sangjoon, I. Sandeep, and M. S. M., "Microstructure of α-u and δ-uzr2 phase uraniumzirconium alloys irradiated with 140-kev He ion-beam," *Journal of Alloys and Compounds*, vol. 681, pp. 6–11, 2016.

[49] D. B. Lancaster, R. L. Marsh, D. B. Bullen, P. Holger, S. C. Erwin, and A. E. Levin, "A technique for the selection of the fuel pin diameter for a uranium/zirconium alloy-fueled pressurized water reactor," *Nuclear technology*, vol. 97, 1992.

[50] E. S. Fisher, "The first 30 years of research on the physical properties of α-U," *Journal of Alloys and Compounds*, vol. 213-214, pp. 254–261, 1994.

[51] W. J. V. Sames, "Uranium metal powder production , particle distribution analysis , and reaction rate studies of a hydride - dehydride process." Texas A&M University.

Appendix C

Determination of Vacancy Formation Energies in U-Zr Alloys

PI: Chaitanya Deo

Personnel:

David Carroll (Graduate Student)

Elton Chen (Graduate Student)

Daniel Vizoso (Graduation Student)

Submitted to: University of Arkansas

Final Report of Subcontract

2506P44

RF347

COMPUTATIONAL A0ND EXPERIMENTAL STUDIES OF MICROSTRUCTURE-SCALE POROSITY

TABLE OF CONTENTS

LIST OF TABLES

LIST OF FIGURES

Page

Page

As new nuclear reactors are being considered, such as fast reactors and advanced thermal reactors, new designs for key components are being considered. In America's current reactor fleet, uranium oxides are often used as they have a much higher melting point than other potential fuels, and are also inflammable, since the fuel is already in an oxidized state. However, for fast reactors, several different fuel types are being considered, chief among them being metallic alloys.

Metallic alloys were used in early experimental nuclear reactors due to their high fissile density, compatability with the sodium coolant, and low smear density which lead to a much higher fuel burnup. Many of the first reactors used in the nuclear program's infancy utilized metallic fuels; in the U.S., the EBR-I, EBR-II, and FERMI-I used metallic alloys, as well as the DFR in the U.K. Specifically, the Integral Fast Reactor in the U.S. used U-Pu-Zr alloys and was the first program to put together a vast database on the metallic alloy fuel's performance. Mark-I, or first generation, fuel used unalloyed, highly enriched uranium metal. In EBR-I, Mk-II fuels were composed of centrifugally cast U-Zr alloy, while Mk-III fuels coextruded Mk-II fuels with a layer of Zircaloy-2 cladding. After the EBR-I, the EBR-II irradiated over 30,000 Mk-II fuel driver rods, 13,000 Mk-III/IIIA/IV driver fuel rods, and over 600 U-Pu-Zr fuel rods. So the U-Zr alloy has long been important in nuclear fuel development and will continue to be important as advanced reactors are developed, as thermal reactors with oxide fuels have only been used in the past.

Metallic Fuel Advantages

Metallic alloy fuels are being looked at as primary fuels in advanced reactor designs currently being developed due to several traits that would help them perform better than the oxide fuels being used in the nuclear industry's current fleet of reactors. First, metallic fuels can

have a higher burn-up potential due to their ability to possibly have a higher fissile atom density. Since there is more burn-up potential in the fuel, the operation time between refueling will be longer, allows smaller reactor designs with high power density, and allows more plutonium to be bred during operation time.

Advanced reactors, especially fast neutron reactors, will be operating at much higher temperatures than thermal reactors currently being operated. Metallic fuels have the thermodynamic properties required to better handle the higher temperatures, specifically a better thermal conductivity, allowing much more efficient cooling and reducing cladding and fuel temperatures.

Most of the metallic fuels will be in the BCC phase during reactor operating temperatures, leading to much more isotropic neutron cross sections. This is particularly beneficial for smaller reactors as it also allows a higher power density.

Another metallic fuel advantage is that plutonium does not have to be separated from the fuel during reprocessing. Plutonium has a very high potential to be used in nuclear devices, so proliferation experts would prefer a fuel that can be reprocessed without separating out the plutonium.

The last advantage worth mentioning is that metallic fuels have some passive safety features during core off-normal events that oxide fuels clearly do not. During a loss-of-flow event, fission gases and thermal expansion will cause the fuel to expand and swell to the cladding, where the fuel at the interface will transform to the molten phase, reducing reactivity in the reactor and helping to prevent the core from going supercritical.

Metallic Fuel Disadvantages

However, as with any engineering solution, there are downsides to go with the upsides. Fuel swelling, fission gas release, fuel redistribution, and cladding and coolant interactions are all potential problems that need to be addressed before utilizing the metallic fuels in commercial reactors.

Fuel swelling is when the fuel's volume increases while its general shape remains the same, where as irradiation growth causes the fuel's shape to change while the volume remains the same. Both of these occur as the fuel is irradiated during reactor operation. When operation first begins, the metallic fuel swells drastically due to fission gas bubbles; once these bubbles become interconnected and create a pathway for them to escape through, the swelling slows and is mostly caused by fission products taking spots in the fuel's lattice. These fission products also bring about a decrease in thermal conductivity, as the fission products tend to have a lower thermal conductivity than the metals they are replacing. In addition, large irregular shaped cavities are caused by grain boundary tearing at the fuel edges. Both irradiation growth and grain boundary tearing can cause reactivity loss in the reactor (Pahl 1990).

The fuel cladding mechanical interaction (FCMI) is another downside that occurs as the fuel is irradiated. The fission gas pressure can cause irradiation/thermal creep until eventually the cladding undergoes a stress-rupture (Pahl 1990; Pahl 1992). Until the 1960's, when a technical breakthrough at Argonne National Lab changed things, the FCMI put a limit on the burn-up of metallic fuels. With the newly decreased FCMI, the burn-up potential of metallic fuels was finally achieved (Ogata 1996; Walters 1984). By reducing the smear density by approximately 75%, the fuel has room to swell inside the cladding, so the fission gas will connect enough to create an escape path before the stress-rupture occurs.

There is also the fuel cladding chemical interaction (FCCI), which can cause creep rupture at high burn-ups. Another result of FCCI is fuel elements such as plutonium, uranium, and fission products can diffuse into the cladding, leading to cladding wall thinning, a brittle cladding layer, and a lowered melting point due to a eutectic composition in the fuel (Pahl 1990; Hayes 2009; Ogata 1997).

Experiments have also shown that uranium and zirconium undergo redistribution when the uranium-zirconium alloys undergo irradiation, as in a nuclear reactor. However, experimentally, this interdiffusional restructuring only slightly changes the mechanical and neutronic properties of the fuel, and makes no significant change to the overall fuel lifetime, despite a lowered solidus temperature in some fuel regions (Pahl 1990; Kim 2004).

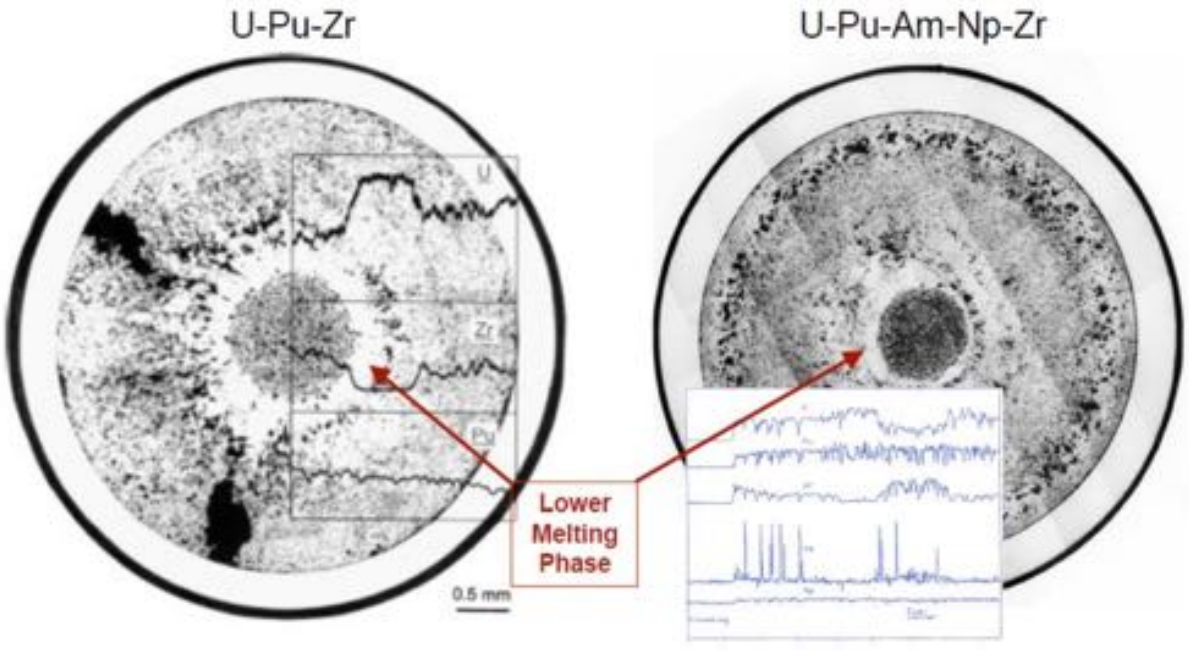

Figure 1: Post-irradiation Optical Metallography and Measured Constituent Redistributions (Kim 2004; Hofman 1996)

Another potential downside is the lower melting point of metallic alloy fuels compared to oxide fuels. Uranium in particular has a low melting point, however, by alloying to metals that

are also in BCC phase at high temperatures. So far, zirconium, molybdenum, and niobium are the alloying metals that have been studied most. One of the positives of nuclear metallic fuel, the alloy's higher thermal conductivity, could negate this negative to some degree. Since the thermal conductivity is higher, the thermal flux will be higher, allowing a lower temperature gradient and high power density while still remaining below the fuel's melting point. In addition, the lower melting point is not necessarily a total negative. In the event of a loss of cooling, the low melting point will allow the fuel to go into the molten phase earlier, reducing reactor reactivity. This is a passive safety feature of the metallic fuel.

Swelling has also been considered a potential benefit, in certain off-normal situations. The interconnected porosity of swollen metallic fuel and the low melting point during a transient event allows for the fuel's thermal expansion during temperature-induced phase transitions. This transformation prevents the cladding from being stressed by the fuel and allows the fuel to flow onto itself in the open porosity (Ondracek 1973).

There is still a lot that needs to be discovered about metallic fuels before implementation in advanced reactor designs and a lot of that information will be discovered using computational simulations. Unfortunately, a lot of the necessary tools for computational simulation of metallic fuels are not complete. Computational simulation gives the ability to see what is happening at much smaller sizes and timescales than is possible using experimentation and will also allow predictions to be made about metallic fuel properties under a variety of conditions that are not necessarily possible to make experimentally. Experimentation at higher temperatures is also difficult due to severe thermal scatter. By using experimentation and computational simulation together, it will be possible to plan the operation and design of a reactor, as well as optimizing fabrication and processing of fuels.

Uranium (U)

Uranium is an actinide exhibiting delocalized f-electrons, and therefore has three solid allotropes: α (face-centered orthorhombic), β (body-centered tetragonal), and γ (body-centered cubic). The α state is uranium's base level allotrope but transforms into the β around 935 K, while β becomes γ at approximately 1045 K. The γ allotrope is the most interesting for advanced reactor designs as most advanced reactors operate at very high temperatures. The α, β, and γ crystal structures are shown below.

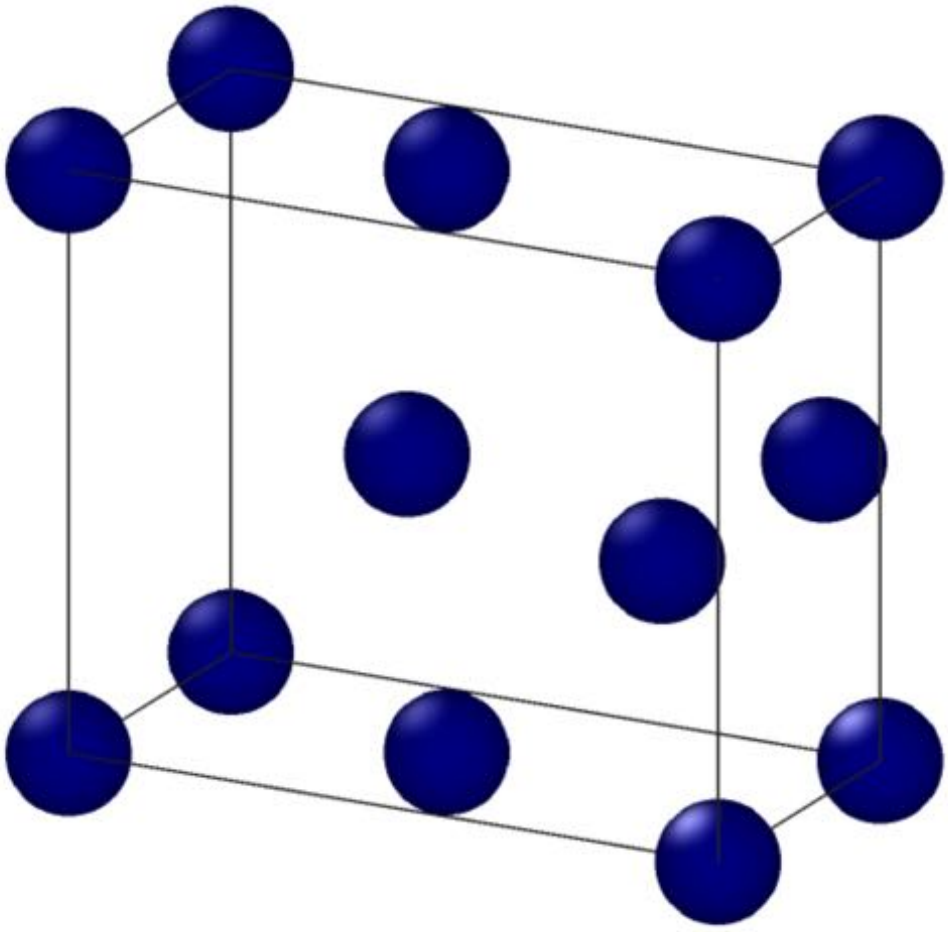

Figure 2: The Unit Cell of the α-U Crystal Structure

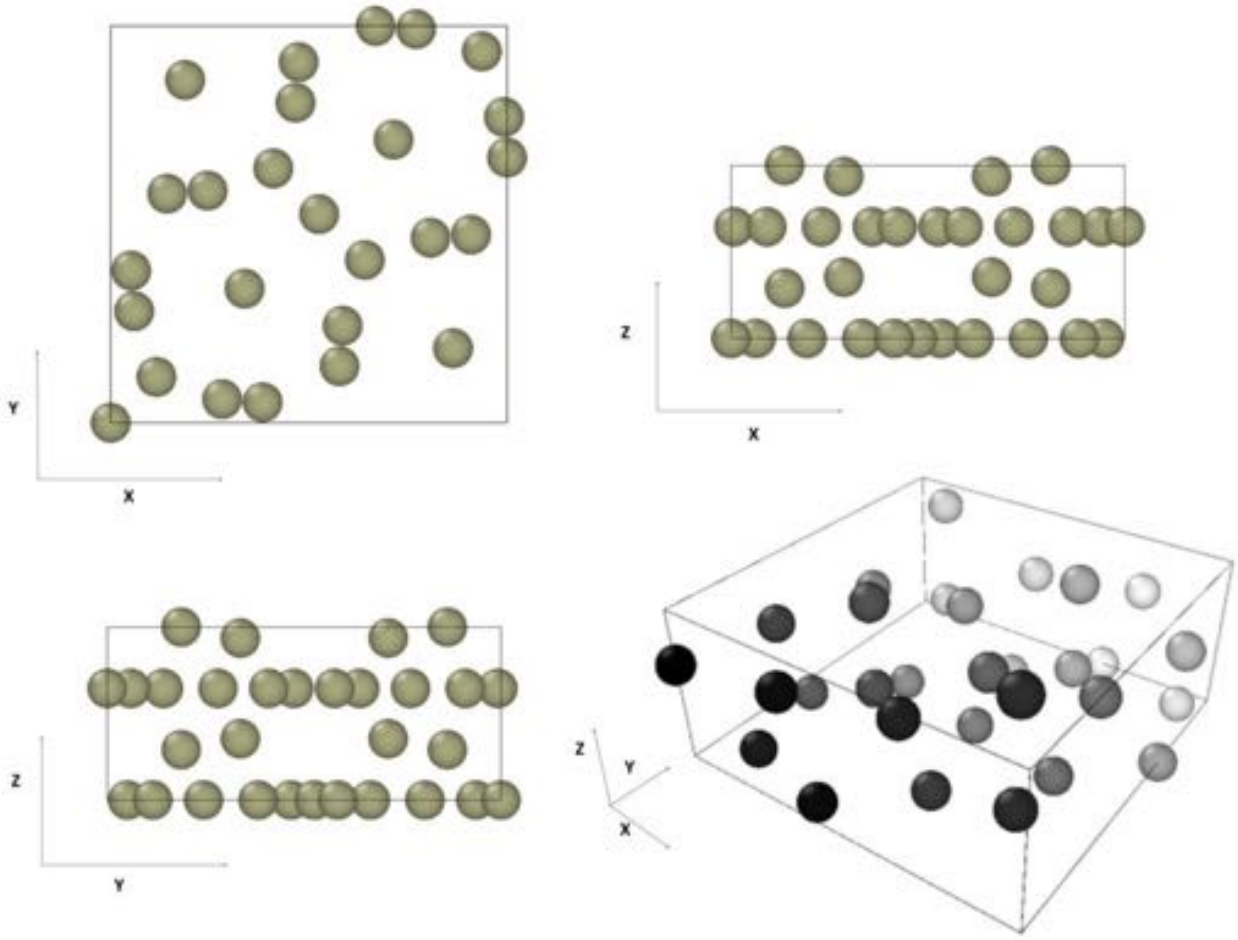

Figure 3: The β-U Crystal Structure (Beeler 2012a)

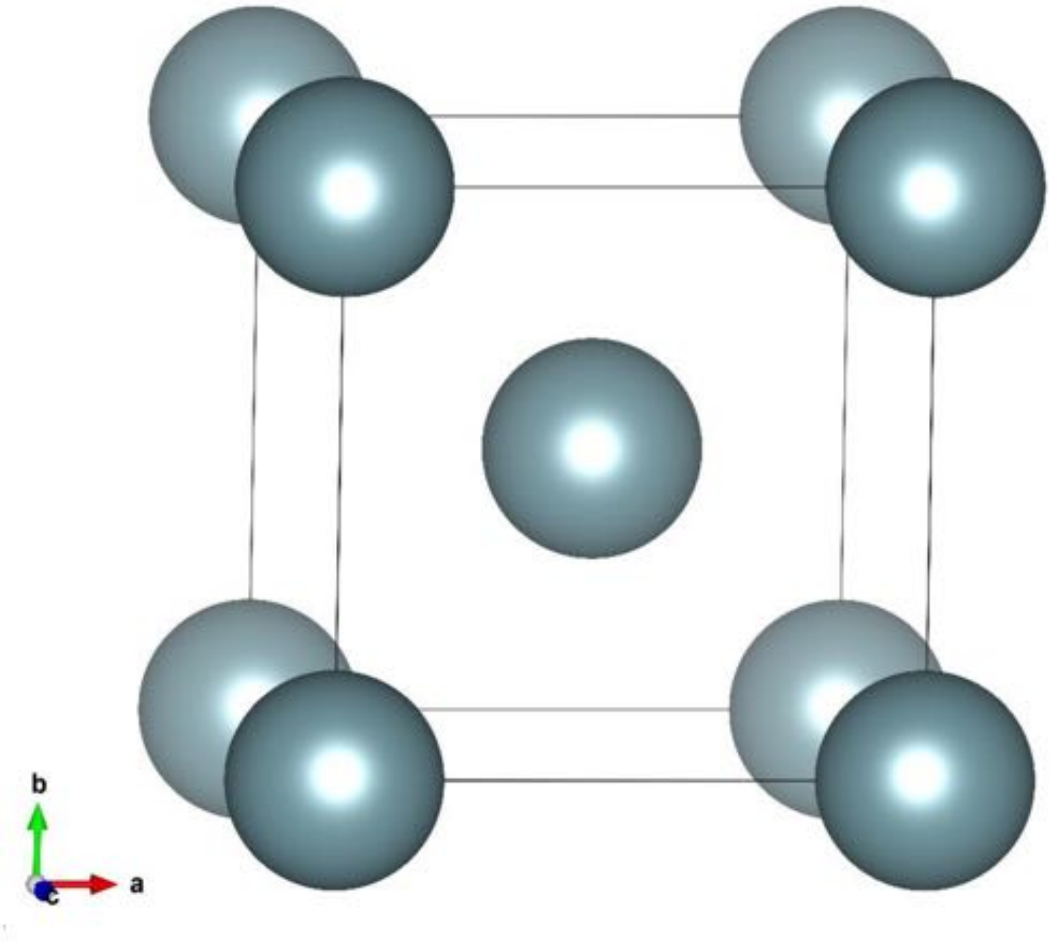

Figure 4: The γ-U Crystal Structure

Uranium's vacancy formation energies in the BCC state have been calculated in several previous studies, as shown in Table 1 below. Since then, a previous study done by Moore has found a vacancy formation energy of 1.34 eV for the uranium at 0 K.

Table 1: Vacancy Formation Energies of γ-U

E^{v}_{form} (PBE)	1.384 eV
E^{v}_{form} (PW91)	1.323 eV
E^{v}_{form} (Xiang) [14]	1.08 eV
E^{v}_{form} (Matter) [15]	1.2 ± 0.25 eV

Zirconium (Zr)

Zirconium is a transition metal and has two solid phases. At low temperatures, it is in the α (hexagonally closed packed) phase, while starting at 863° C, it transitions to the β (body centered cubic) phase. Zirconium also has a very high melting point of 1855° C, or 2128 K. Because of the fact that both uranium and zirconium are in the bcc phase at high temperatures, zirconium is a strong candidate for alloying with uranium. In addition, the high melting point raises the melting point of uranium once the two are alloyed. In the same study done by Moore cited above, the vacancy formation energy of β zirconium was found to be 2.1 eV.

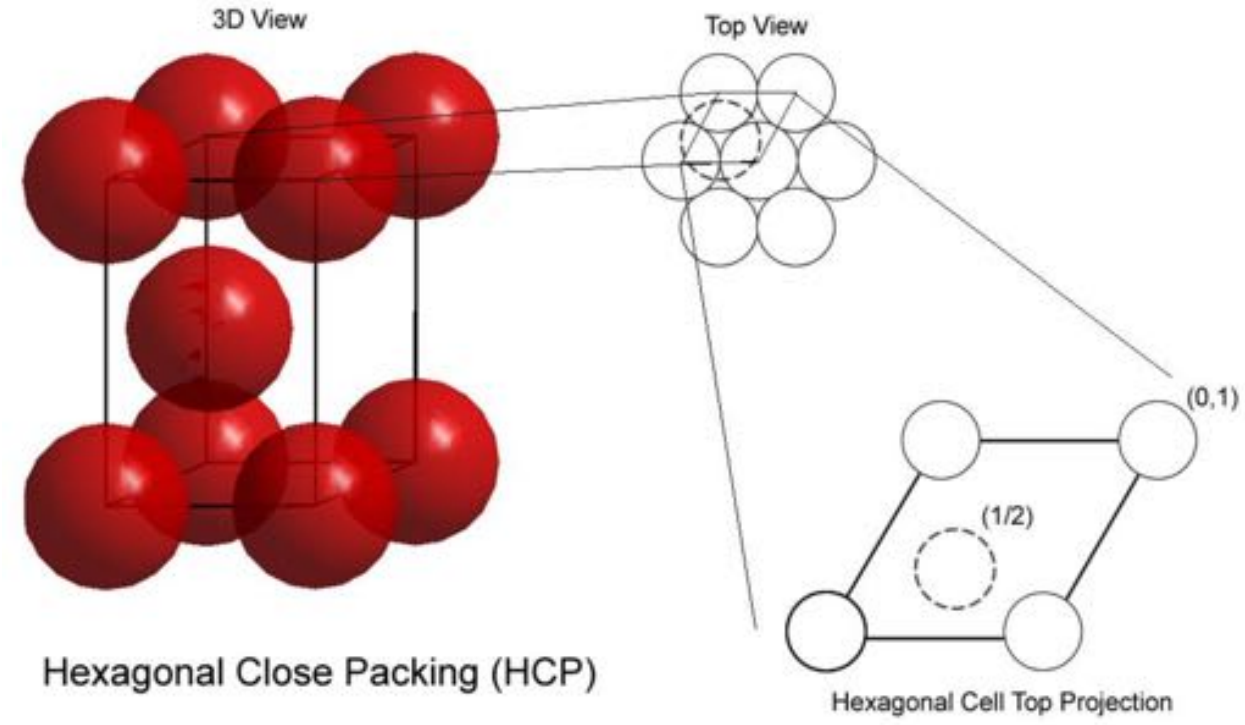

Figure 5: Unit Cell of α-Zr Crystal Structure ("Hexagonal Closed Packing HCP")

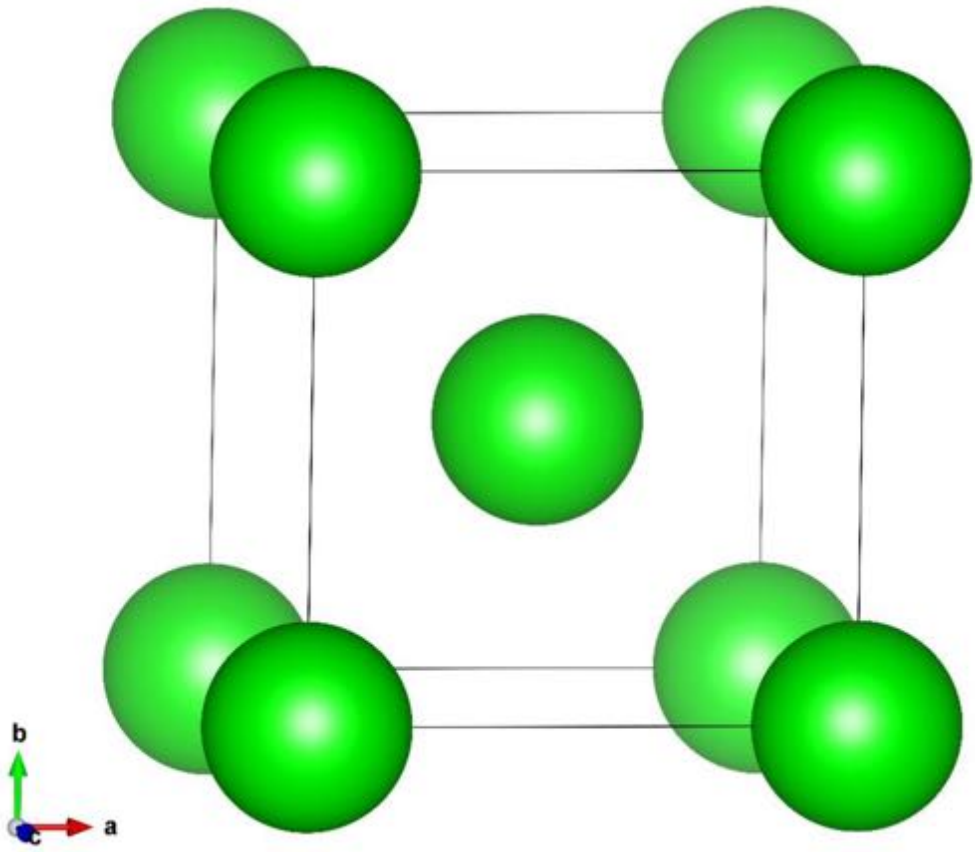

Figure 6: The β-Zr Crystal Structure

Uranium-Zirconium Alloy

Zirconium has long been used in nuclear reactors as cladding and for other components due to multiple properties; it has a high temperature BCC phase, high melting point, very small neutron absorption cross-section, low cost, and high fission product yield. The reasons that make it a good material for reactor components are the same reasons it should make a good material to be alloyed with uranium for metallic alloy fuel. In the past, which metal to alloy with uranium has been decided by trial and error, compromising between corrosion resistance and mechanical properties. In addition to several other candidates, such as molybdenum and niobium, uranium-zirconium has been selected as a great option for nuclear fuel in fast reacotrs.

At reactor operating temperatures, both uranium and zirconium are in the body centered cubic phase, so all uranium-zirconium alloys, no matter the composition, will be in body centered cubic as well. It should be noted that from 65% to 75% zirconium, the alloy goes through a δ (C32 crystal structure) before transitioning to the predicted γ phase at 890 K. However, this research focuses on alloys up to 30% zirconium. H. Okamoto has created the most recent uranium-zirconium diagram utilizing a compilation of experimental papers, as shown below.

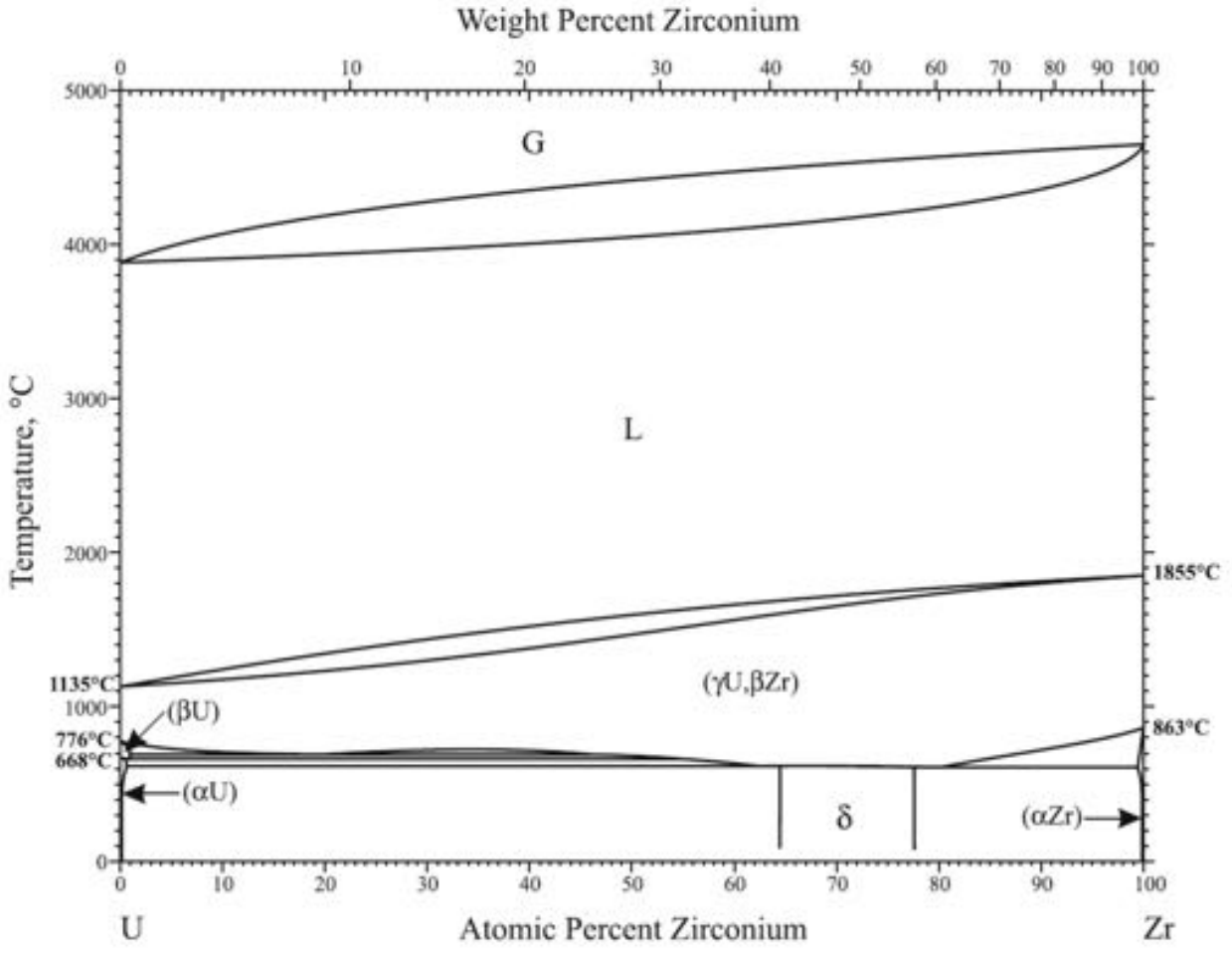

Figure 7: Phase Diagram of U-Zr (Okamoto 2007)

Due to sharing a BCC structure, γU and βZr are completely miscible and the alloy of the two have isotropic neutronics, which is why it is the main phase of interest for high temperature fast reactors. The BCC phase also has the desired isotropic expansion for use in the TRIGA type pool reactors and the Generation IV SFR's reactors (EBR-II, SABR, S-PRISM, etc.), but there is not as much experimental data about the lower temperature phases. The primary focus of this research is the BCC metallic phase.

Applications of Uranium-Zirconium

Subcritical Advanced Burner Reactor (SABR)

One of the advanced reactor designs that will be made possible through use of metallic alloy fuels is the Subcritical Advanced Burner Reactor (SABR). In this design, a subcritical fission reactor is driven by a fusion neutron source, similar to a tokamak design. This design has several advantages, such as using not highly enriched fuel and better safety since the design is inherently subcritical (Stacey, unpublished data).

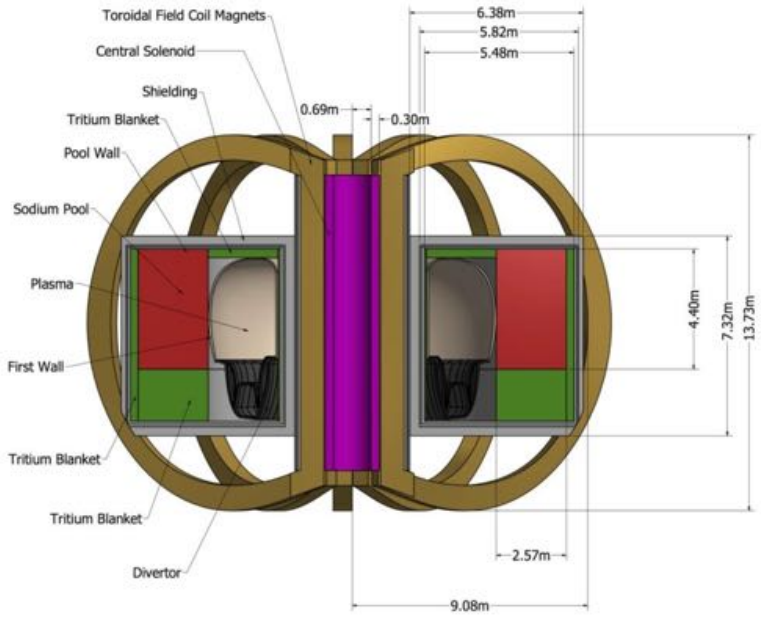

Figure 8: Perspective View of SABR Configuration (Stacey, unpublished data)

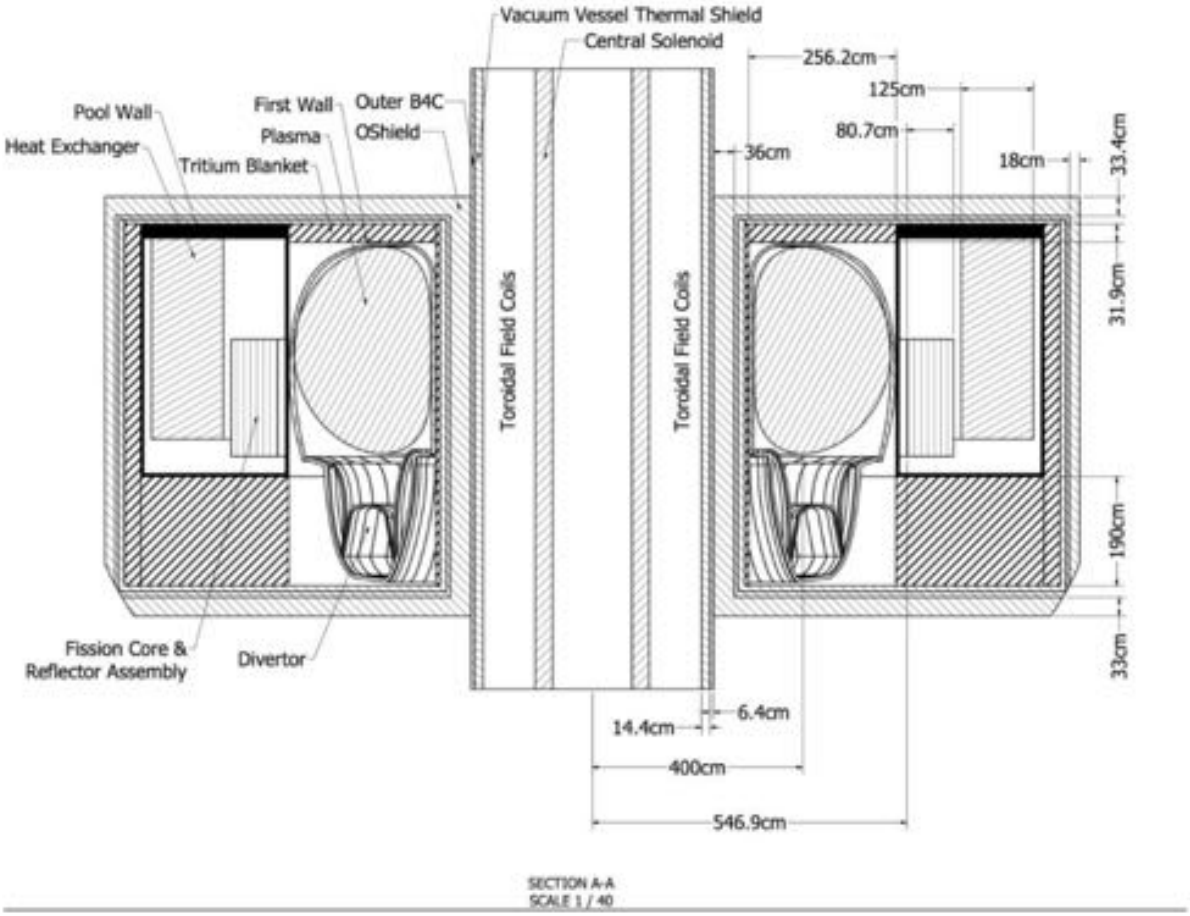

Figure 9: Radial View of SABR Configuration (Stacey, unpublished data)

Table 2: Basic SABR Core Properties (Stacey, unpublished data)

Fast Reactor Core Properties	
Coolant	Sodium (Na)
TRU fuel composition	40Zr-10Am-10Np-40Pu
Fuel Maximum / Allowable Temperature	1014 K / 1200 K
Cladding Maximum / Allowable Temperature	814 K / 923 K
Coolant Maximum / Allowable Temperature	787 K / 1156 K
BOL TRU mass	15104 kg
BOL keff	0.973
Specific power	198.6 W/gHM
Fuel assembly	800
Fuel pin	469/per assembly, 375,200 total

Table 2 Continued: Basic SABR Core Properties (Stacey, unpublished data)

Power density	256 kW/L
Linear fuel pin power	12.3 kW/m
Sodium coolant mass flow rate	16,690 kg/s
Coolant temperature Tincool/Toutcool	628 K/769 K
Fuel & Clad temperature Tmaxfuel/Tmaxclad	1014 K/ 814 K
Clad & Structure	ODS MA957
Electric insulator	SiC
Fuel/Clad/Bond/Insulator/duct/coolant/wire (v/o)	22.3/17.6/7.4/6.5/9.3/35.3/1.5%

However, this design did come with a few problems. SABR is designed for long fuel irradiation cycles with high burn-up, so the metallic alloy fuel would undergo a large amount of swelling and a significant fission gas production. In order to combat this, the fuel is fabricated with a 75% smear density and an extra-long plenum was created to hold the fission gases that escape the fuel. Swelling and fission gas is already an issue with metallic fuels, but with SABR's higher burn-up conditions, the plenum is twice as long as the fuel region, allowing the extra fission gas to escape.

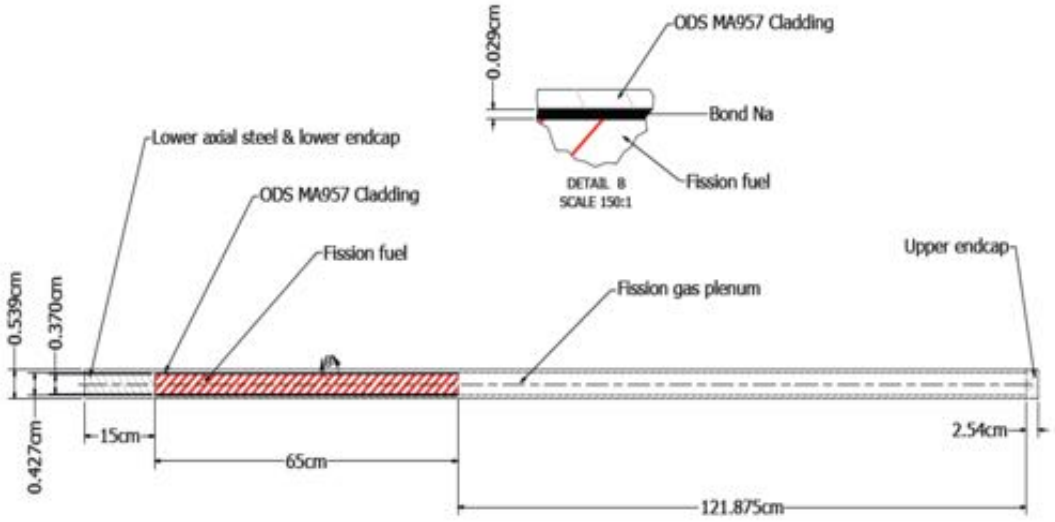

Figure 10: SABR Fuel Pin Configuration (Stacey, unpublished data)

As previously discussed in the Metallic Fuel Disadvantages section, the cladding is also going to be subject to irradiation damage and fuel cladding interactions (FMMI and FCMI). So far, the SABR design keeps the cladding irradiation damage below the set limit; however, incorporating fuel cladding interactions may require more research to keep it below safety limits.

Methods

Computational Simulations

By modeling materials using computer simulations, it is possible to get a much closer look at the properties of the materials than just through experimentation. Using computational methods, one can see the effect removing or adding one single atom to the lattice structure has, or at what precise moment a material changes phase. Without thorough information on the microstructural properties only obtainable through computational methods, it is much more difficult to predict how the macroscopic properties will react under varying circumstances.

Ensembles are composed of a group of atoms, represented by a sequence of points, that satisfy the conditions of a particular thermodynamic state. An ensemble can have atoms with many different microscopic states, but are unified by one or more macroscopic or thermodynamic property.

Ensembles are named after the properties that are fixed, or the independent variable. Not only would not holding any of the variables constant be computationally expensive, but it would be difficult to interpret the data and which changing property is affecting the thermodynamic properties of the whole structure. Ensembles are in computational simulations in order to find the approximate equilibrium state of the dependent variables.

In order to calculate the equilibrium values of the dependent variables, it is assumed that once the simulation has undergone enough steps, the dependent variables will be fluctuating around the equilibrium value, so the average of the value is taken once the dependent value has started fluctuating until the end of the simulation. The equation is shown below

$$\langle A \rangle = \sum_i A_i p_i \qquad (1)$$

It is assumed that the ensemble average is the same as the time average once the variations of the dependent variables has settled to fluctuate around the equilibrium value; this is known as the Ergodic hypothesis for Molecular Dynamics simulations.

$$\langle A \rangle = \lim_{t\to\infty} \frac{1}{t} \int_0^t A \, dt \qquad (2)$$

Table 3: Common Thermodynamic Ensembles

Ensembles	Independent Variables	Dependent Variables	Z (Partition Function)	Pi (ith state Probability)
Microcanonical	N, V, U	μ, P, T	$\sum_i \delta(E_i - E)$	$\frac{\delta(E_i - E)}{Z_{NVE}}$
Canonical	N, V, T	μ, P, E	$\sum_i e^{-\beta E_i(N,V)}$	$\frac{e^{-\beta E_i(N,V)}}{Z_{NVT}}$
Grand Canonical	V, T, μ	N, P, L	$\sum_i e^{\beta N \mu} Z_{NVT}$	$\frac{e^{-\beta(E_i - \mu N)}}{Z_{NV\mu}}$
Isothermal-Isobaric	N, P, T	μ, V, H	$\sum_i e^{\beta p V_i} Z_{NVT}$	$\frac{e^{-\beta(E - pV_i)}}{Z_{NPT}}$

The total energy of the system is U, $\beta=1/k_BT$ is the reduced temperature, Z is the partition function, N is the number of moles, V is volume, T is temperature, μ is the chemical potential, P is the pressure, H=U+PV is the enthalpy, $L=U - \Sigma(\mu_i N_i)$ is the Hill energy, P_i represents the probability of observing the ith state, and all of the other subscript i's represent the parameter at the ith state (Hünenberger 2005).

Molecular Dynamics

Molecular Dynamics computational methods utilizes an interatomic potential in order to properly simulate how the atoms in a structure interact with each other. In this case specifically, the Modified Embedded-Atom Method (MEAM) was used, but more on that later. Molecular

Dynamics uses the gradient vector of the potential energy at each atom's location to determine the force acting upon that atom. This force is specifically calculated using the MEAM interatomic potential. In Molecular Dynamics, each atom is allowed to move for a short period of time based on the forces being applied to it by the other atoms, as calculated by the MEAM interatomic potential. Molecular Dynamics then gives snapshots of the structure over time as the atoms are allowed to move around until they have come to an equilibrium state. The temperature of the simulation is calculated based on the average velocity of all of the atoms.

The Large-scale Atomic/Molecular Massively Parallel Simulator (LAMMPS) was the Molecular Dynamics code used in this research. The initial setup consisted of 2000 atoms with periodic boundary conditions in an unrelaxed, perfect BCC lattice. The atoms were then allowed to relax by running in an isothermal-isobaric (NPT) ensemble, where the number of atoms, pressure, and temperature are held constant. Then, the center atom is removed and the remaining 1999 atoms are run in a canonical (NVT) ensemble, where the number of atoms, volume, and temperature remained constant.

Modified Embedded-Atom Method Interatomic Potential

Interatomic potentials are of vital importance to simulations that model material properties. The foundation of these potentials is Density Functional Theory (DFT), which posits that energy is a functional of the electron density. With knowledge of the electron density of an entire system, one can determine the potential energy of a system:

$$U = f[\rho(r)] \tag{3}$$

$$E[\rho(r)] = T_s[\rho(r)] + J[\rho(r)] + E_{xc}[\rho(r)] + E_{ext}[\rho(r)] + E_{ii}[\rho(r)] \tag{4}$$

where E is the total energy, T_s is the single particle kinetic energy, J is the Hartree Electron-Electron Energy, E_{xc} is the Exchange Correlation Functional, E_{ext} is the Electron-Ion Coulombic Interaction, and E_{ii} is the Ion-Ion Energy (Moore 2013).

With this basis, the Embedded-Atom Method (EAM) was created by assuming that an atom can be embedded into a homogeneous electron gas, and the change in potential energy is a functional of the embedded atom electron density that can be approximated with an embedding function. In a crystal, though, the electron density is not homogeneous, so the EAM potential replaces the background electron density with the electron densities for each atom and supplements the embedding energy with a repulsive pair potential to represent atoms core-core interactions.

With a simple linear superposition of the atoms' electron densities as the background electron density, the EAM is governed by the following equations:

$$R_{ij} = \left|r_i - r_j\right| \tag{5}$$

$$\overline{\rho_i} = \sum_j \rho_j^a\left(R_{ij}\right) \tag{6}$$

$$U = \sum_i F(\overline{\rho_i}) + \frac{1}{2}\sum_{i,j} \phi\left(R_{ij}\right) \tag{7}$$

where R_{ij} is the distance between atoms i and j, ρ_j^a is the atomic electron density, r_i is the position of atom i, F is the embedding function, ρ_i are the electron densities, and ϕ is the pair interaction potential.

However, EAM does not do a great job of simulating materials with significant directional bonding, which includes most metals. In order to properly simulate metals, the Modified Embedded-Atom Method was created, which allows the background electron density to depend on the local environment instead of assuming a linear superposition. The equation governing the potential energy is

$$U = \sum_i F(\overline{\rho_i}) + \frac{1}{2}\sum_{i,j\neq i} \phi_{ij}(R_{ij})S(R_{ij}) \qquad (8)$$

The main difference between the equation for potential energy for the EAM and MEAM is the inclusion of S, which is the radial screening.

For a more in-depth look at the MEAM interatomic potential used in this work, Moore's 2013 thesis and 2016 dissertation is recommended as further reading, where Moore developed the interatomic potential for uranium and zirconium.

MD Time Converging and Averaging

As previously discussed, the simulation must first be run long enough for dependent variables of the ensemble to settle from the initialized position. Once that has happened, they also must be run long enough to give a statistically sound average. For both before and after the center atom of the lattice structure is removed, the simulation is run for 20 picoseconds with a timestep of 1 femtosecond, which gives 20,000 steps for each stage, and 40,000 steps total. The ensemble average of the properties was calculated during the last 10 picoseconds of each stage.

Periodic Boundary Conditions and Finite Size Effects

In order to allow a small lattice structure of 2000 atoms to properly represent a full sized structure, a periodic boundary condition is used so that if an atom leaves on end of the cell, it returns on the opposite side, as if a new atom came in to take its place. This ensures that the lattice always has the proper amount of atoms while also simulating a much larger structure.

Even with the periodic boundary conditions, the system must be large enough to accurately represent the effects of all of the atoms that are close enough to apply a force to the atom that is removed for the vacancy. However, the larger the computational system, the even longer the computational time becomes, leading to need to find a "sweet spot" between reducing both periodic boundary finite size effects and computational runtime.

Finite periodic box size effects can be hard to quantify, especially due to thermal scattering events dominating the finite periodic box effects. A larger box size also leads to better time averages thanks to the law of large numbers. The box size also needs to be large enough to allow separation, clustering, and ordering effects to be seen without neighboring reflected images interfering.

A 10x10x10 BCC unit cells cubic periodic box was chosen based upon previous research which analyzed the potential energy from a random solid solution molecular dynamics simulation over a range of sizes to find a proper size to keep the periodic boundary finite size effects to a minimum (Moore 2013). The 10x10x10 unit cells form a supercell. It is recommended that the size of the structure is larger than twice the cutoff distance to reduce PBC, and 10x10x10 is much larger. This condition is set because it makes it impossible for a particle to be under the effect of two images of a different, given particle.

Alloying

Several different atomic percentage alloys are used throughout here; 0%, 10%, 20%, and 30% zirconium alloys. In real life, alloys are never exactly the correct atomic percentage. In order to properly simulate this, atoms were changed at random. Starting with a pure uranium 10x10x10 BCC structure, each atom was given a chance at becoming zirconium, that chance being the desired atomic percentage of zirconium in the structure. In addition, to ensure that one random seed number doesn't affect the results too far away from the desired atomic percentage, five different structures were created for each desired atomic percentage, allowing for actual atomic percentages above and below the desired one.

Vacancy Formation Energy

In order to calculate a vacancy formation energy, a single vacancy was introduced into a perfect lattice with equilibrium lattice constants and structural relaxation of atomic positions. Only non-interacting isolated defects were considered when calculating defect formation energy. Visual verification and common neighbor analysis was also used to ensure that the structure of the lattice did not alter phase once the defect had been introduced. With periodic boundary conditions and no point-defect sources, the only other types of defects that could form during the simulation were vacancy-interstitial pairs (Mendelev 2009).

Generally, the formation energy of a vacancy in a homogeneous bulk crystal that does not change phase can be described by:

$$E_v = E_{(n-1)} - \left[\frac{n-1}{n}\right] E_n \qquad (9)$$

$E_{(n-1)}$ is the total energy of an atom supercell containing one vacancy, while E_n is the total energy of that supercell before the vacancy was created.

In this research, the vacancy formation energy was calculated by taking averages in three different ways. In the first way, the total energy from the last 10,000 MD steps of each stage was averaged before plugging into equation 3. Similarly, the variance was calculated for each of the two stages before being used to calculate the overall variance from equation 3 as shown in equation 4:

$$\sigma = \sqrt{\sigma_{(n-1)}^2 + \left[\frac{n-1}{n}\right]^2 \sigma_n^2} \qquad (10)$$

The second method was to calculate the total energy per atom in each of the 10,000 MD steps, as shown in equation 5:

$$E_{atom} = \frac{E}{n} \qquad (11)$$

where n is either 2000 or 1999, depending on whether or not the vacancy had been introduced.

The energy per atom of each step is then averaged and those values were used in equation 3. For the error, the variance of the energy per atom of each step was calculated, and then those values were used in equation 4. The final method had the difference in total energy calculated for each individual step, as shown in equation 6:

$$E_{v,i} = E_{(n-1),i} - \left[\frac{n-1}{n}\right] E_{n,i} \qquad (12)$$

Then, the total vacancy formation energy is calculated:

$$E_v = \sum_{i=1}^{10,000} E_{v,i} \qquad (13)$$

The error is calculated simply by taking the variance of the results from equation 6.

Short Range Order Parameter

Order parameters allow the configuration and order of a structure to be quantified in simple, easy to comprehend values without even looking at the structure itself. The Short Range Order (SRO) parameter uses only the atoms' first nearest neighbors in order to give a single digit to represent the order of the structure:

$$\sigma = -\frac{P_{AA} - n_A}{1 - n_A} \qquad (14)$$

Here, P_{AA} is the fraction of nearest neighbor sites of atom type A that are occupied by A type atoms (averaged over all A type atoms) and n_A is the total atom fraction of A type atoms in the whole system.

So, for the SRO parameter, for a system with an equal number of A and B atom types, a perfectly ordered lattice has a $\sigma = 1$, a phase separated system has a $\sigma = -1$, and a totally random solid solution has a $\sigma = 0$. If the A and B atom types are unequal, σ's extreme values, perfect order and phase separated, are reduced in magnitude.

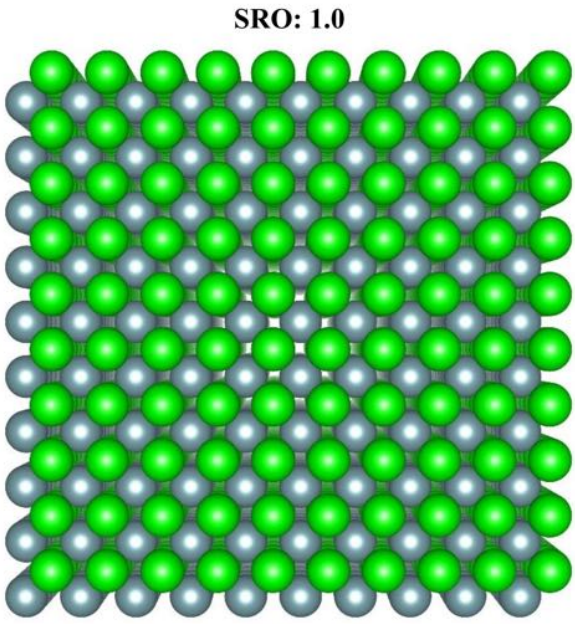

Figure 11: Perfectly Ordered Periodic B2 U-Zr System (Uranium 50% atomic fraction and Zirconium 50% atomic fraction) (Moore 2013)

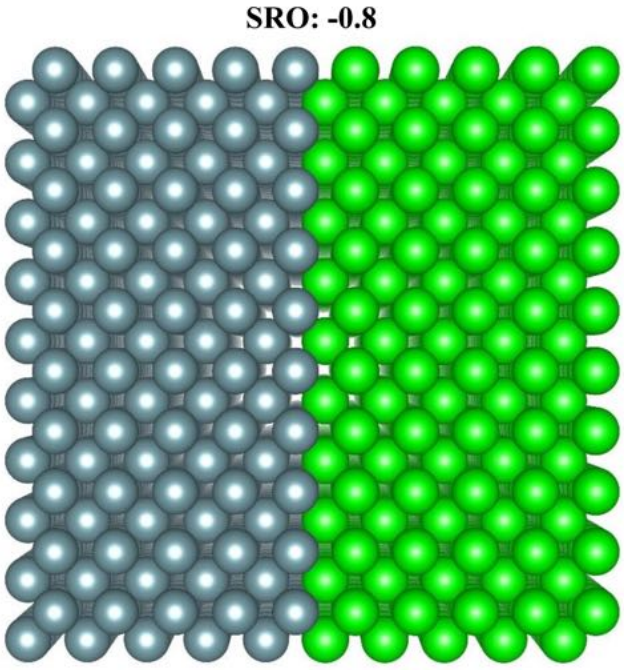

Figure 12: An Example of a Periodically Separated U-Zr System (Uranium 50% atomic fraction and Zirconium 50% atomic fraction) (Moore 2013)

Because this work uses a finite box with periodic boundary conditions, it is impossible to have an SRO of $\sigma = -1$. In this case, the separated SRO parameter depends on the box size and the way the atoms separate; it is possible for the atoms to separate and be divided by a single planar line (see above) or to be clustered into a bunch.

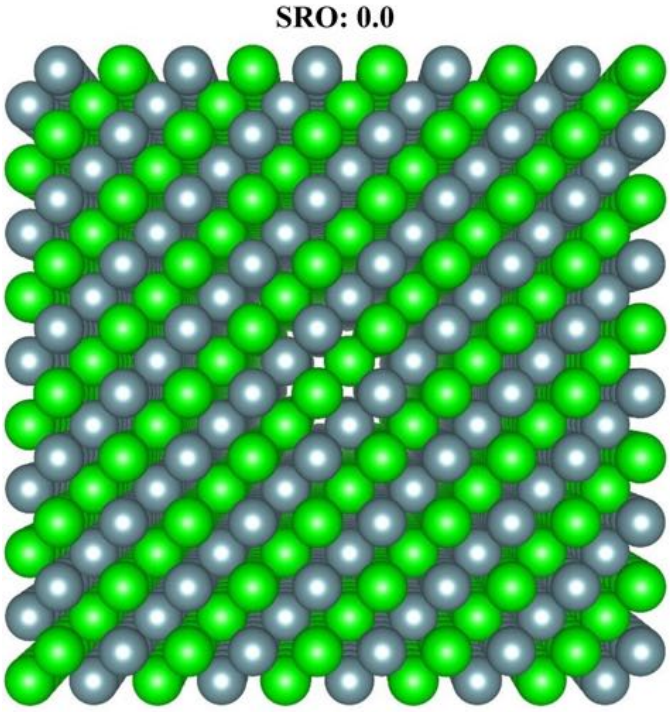

Figure 13: An Example of a Configuration of a Plane of Atoms Not Captured by the Short Range Order Parameter

Because the Short Range Order parameter is a simple quantified representation of a potentially complex order, it is possible that some configurations are not properly represented by the single number. For this reason, visual verification should always be performed in addition to calculating the Short Range Order parameter. For instance, alternating planes of atoms will not be obvious just from the parameter.

The Short Range Order parameter code assumes a Body Centered Cubic crystal structure, which means each atom has eight nearest neighbors. The order parameter is calculated on a snapshot of the atoms' position at any time.

Wigner-Seitz Defect Analysis

Wigner-Seitz defect analysis was used to determine whether or not point defects formed during the simulation run. This defect analysis works by taking a reference state, in this case, the initial, perfect 10x10x10 BCC structure before relaxation occurs, and comparing it to the displaced configuration, the rest of the timesteps occurring during the simulation, both before and after the vacancy was created.

Wherever a particle is located in the refence state is defined as a Wigner-Seitz cell, which is the spatial region belonging to that site. The defect analysis compares the displaced configuration to the reference state; if there are no particles within a Wigner-Seitz cell, that cell contains a vacancy, if there is one particle, then the cell is normal, and if there are more than one particles within the cell, the cell contains an excess interstitial.

Due to the periodic boundary conditions and no point-defect sources, the structure before the vacancy is created will always have the same number of vacancies and interstitials, known as vacancy-interstitial pairs, while once the vacancy has been created, there will always be one more vacancy than interstitials.

Common Neighbor Analysis

In order to determine whether or not the alloys maintain their phase during the simulations, Common Neighbor Analysis was used to verify this. Common Neighbor Analysis, developed by Honeycutt and Andersen, uses an algorithm to develop a "fingerprint" for pairs of

atoms, which characterizes the local structural environment. CNA allows an accurate understanding of which particles are part of which phase, and which are near defects.

Original Common Neighbor Analysis used a cutoff distance to determine whether or not a pair of atoms were bonded, but Stukowski was able to develop an adaptive CNA, which automatically determines cutoff distances for each particle. This allows the parts of the structure which may have slightly changed phase to be determined more readily.

Radial Distribution Function

The radial distribution function gives the density of surrounding particles around each particle and averages them, giving a function that describes, on average, how close particles are to each particle. It is calculated by showing how the atomic density from a reference particle varies as a function of radial distance from the reference particle.

$$g(r) = \frac{1}{4\pi N r^2 \rho_0} \sum_{j=1}^{N} \sum_{\substack{i=1 \\ i \neq j}}^{N} \delta\left(r - r_{ij}\right) \qquad (15)$$

This equation gives the probability of finding a particle in the distance r from a given particle.

A lot of useful information can be pulled from equation 9. By looking at the width of the peaks, one can determine the average thermal scatter, and by examining the distance between the peaks, one can find the phase of the system. It is even possible to determine the chemical ordering of a complex system if elemental radial distance functions are used.

Results

Vacancy Formation Energy

As discussed in the methods section, the vacancy formation energy was calculated using three different methods; the first and third methods used the total energy of the atomic structure, while the second method used the per-atom energy by dividing the total energy by the number of atoms currently in the lattice. As a result, the first and third methods provide incredibly similar results, which are also on the same order of magnitude as previous literature on uranium's vacancy formation energy. Consequently, the first method will be the one used for all subsequent plots. Table 4 gives the results of using all three methods for calculating the vacancy formation energies and standard deviations for all simulation cells run at 800 K. This includes all five cells run at each of zirconium atomic percentages. This demonstrates the similarities of method 1 and 3 and the vastly different method 2.

Table 4: Vacancy Formation Energies for 800 K

	800	Zr00	Zr10	Zr20	Zr30
1	Average 1	1.4003428	1.72230583	2.312345965	-4.178796141
	STD1	2.257896704	2.688173452	2.902574502	3.607615093
	Average 2	-0.001908113	-0.001760533	-0.001495244	-0.004785475
	STD2	0.00112919	0.001344426	0.0014516	0.001804203
	Average3	1.4003428	1.722305831	2.312345965	-4.178796141
	STD3	2.170656194	2.595606021	2.804284086	3.574143694
2	Average 1	1.720643487	2.053608134	1.722105598	-1.133259236
	STD1	2.022735887	2.531301846	2.927282985	3.248059382
	Average 2	-0.001747883	-0.001590306	-0.001787191	-0.003242758
	STD2	0.001011637	0.001266019	0.001464008	0.001624444
	Average3	1.720643487	2.053608134	1.722105598	-1.133259236
	STD3	2.115359269	2.525967153	2.709120597	3.257120844
3	Average 1	1.689327583	2.304935836	-0.547867803	-6.774253473
	STD1	2.101852991	2.675434503	2.781539863	3.324777606
	Average 2	-0.001763556	-0.001469821	-0.002921053	-0.00607661
	STD2	0.001051216	0.001338043	0.001391046	0.001662844
	Average3	1.689327583	2.304935836	-0.547867803	-6.774253473
	STD3	2.161064914	2.682473845	2.618852329	3.025901579
4	Average 1	1.359732973	1.71248722	2.548949382	1.724600213
	STD1	2.060468302	2.760003622	3.113229914	3.072065616
	Average 2	-0.00192837	-0.001763649	-0.001379558	-0.001827037
	STD2	0.001030463	0.001380338	0.001557022	0.001536396
	Average3	1.359732973	1.71248722	2.548949382	1.724600214
	STD3	2.109341858	2.700361996	2.931444244	3.112080664
5	Average 1	1.691577218	2.771411018	2.094677183	-0.937796166
	STD1	2.356761998	2.746576606	2.963672623	3.342092555
	Average 2	-0.001762432	-0.001233841	-0.001600171	-0.00315786
	STD2	0.001178665	0.001373582	0.001482204	0.001671461
	Average3	1.691577218	2.771411018	2.094677183	-0.937796166
	STD3	2.402609671	2.706361126	2.967630712	3.099820388

Table 5 gives the average of the vacancy formation energy for all the temperatures and atomic percent compositions over all five simulations run for each state.

Table 5: Vacancy Formation Energies Calculated Using Method 1

Temp	Zr00	Zr10	Zr20	Zr30
100	-3.333174385	-0.511642805	-0.414206217	-1.440200866
200	-3.044087069	0.422517349	-0.903291653	-1.53660397
300	-1.63464457	1.083699889	0.212259949	-1.874586013
400	-0.485557605	1.16231472	1.076516211	-0.316028245
500	0.086958022	1.470468981	0.972018486	-3.874073751
600	0.856185428	1.746645698	1.548411563	-0.117170697
700	1.285104182	2.069903275	1.461067739	-4.541624199
800	1.572324812	2.112949608	1.626042065	-2.259900961
900	1.799359394	2.379986064	1.167058059	-11.83625143
1000	2.153252159	2.551729845	1.621974316	-12.95504156
1100	2.513527751	2.592697137	1.787654884	-6.701904151
1200	2.646341879	2.819289136	2.118303777	-4.027482191
1300	2.852343146	3.087606225	0.928831125	-13.07436566
1400	3.034759937	3.058890675	1.592596337	-7.988685364

When looking at the vacancy formation energies the different alloys over temperature, it is seen that the vacancy formation energies come out negative for the low temperatures. This is due to the fact that BCC uranium does not actually form until 1045 K. So with the phase not necessarily existing at such low temperatures, it is much more likely for a negative vacancy formation energy. As the temperature goes up, the vacancy formation energy tends to find a value similar to those previously reported in the literature. However, this is not always the case. With 30%-Zr, the vacancy formation energies never reach a positive value and the 20%-Zr alloys start to dip a little at higher temperatures. At high temperatures in BCC phase uranium, there is an increase in the formation of vacancy-interstitial pairs. The creation of these pairs increases both $E_{(n-1)}$ and E_n, but increases E_n more. For a relatively small simulation cell where vacancy interstitial pair formation is rare and the simulation cell will either have one vacancy-interstitial pair or none. Once a pair has formed, the pair cannot annihilate unless the interstitial and vacancy meet again. But if the simulation cell already had a vacancy, the vacancy-interstitial pair would exist for a shorter time because the interstitial now has two vacancies to meet and remove

the pair. Therefore, the energy of the perfect lattice, E_n, is increased more because vacancy-interstitial pairs last longer there (Mendelev 2010). In fact, if you look at Figures 37 and 38 (in the Wigner-Seitz defect section) showing the number of defects in the simulation cell at the end of both the perfect and vacancy stage, you will see that the number of defects go up with temperature and with the amount of zirconium in the alloy. The effect of formation of vacancy-interstitial pairs on the vacancy formation energy can be seen in both the figures over change in temperature and in zirconium composition of the alloy.

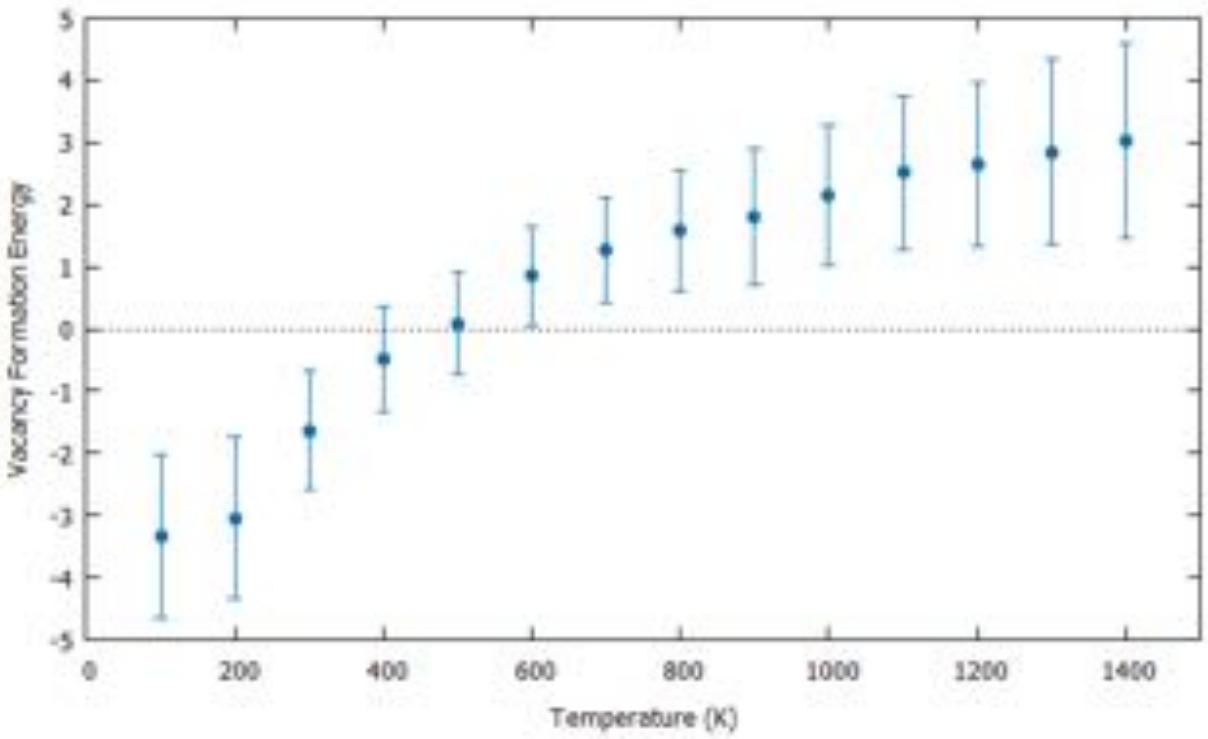

Figure 14: Vacancy Formation Energy vs Temperature for 0%-Zr

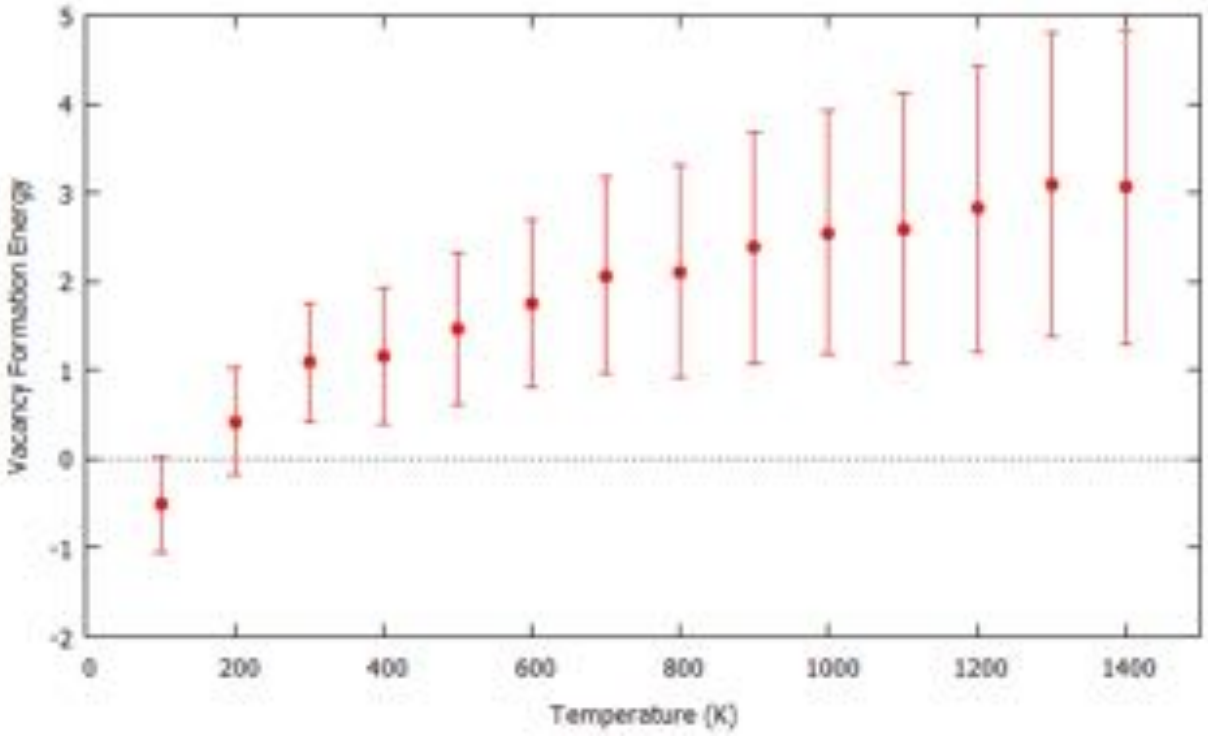

Figure 15: Vacancy Formation Energy vs. Temperature for 10%-Zr

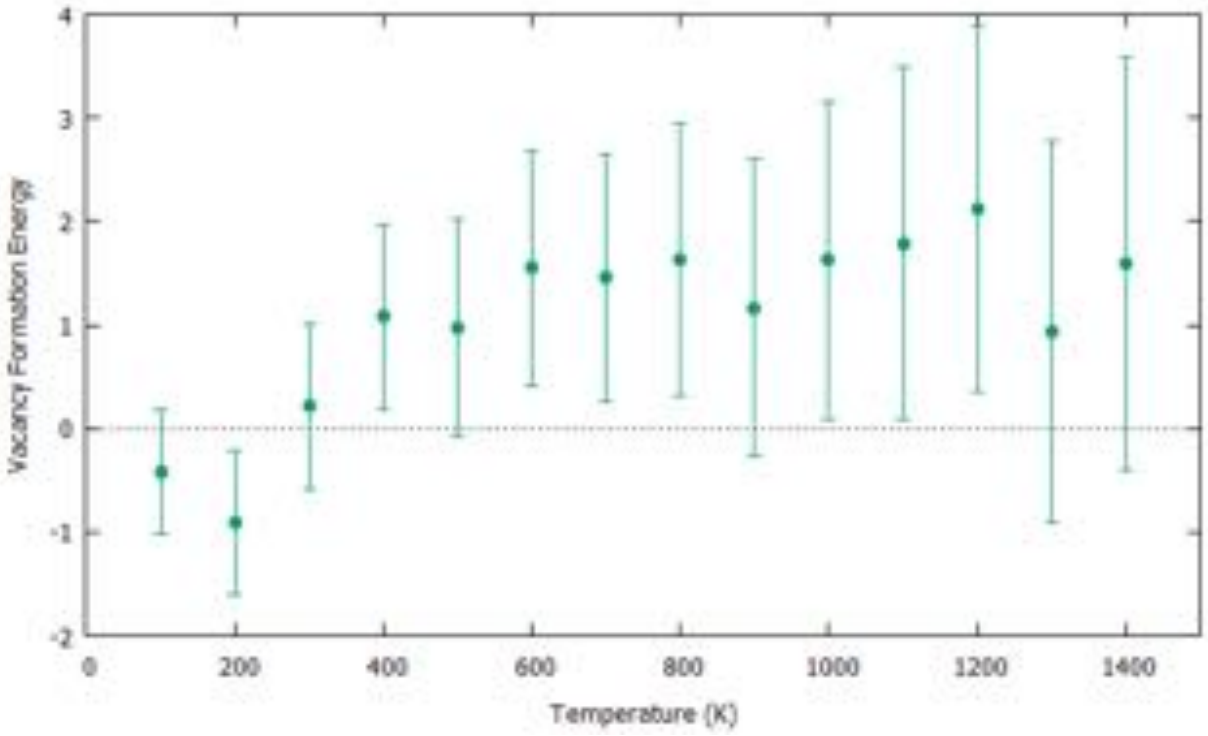

Figure 16: Vacancy Formation Energy vs. Temperature for 20%-Zr

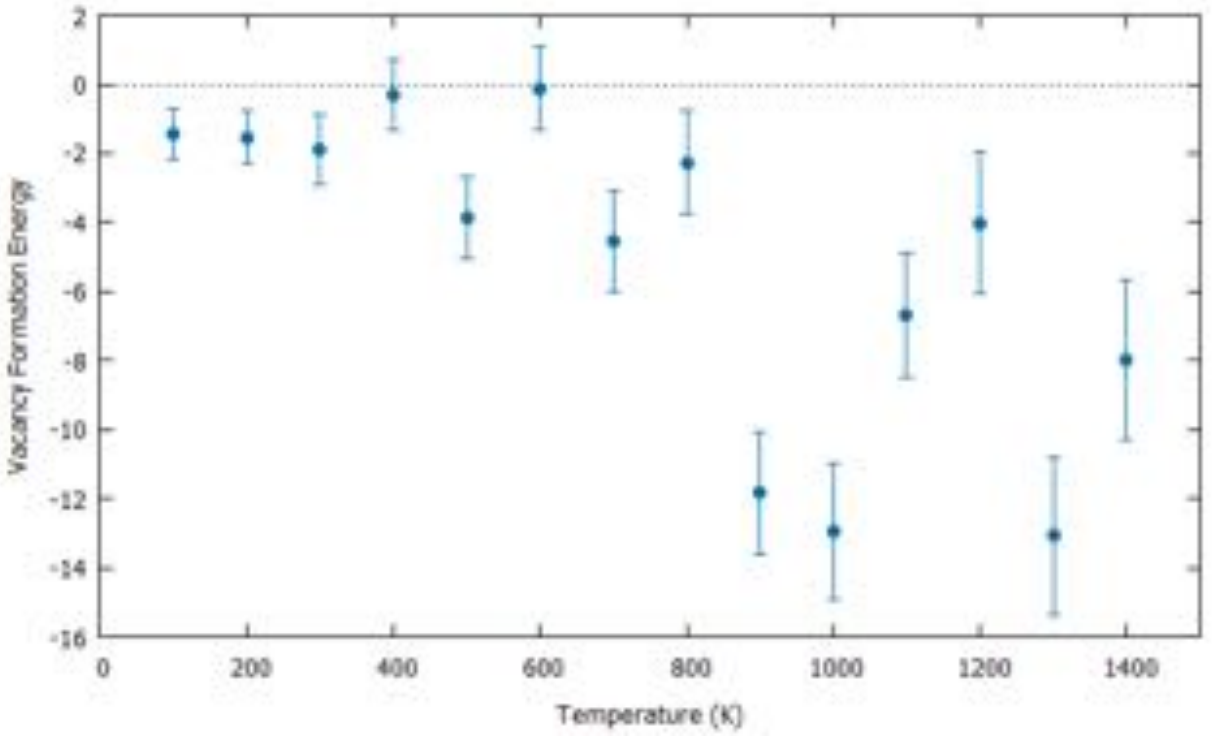

Figure 17: Vacancy Formation Energy vs. Temperature for 30%-Zr

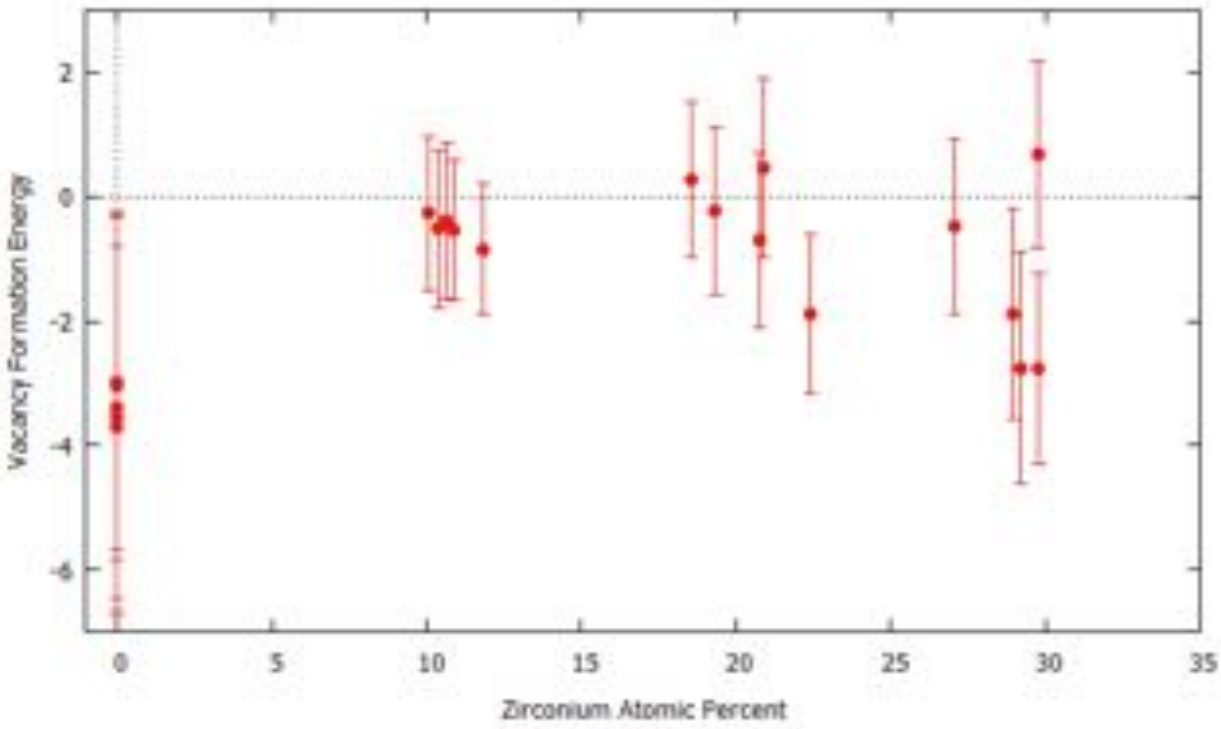

Figure 18: Vacancy Formation Energy vs. Zirconium Atomic Percent for 100 K

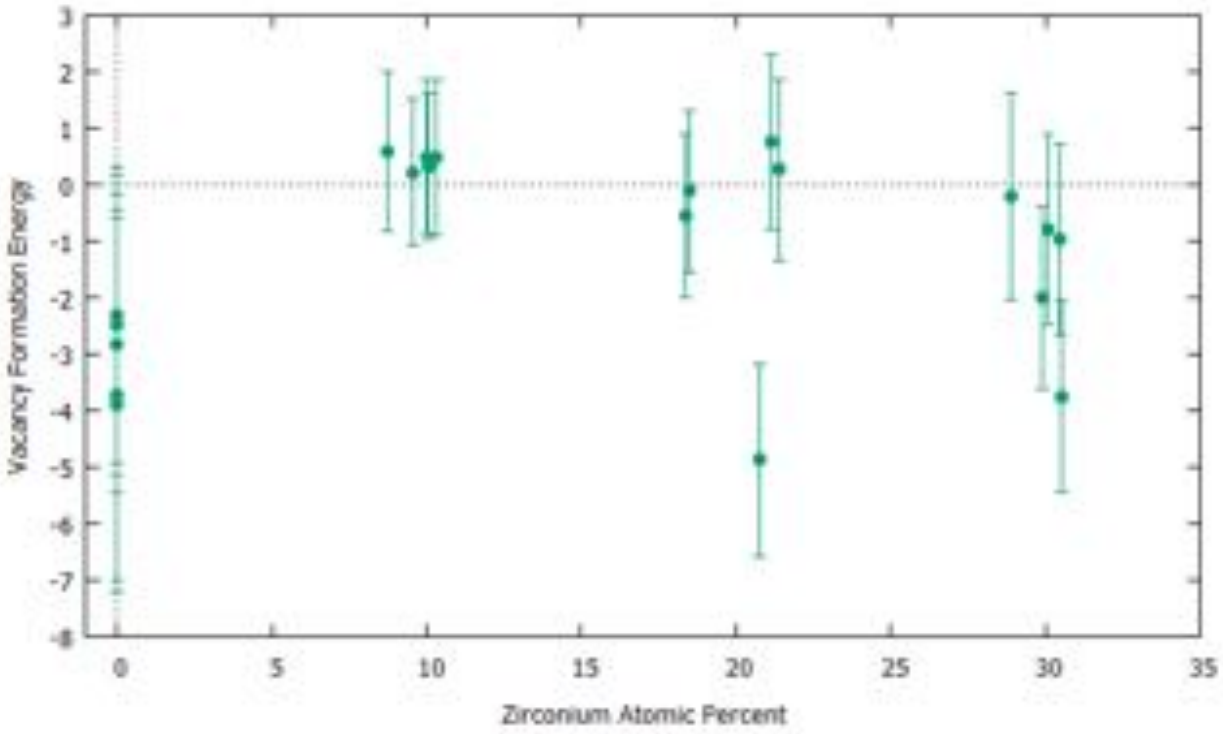

Figure 19: Vacancy Formation Energy vs. Zirconium Atomic Percent for 200 K

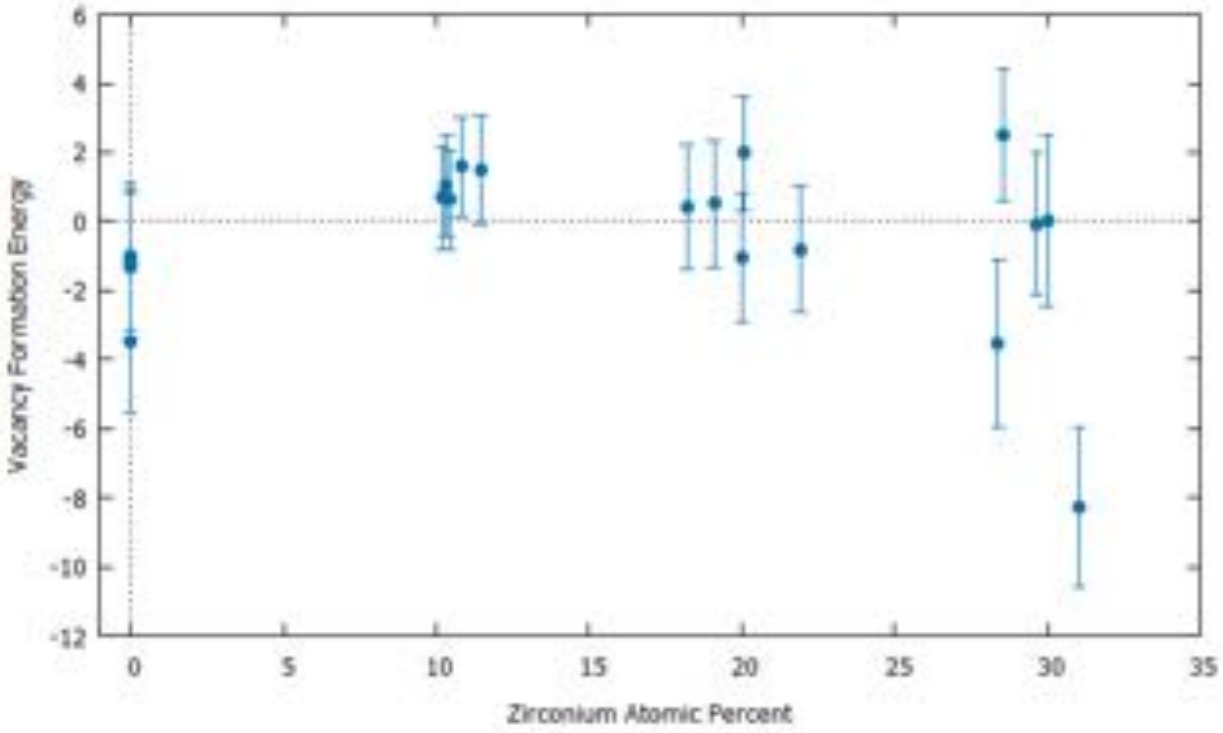

Figure 20: Vacancy Formation Energy vs. Zirconium Atomic Percent for 300 K

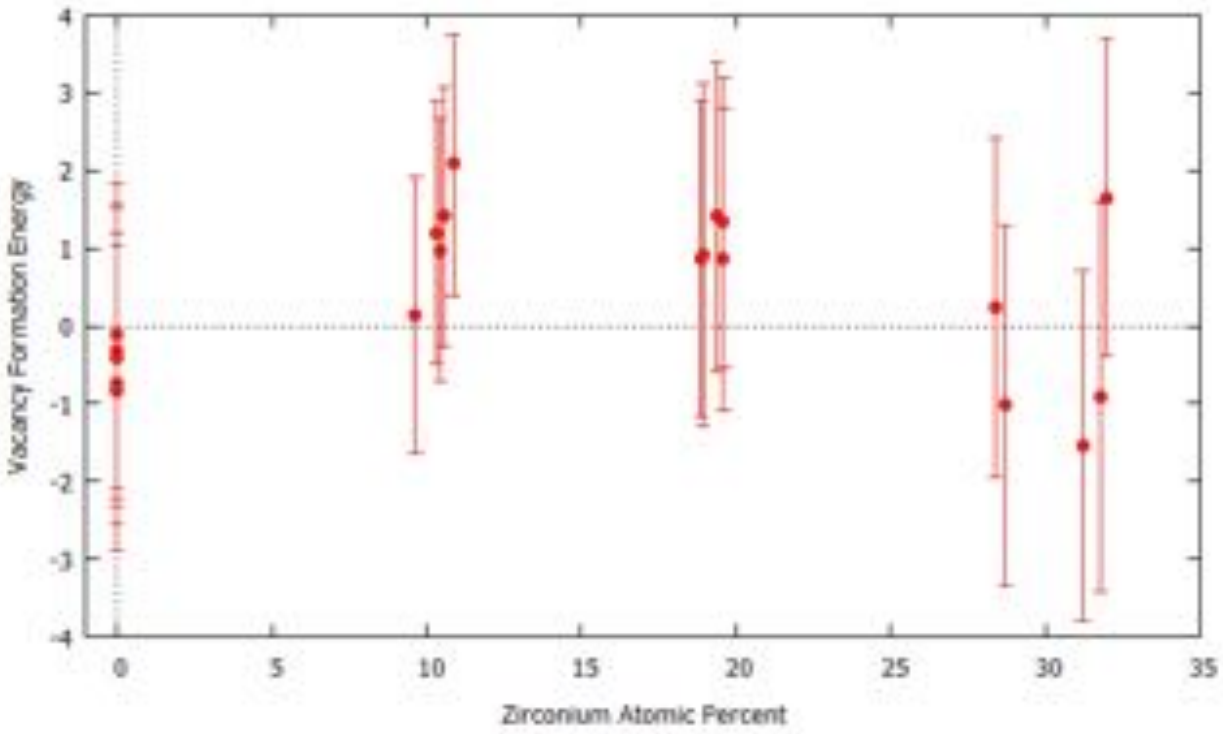

Figure 21: Vacancy Formation Energy vs. Zirconium Atomic Percent for 400 K

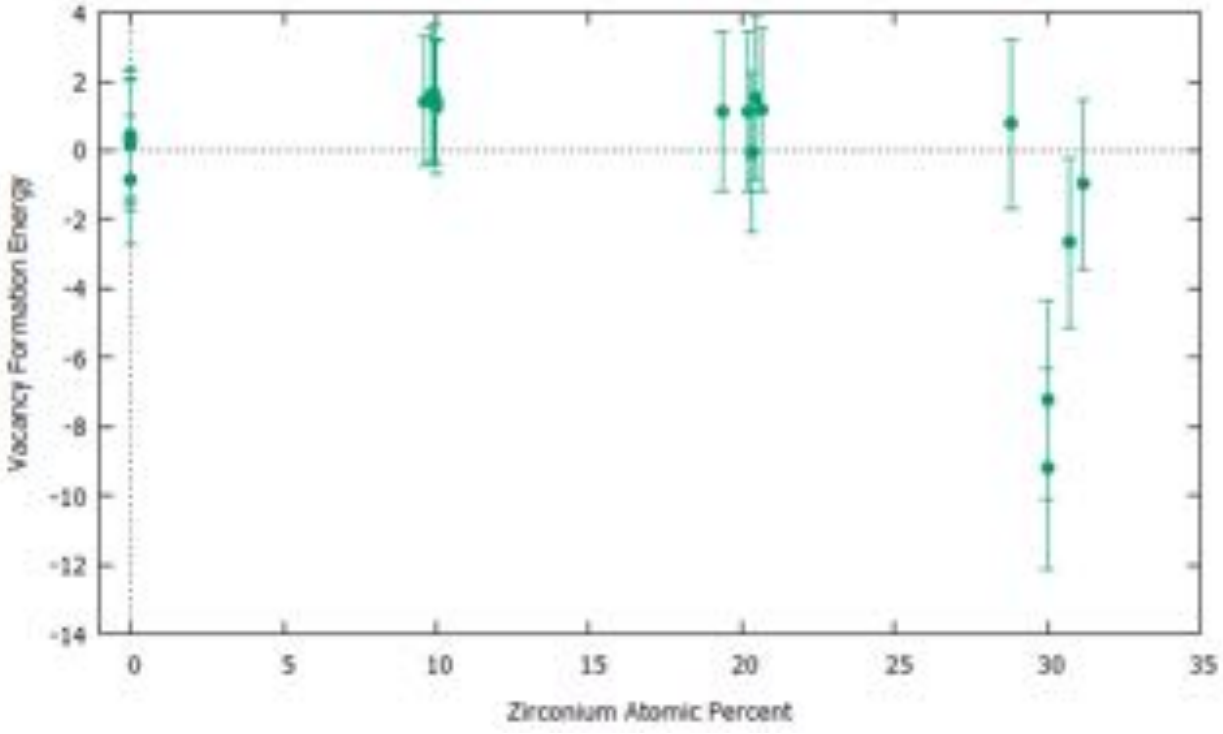

Figure 22: Vacancy Formation Energy vs. Zirconium Atomic Percent for 500 K

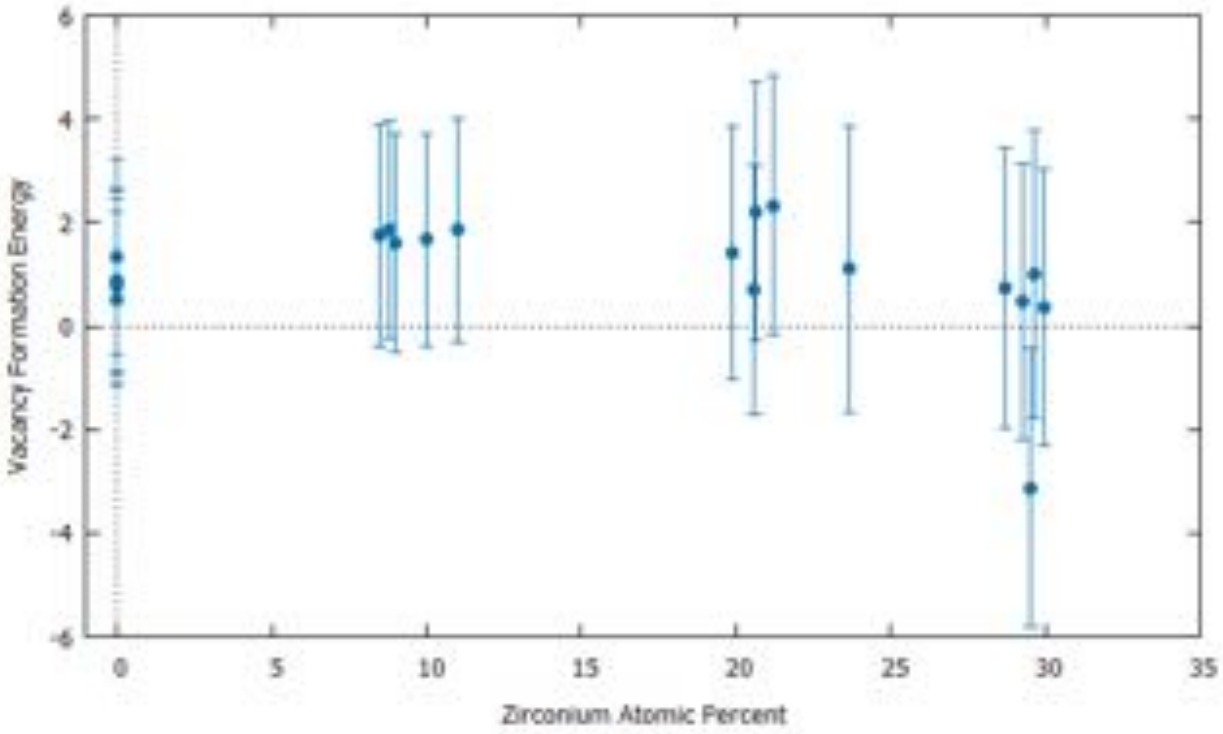

Figure 23: Vacancy Formation Energy vs. Zirconium Atomic Percent for 600 K

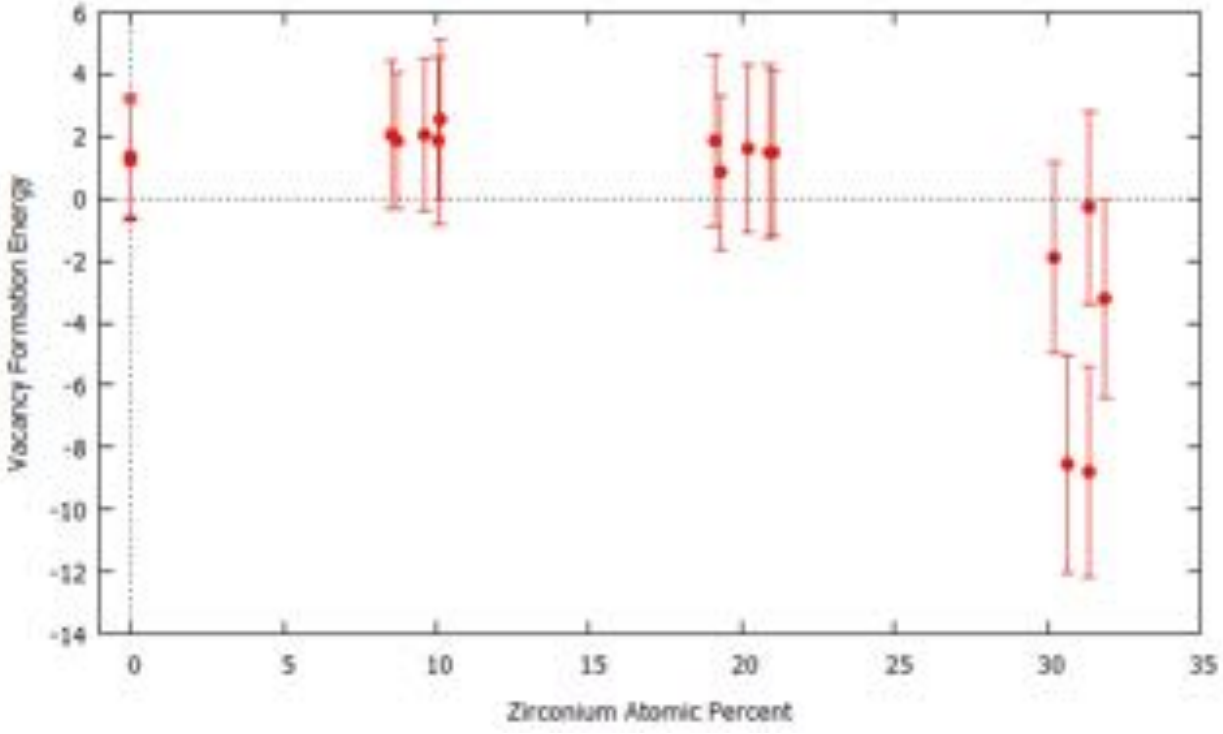

Figure 24: Vacancy Formation Energy vs. Zirconium Atomic Percent for 700 K

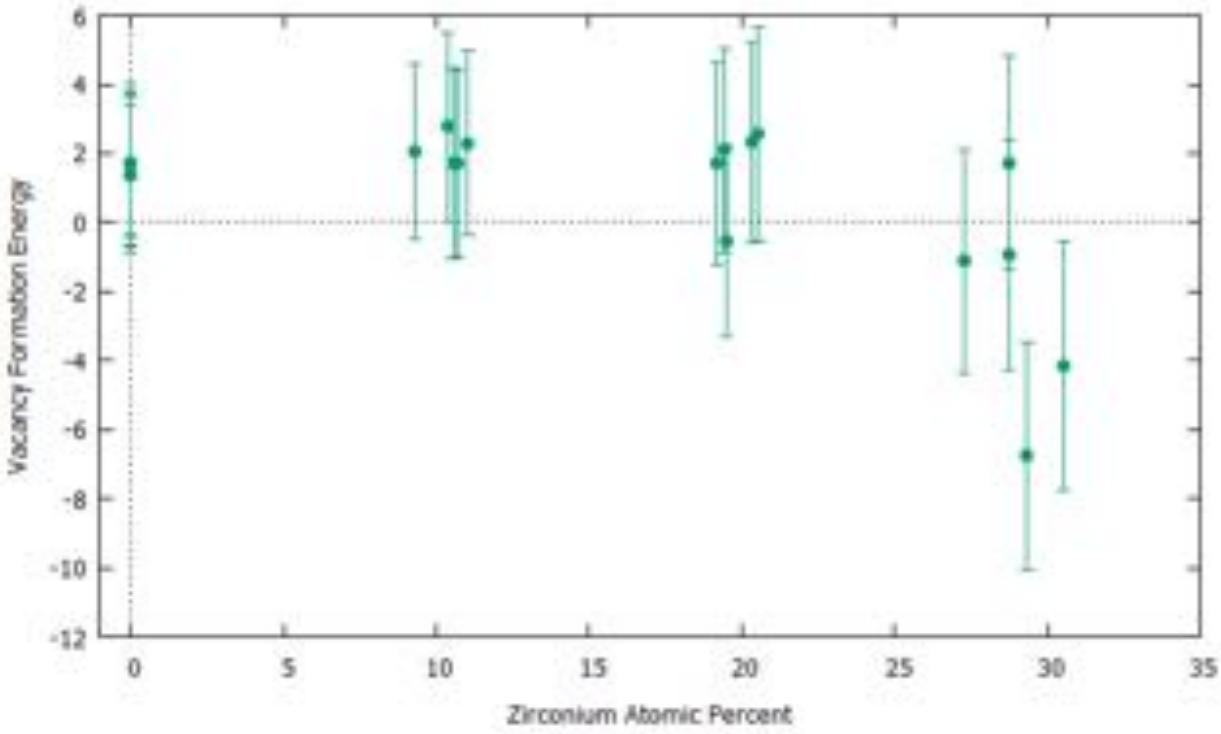

Figure 25: Vacancy Formation Energy vs. Zirconium Atomic Percent for 800 K

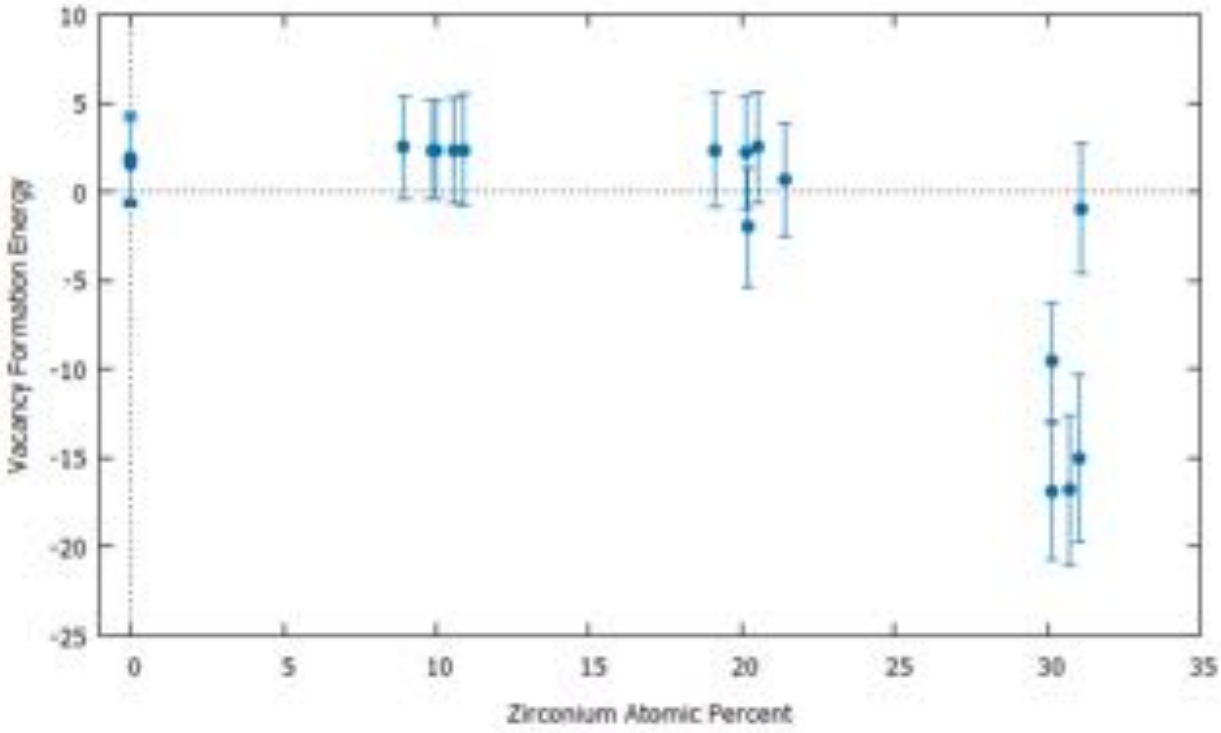

Figure 26: Vacancy Formation Energy vs. Zirconium Atomic Percent for 900 K

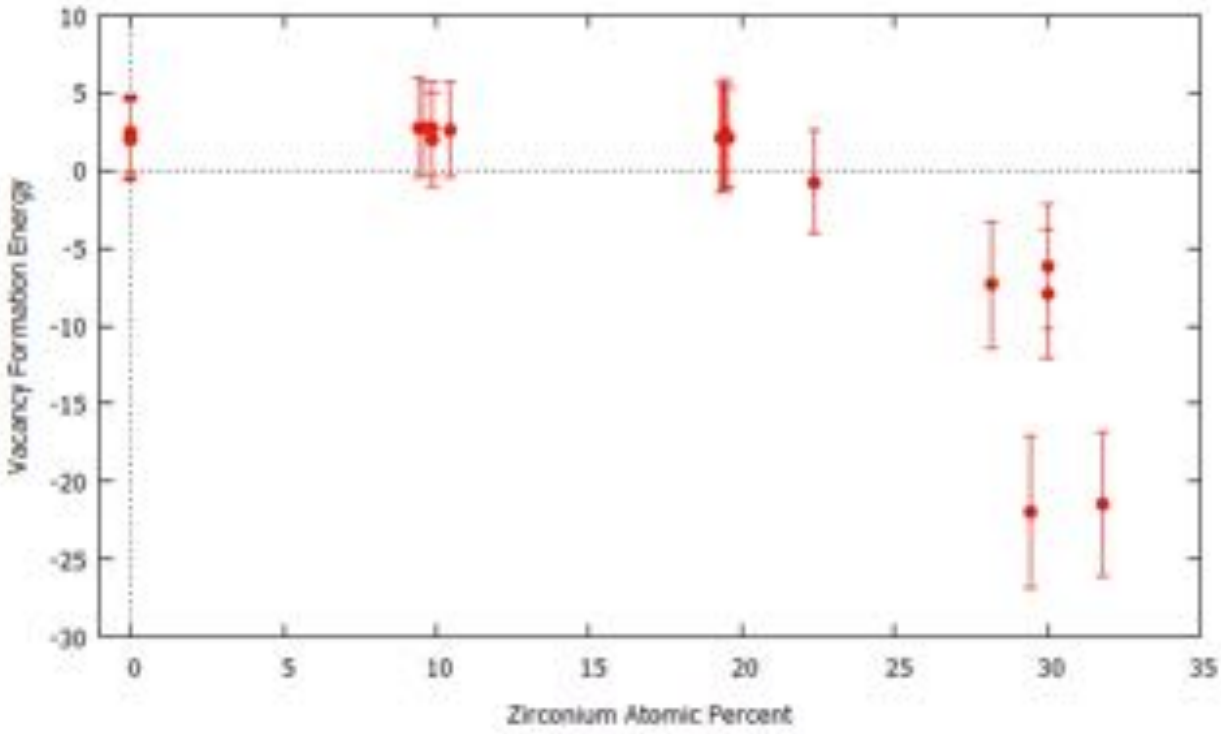

Figure 27: Vacancy Formation Energy vs. Zirconium Atomic Percent for 1000 K

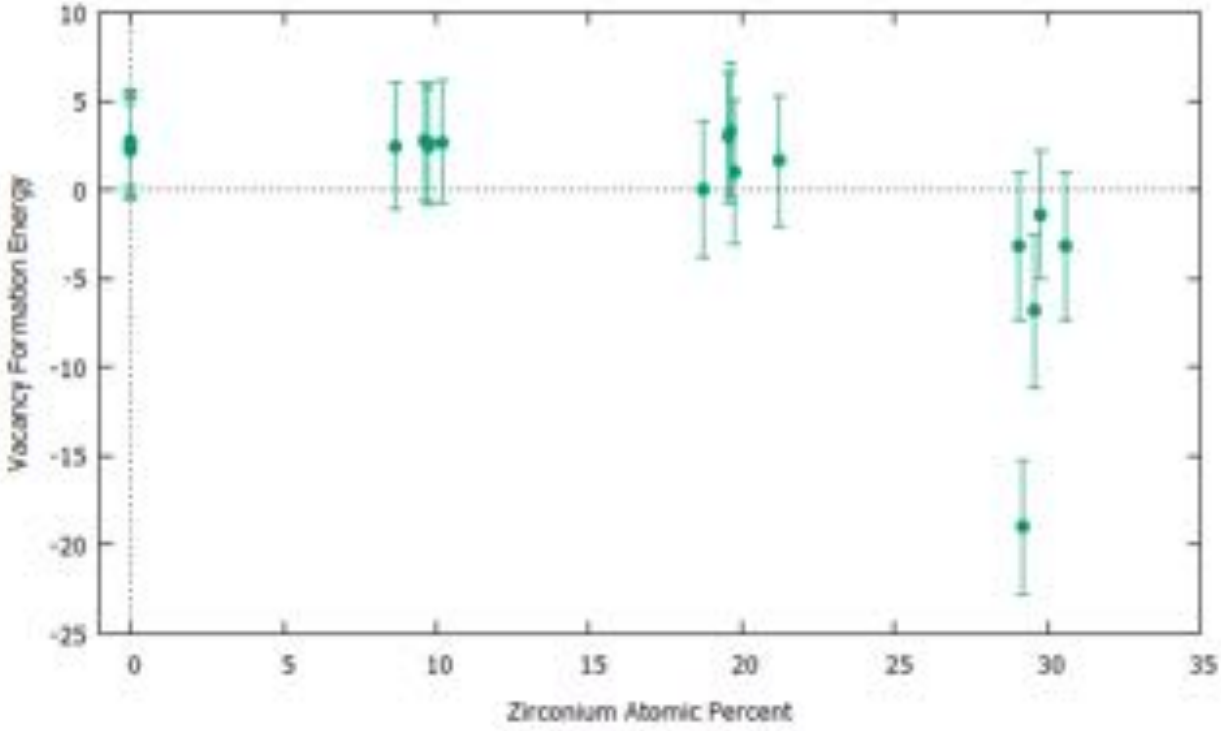

Figure 28: Vacancy Formation Energy vs. Zirconium Atomic Percent for 1100 K

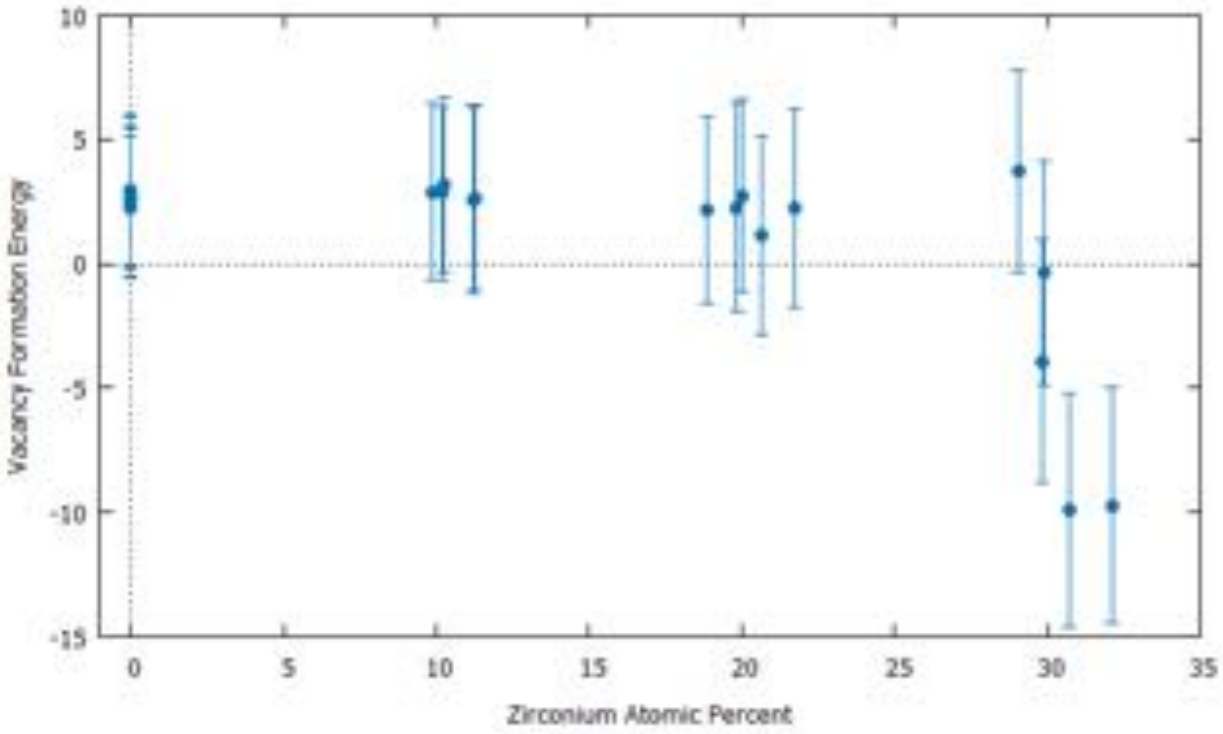

Figure 29: Vacancy Formation Energy vs. Zirconium Atomic Percent for 1200 K

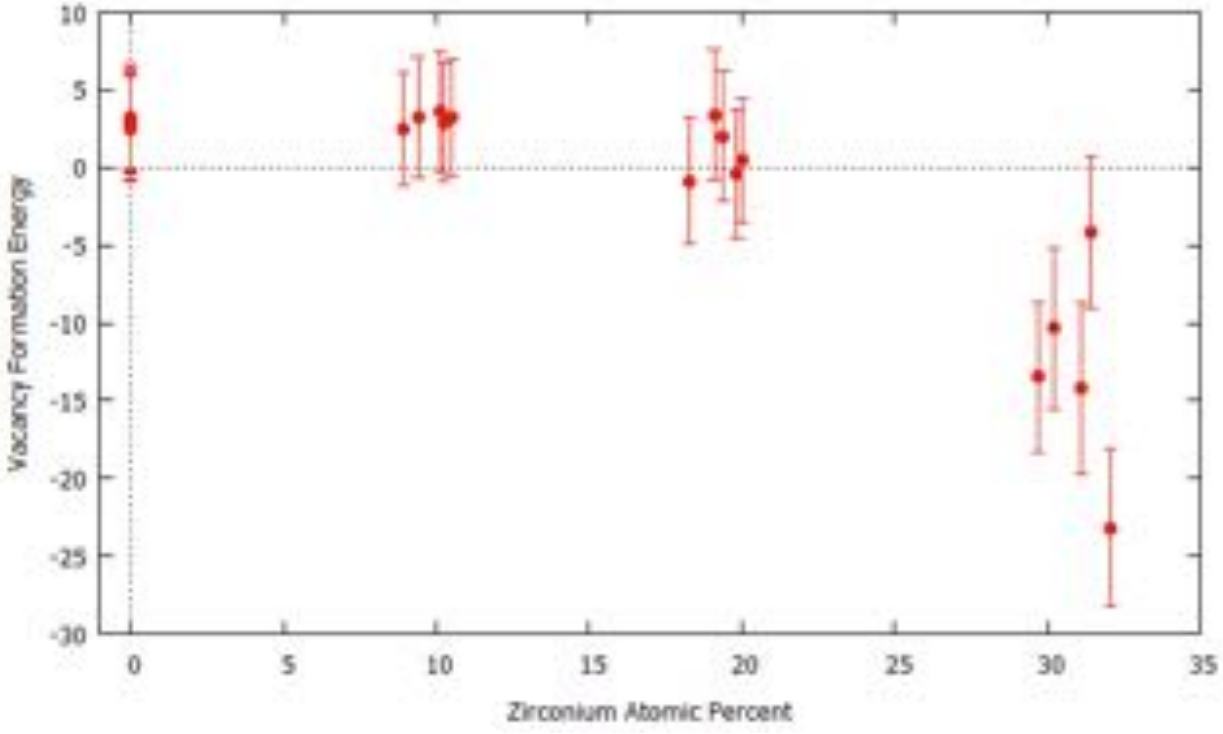

Figure 30: Vacancy Formation Energy vs. Zirconium Atomic Percent for 1300 K

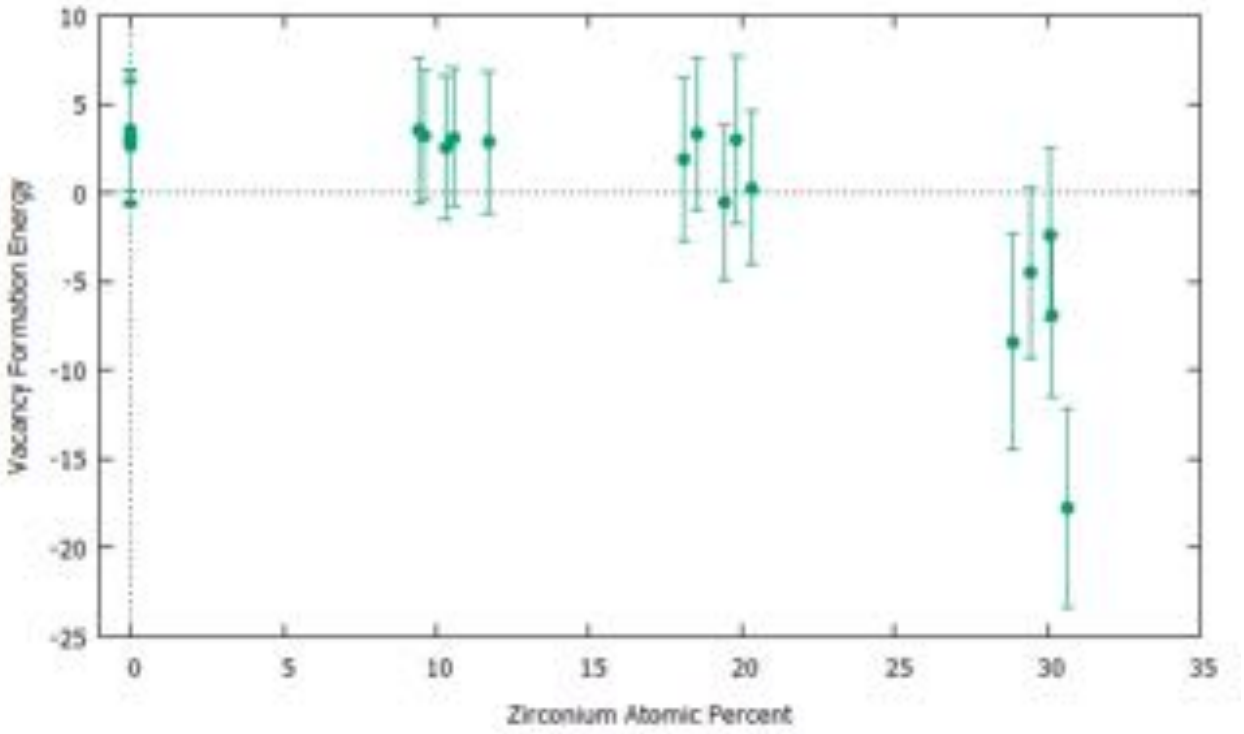

Figure 31: Vacancy Formation Energy vs. Zirconium Atomic Percent for 1400 K

Nearest Neighbors

Because the material being examined is an alloy, there is a significant chance that the composition of the nearest neighbors to the atom that is removed to create the vacancy will have a strong effect on the vacancy formation energy. To look at the effect of the nearest neighbors, a structure of 30% atomic zirconium alloy was chosen as the initial structure, and the eight nearest neighbors to the vacancy were specifically set each time, going from all eight being uranium atoms one-by-one to all eight as zirconium. For all nine configurations, the rest of the atoms were exactly the same as the exact same random number seed was used for the alloyization process. In addition, the simulation was done at 0 K to reduce any possible changes in the vacancy formation energy due to thermal movement and at 1400 K, the extreme limit of the alloy

before reaching the melting point. The results are shown below in Tables 6 and 7 and Figures 32 and 33.

Table 6: Short Range Order and Vacancy Formation Energy for 0 K

Number of Nearest Neighbors	Short Range Order	Vacancy Formation Energy
0U8Zr	-0.007104851	-12.64398445
1U7Zr	-0.007429467	-19.22307885
2U6Zr	-0.0083281	-20.10604145
3U5Zr	-0.007496069	-20.09233219
4U4Zr	-0.007814961	-18.35382658
5U3Zr	-0.007555205	-18.80517178
6U2Zr	-0.007871248	-17.27299004
7U1Zr	-0.007029272	-19.29089834
8U0Zr	-0.007337559	-15.72866253

Table 7: Short Range Order and Vacancy Formation Energy for 1400 K

Number of Nearest Neighbors	Short Range Order	Vacancy Formation Energy
0U8Zr	-0.022303055	-25.16010849
1U7Zr	-0.020269726	-14.26362552
2U6Zr	-0.019987903	-17.54727832
3U5Zr	-0.018529887	-13.07442841
4U4Zr	-0.018822816	-13.75168474
5U3Zr	-0.017358185	-17.92938221
6U2Zr	-0.017646104	-18.34244467
7U1Zr	-0.016170732	-22.95034186
8U0Zr	-0.015867264	-10.15394285

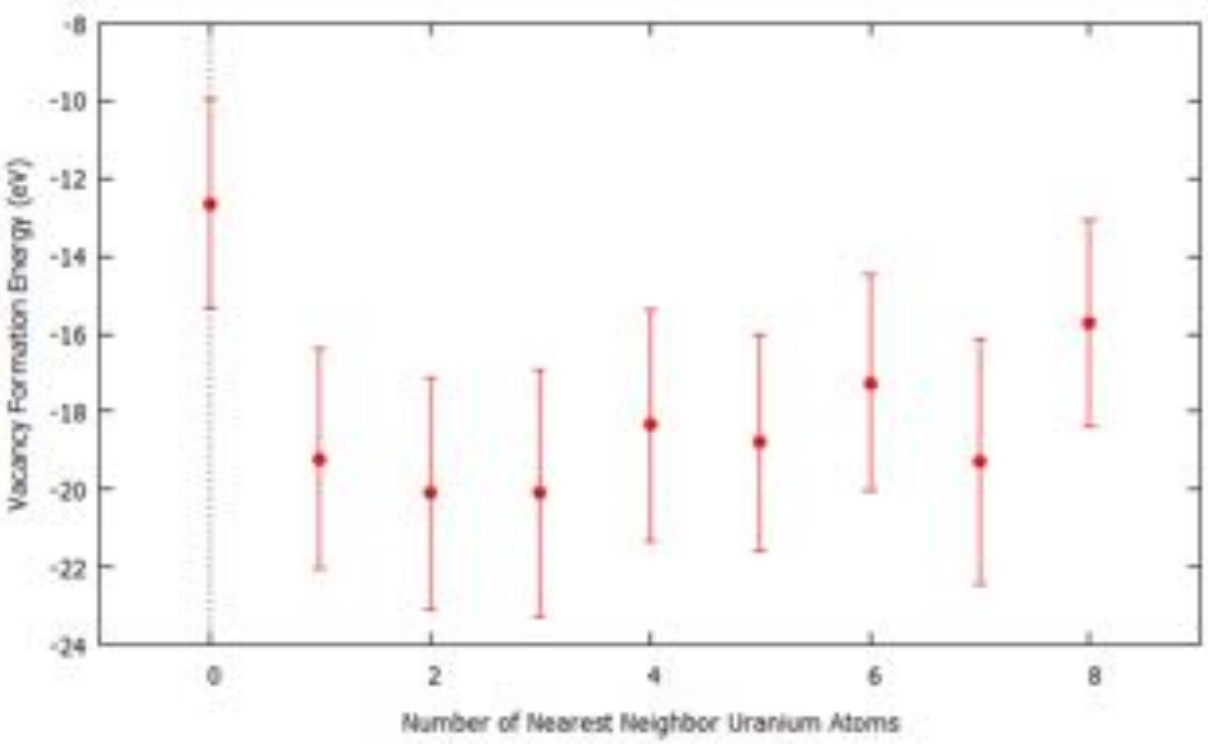

Figure 32: Vacancy Formation Energy of 0 K as Nearest Neighbors Change

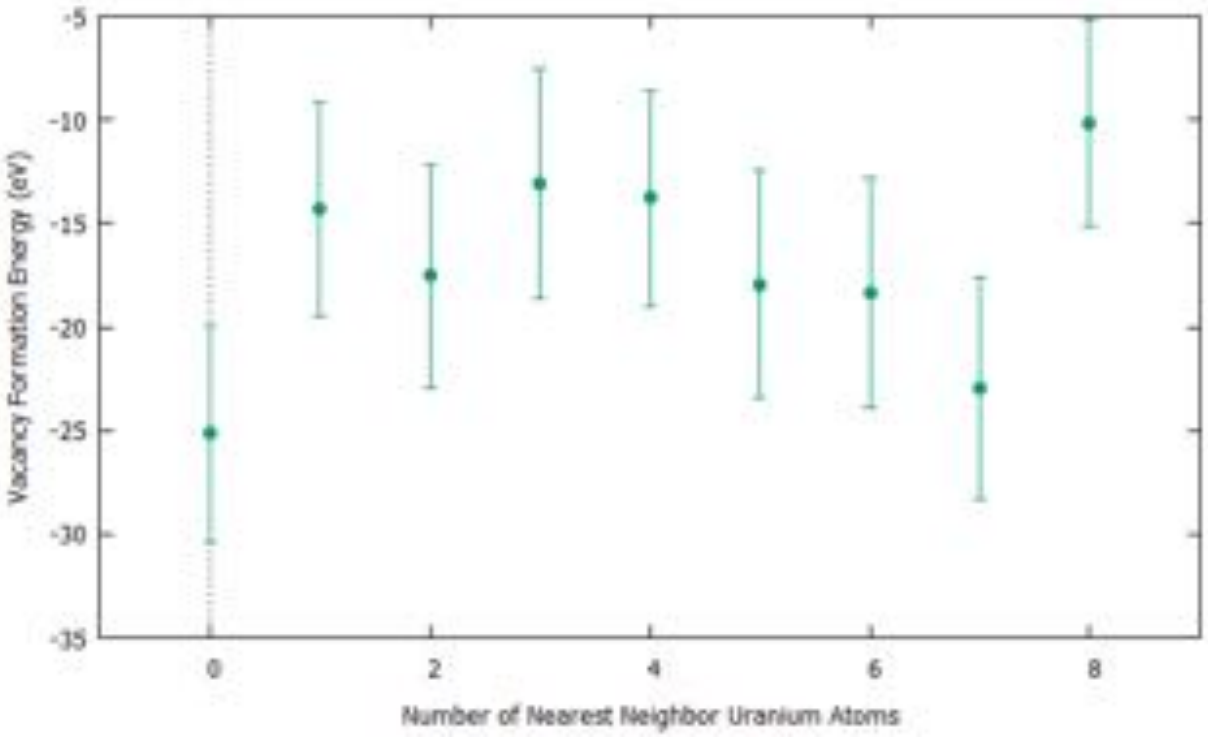

Figure 33: Vacancy Formation Energy of 1400 K as Nearest Neighbors Change

As can be seen in both figures, the nearest neighbors of the vacancy do not seem to predict any significant pattern in the formation energy. This indicates that both uranium and zirconium provide a similar effect to the vacancy. It also may imply that vacancy formation energy is influenced heavily by atoms that do not make up the nearest neighbors.

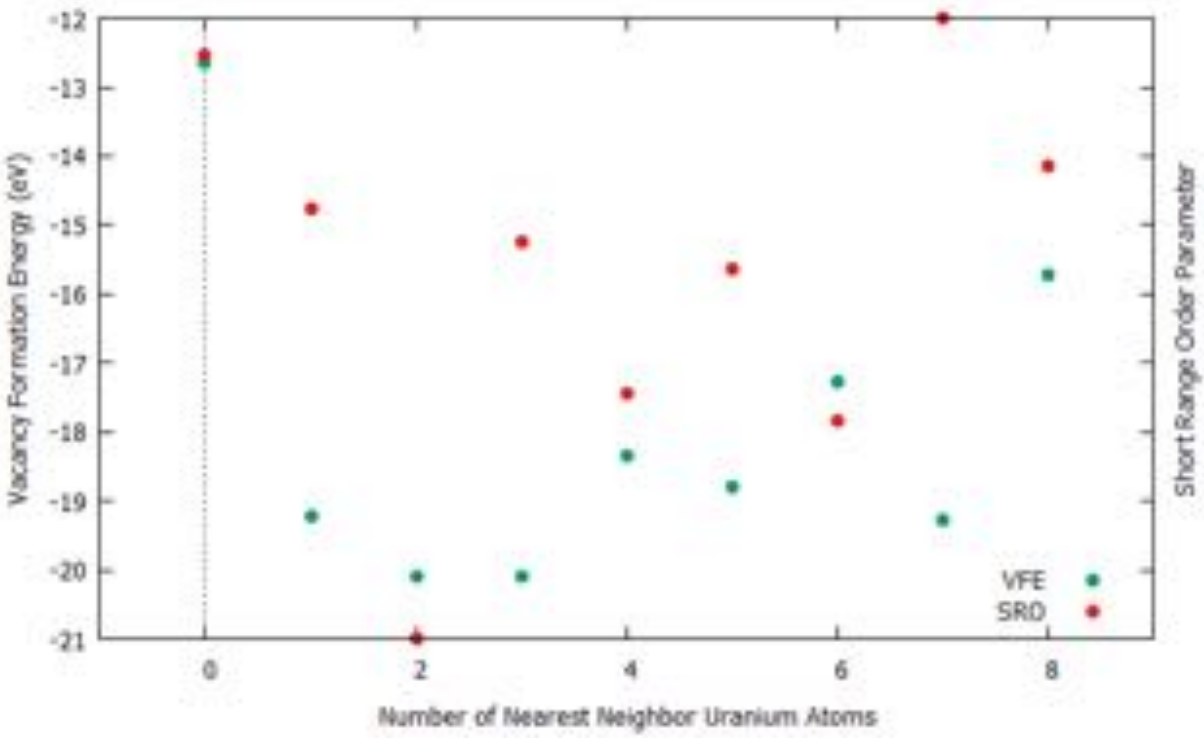

Figure 34: 0 K Vacancy Formation Energy and Short Range Order Parameter

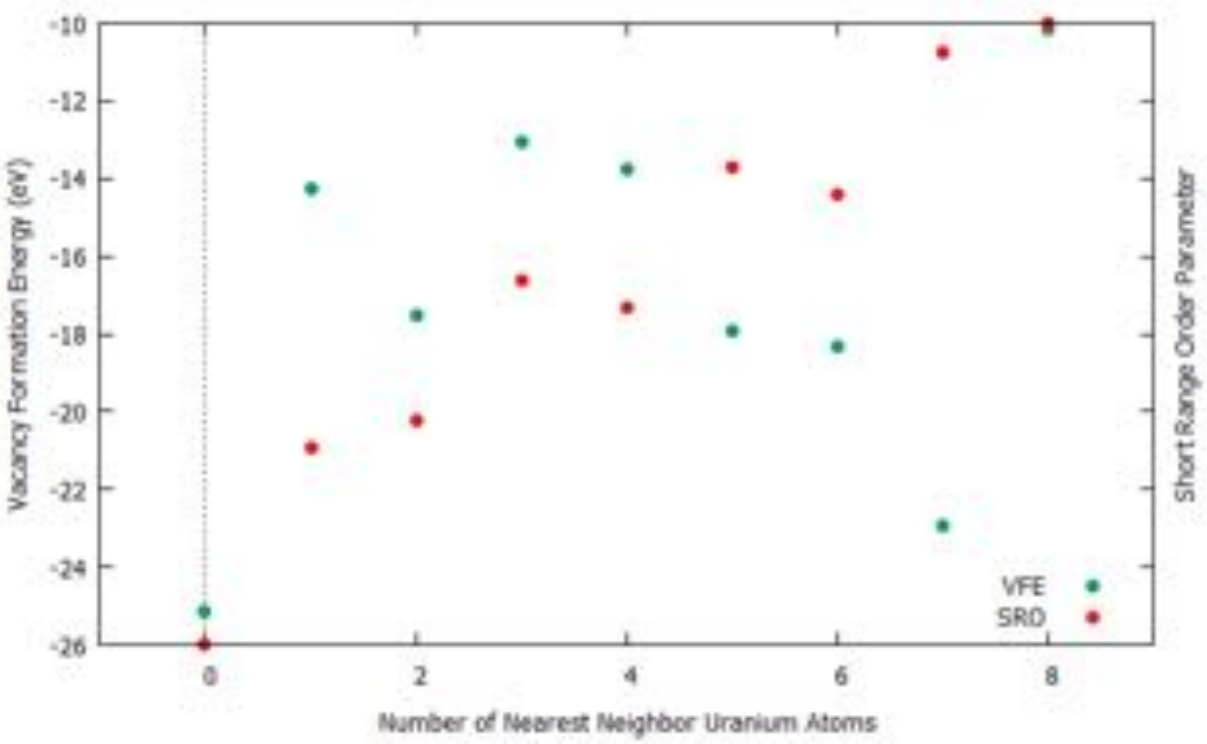

Figure 35: 1400 K Vacancy Formation Energy and Short Range Order Parameter

Looking at Tables 6 and 7 above, we see that the short range order parameters are incredibly close to zero in both temperature cases. In other words, both systems are totally random, as one would expect based on using a random process to perform the alloyization. It's also of vital importance to see if the short range order seems to follow a similar pattern to the vacancy formation energy, potentially showing a more complex link between nearest neighbors and the vacancy formation energy. However, Figures 34 and 35 both refute this, both showing the short range order parameter and vacancy formation energy seeming to jump around randomly, with no discernible relation between the two.

Wigner-Seitz Defect Analysis

As previously mentioned above, vacancy-interstitial pairs have a very significant effect on the vacancy formation energy calculated through use of the simulation. These pairs increase the energy of the perfect lattice more than the lattice with the vacancy introduced due to the fact

that there are more vacancies for the interstitial to find and remove the pair in the latter case. As one could assume, this effect is more profound as the temperature of the simulation is increased, since the movement of the particles is increased as the temperature increases and therefore more likely to end up in another lattice position. However, this effect is also notable when the atomic percentage of zirconium increases. This could be due to the fact that the atomic lattice was initialized using uranium lattice constants, and once zirconium atoms are placed instead, the incorrect lattice constants allow more vacancy-interstitial pairs to be created.

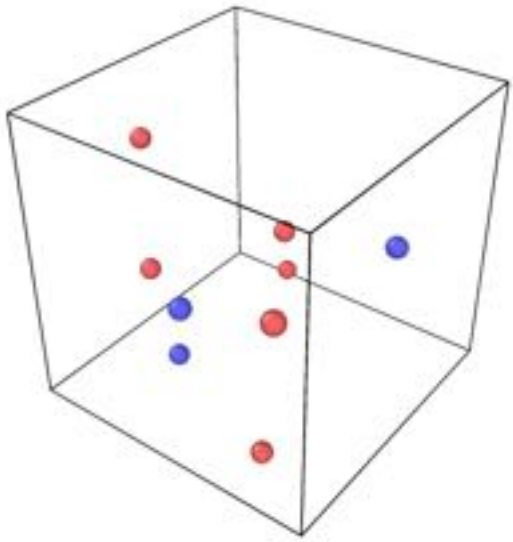

Figure 36: Vacancies and Interstitials During Final Step of U-30%Zr at 1200 K (Red and Blue are Uranium and Zirconium Starting Positions, Respectively)

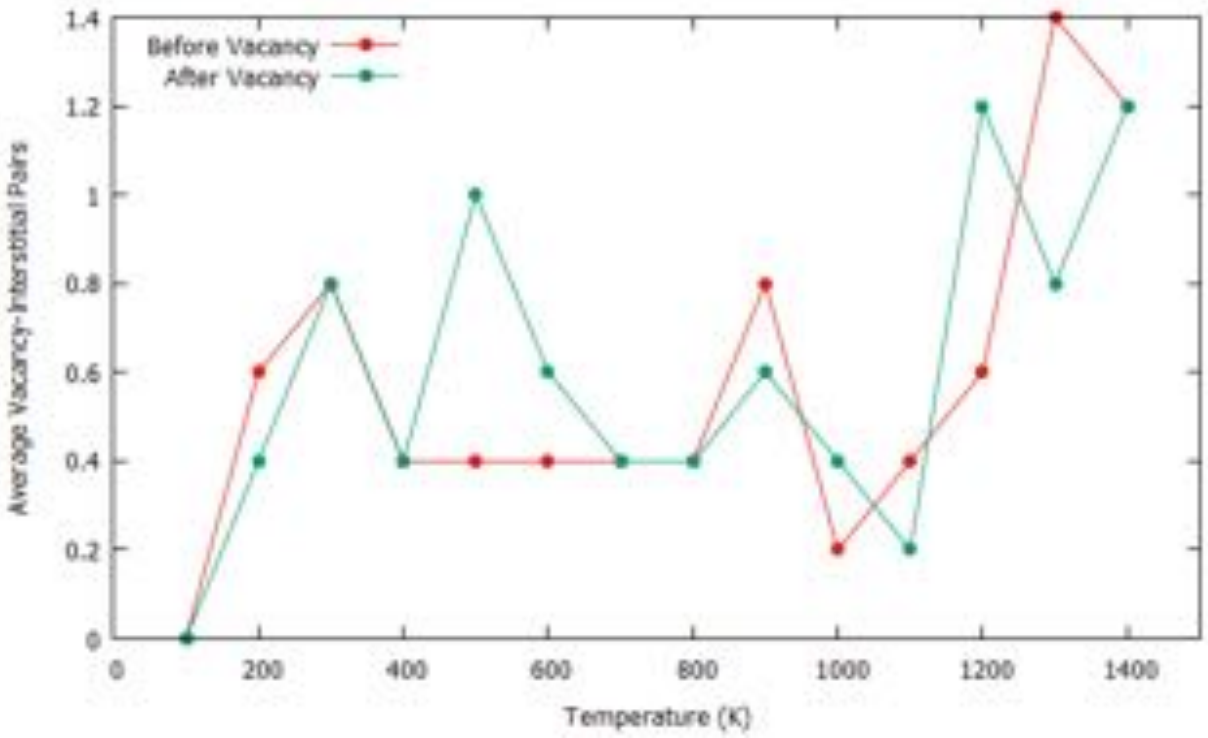

Figure 37: Average Number of Vacancy-Interstitial Pairs vs. Temperature for Zr-20%

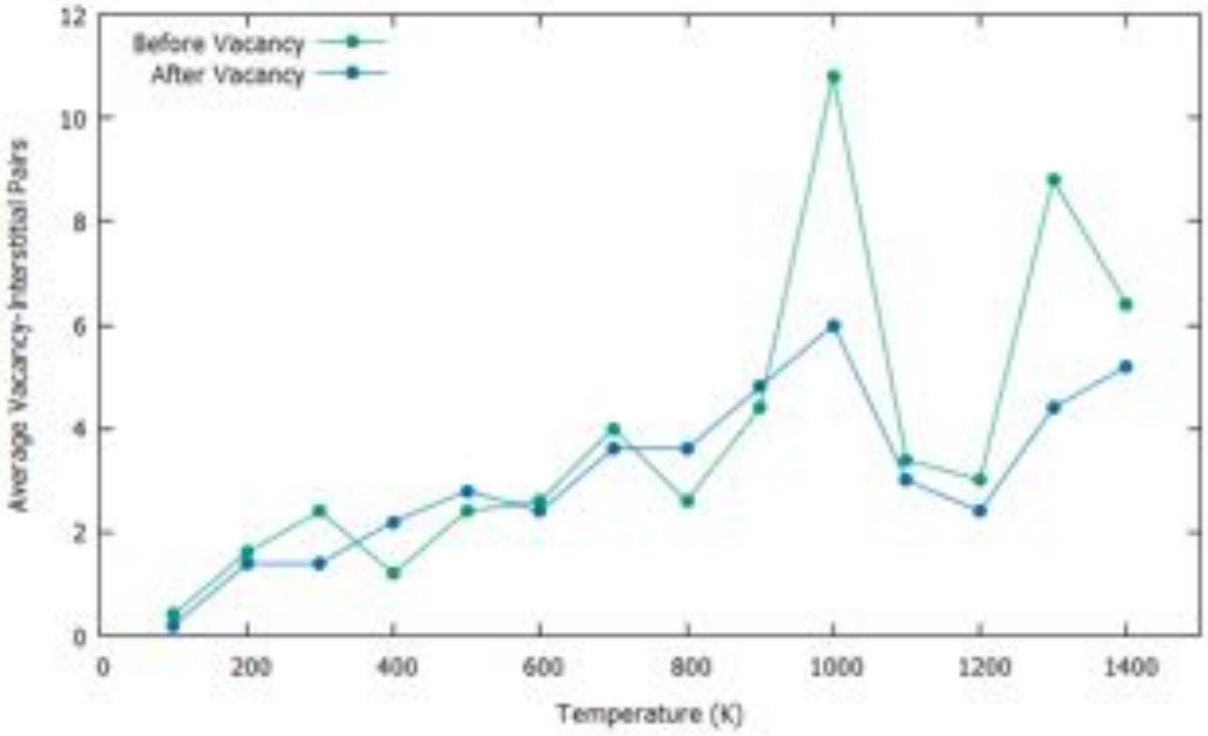

Figure 38: Average Number of Vacancy Interstitial Pairs vs. Temperature for Zr-30%

It should be mentioned that Figures 37 and 38 were created using the number of vacancy-interstitial pairs at the end of each portion of the run and then averaging all five runs of temperature and atomic percentage conditions in order to make each data point. While this misses out on times when there are more vacancy-interstitial pairs in the middle of the run, it does a good job of showing the general trend of more vacancy-interstitial pairs as the temperature increases and as the atomic-percentage of zirconium increases. The pure uranium cases and the Zr-10% cases were not included because there was only one single case that ended with a vacancy-interstitial pair. Despite this, there were several simulations where vacancy-interstitial pairs were created during the runs but had rejoined before the simulation was done.

It's also interesting to note that both Zr-20% and Zr-30% experience a drop in the number of defect pairs around 1000 K, which is the temperature at which the BCC γ-uranium and β-zirconium allotropes actually begin to form. It seems that once the simulations are being run at realistic temperatures for the BCC-phases to exist, the likelihood of vacancy-interstitial pairs being created decreases. However, the increased energy due to higher temperatures still leads to more defect pairs, especially as the melting point of the alloy is almost reached.

Common Neighbor Analysis

Common Neighbor Analysis is used to ensure that the alloy remains in the BCC phase throughout the simulation by using an algorithm to analyze the local atoms and determine which part of the structure is in which phase. Similar to the formation of vacancy-interstitial pairs, the percentage of the structure that remains in the BCC phases decreases as both temperature and the atomic-percentage of zirconium increase.

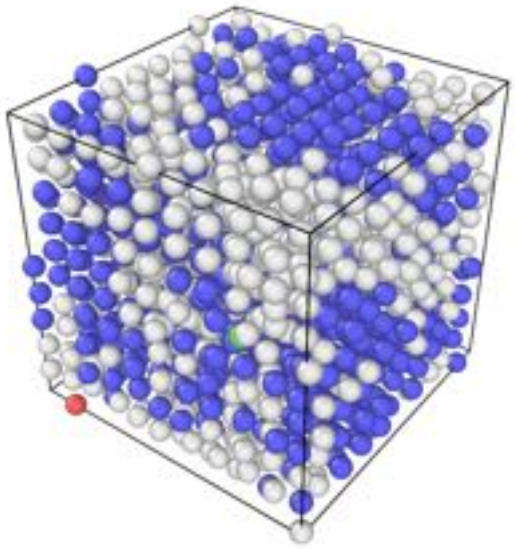

Figure 39: Common Neighbor Analysis of U-30%Zr at 1200 K (Blue = BCC, Green = FCC, Red = HCP, Gray = Other)

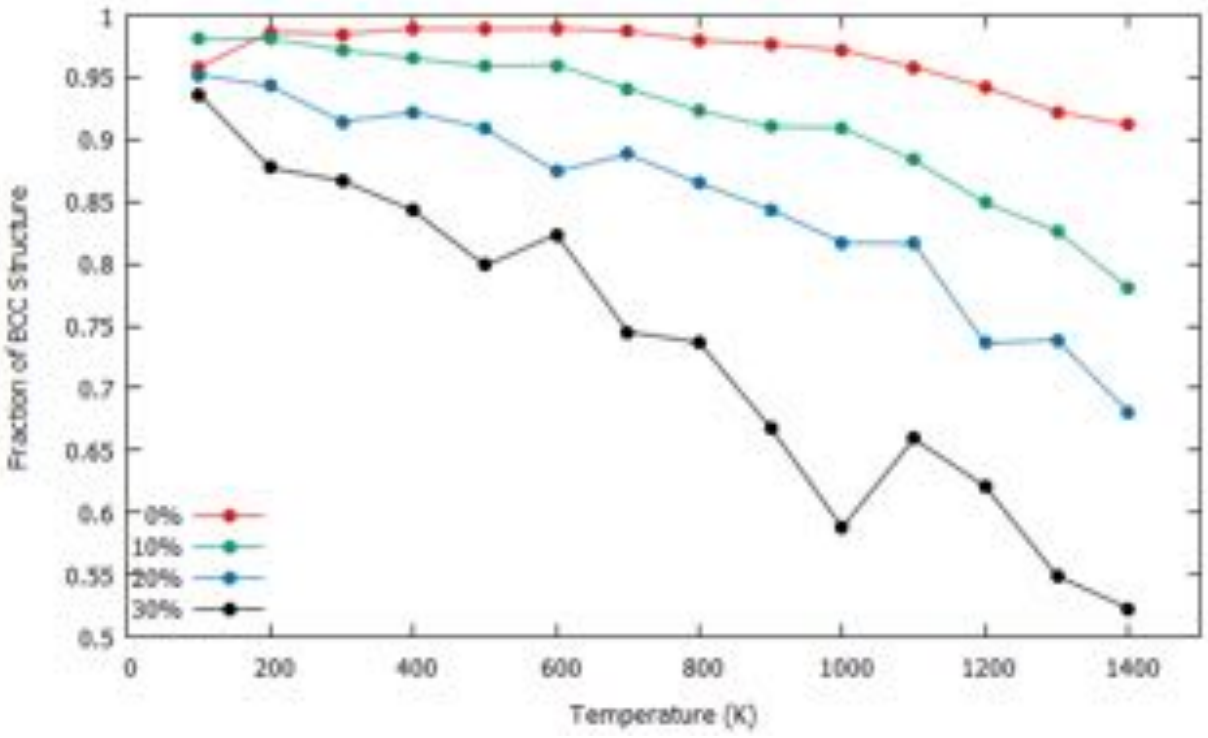

Figure 40: Fraction of Simulation in BCC Phase vs. Temperature

Figure 40 shows the decrease in BCC structure for the four different alloys as temperature increases. This decrease is much more obvious as the percentage of zirconium increases, with Zr-30% nearly reaching less than 50% BCC phase. It's also worth nothing that, as in the vacancy-interstitial pair formation, there is a break in the pattern after 1000 K. The Zr-20% simulations seem to level out in the decreasing BCC fraction, while Zr-30% actually jumps back up. After this point, all of the conditions have a much more quickly decreasing BCC fraction, which can be seen more obviously in Figure 39 below, focusing solely on the pure uranium case. Again, it seems likely that this is due to the fact that the phases being studied actually exist in reality around 1000 K.

Interestingly, the pure uranium simulations experience a brief increase before actually decreasing around 600 K. As previously discussed, this initial increase could be due to the fact that all of the lattice constants properly apply to all of the atoms in the simulation, allowing the simulations to retain their structure before the increased temperature imparts enough energy to lead to a bit of a break down of the BCC structure, as shown zoomed in in Figure 41.

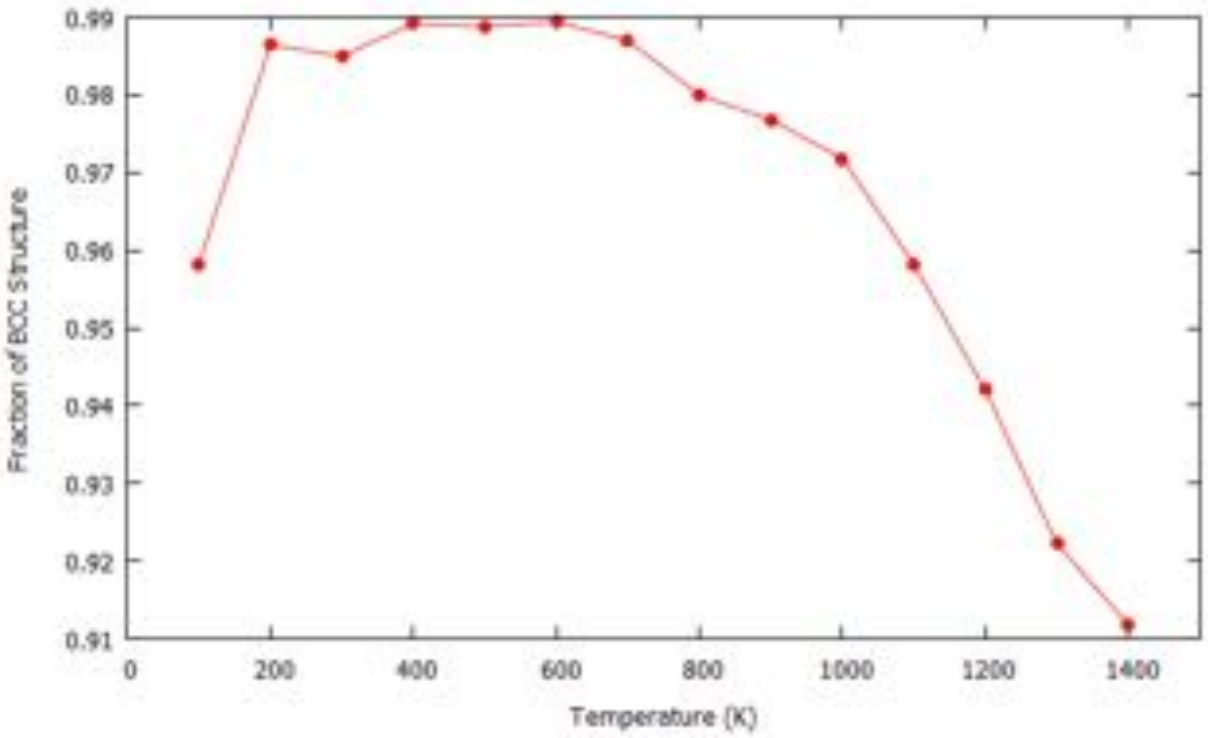

Figure 41: Fraction of Simulation in BCC Phase vs. Temperature for Pure Uranium

Radial Distribution Function

The Radial Pair Distribution Function measures the probability of finding a particle within a certain distance of any other particle. When plotted, the function tends to peak around the lattice constant, as one would expect. Unsurprisingly, the function tends to grow wider around the peak as temperature and atomic percentage of zirconium increases. Figures 42 through 53 below show select snapshots in order to illustrate this.

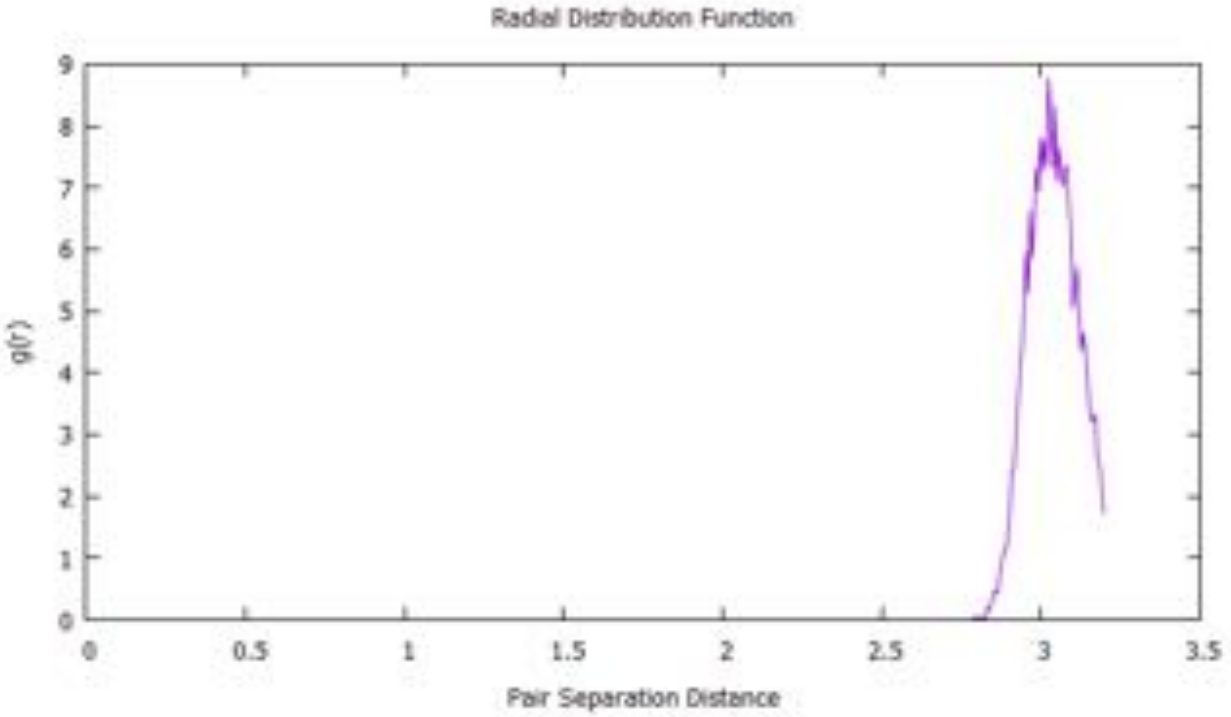

Figure 42: Radial Distribution Function for Zr-00% and 200 K

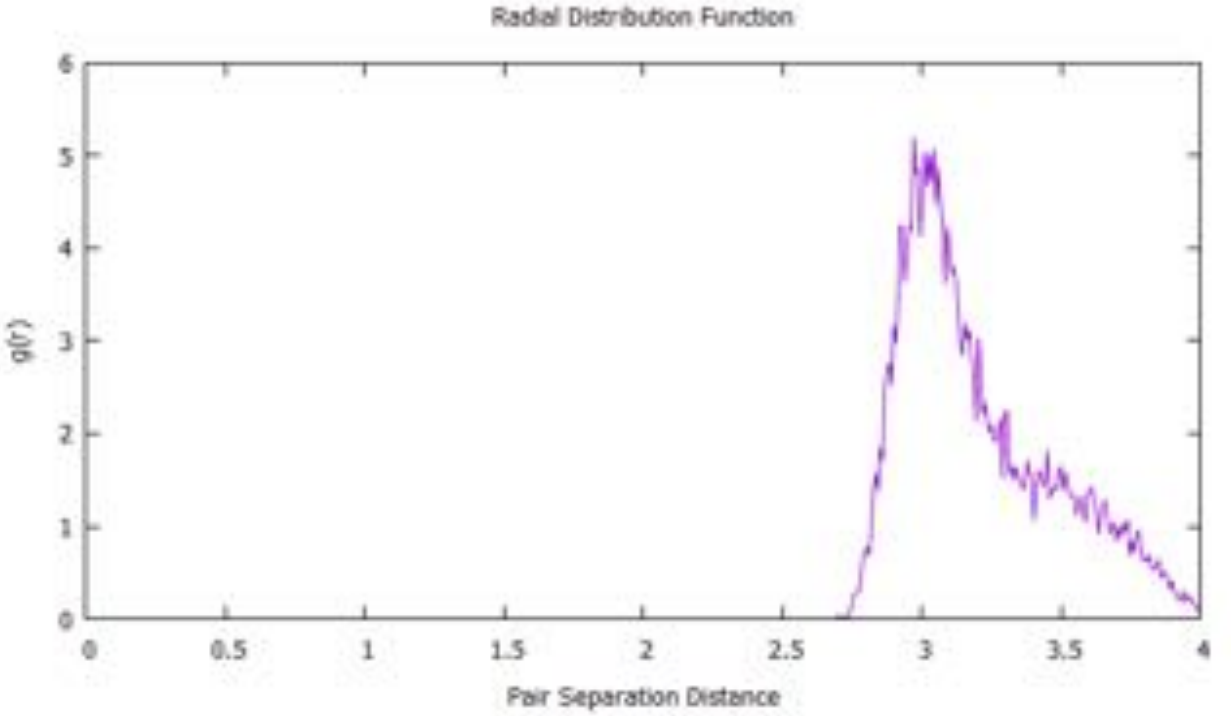

Figure 43: Radial Distribution Function for Zr-00% and 800 K

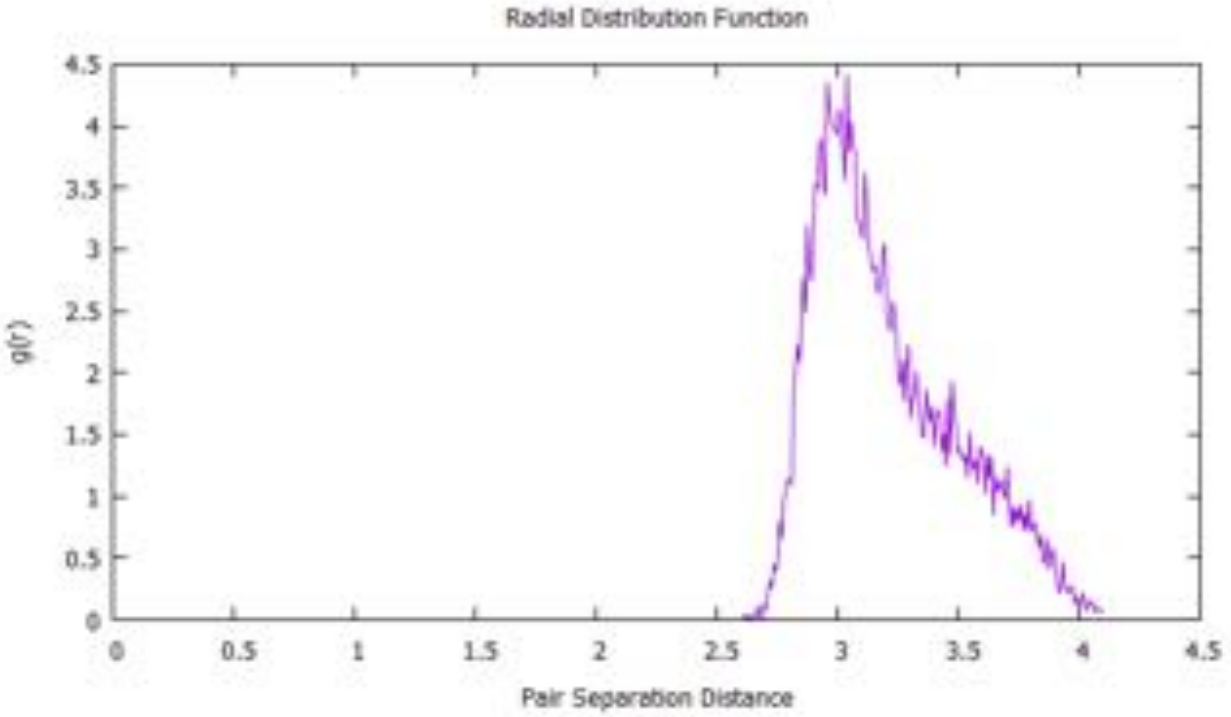

Figure 44: Radial Distribution Function for Zr-00% and 1300 K

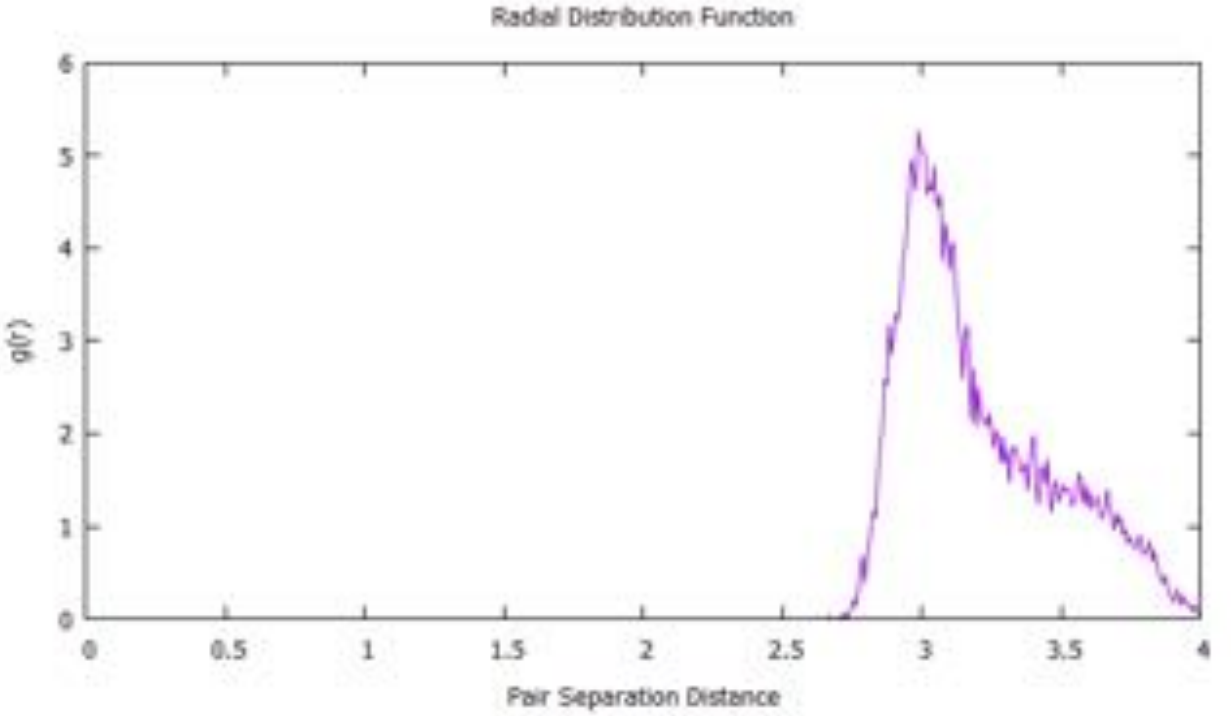

Figure 45: Radial Distribution Function for Zr-10% and 200 K

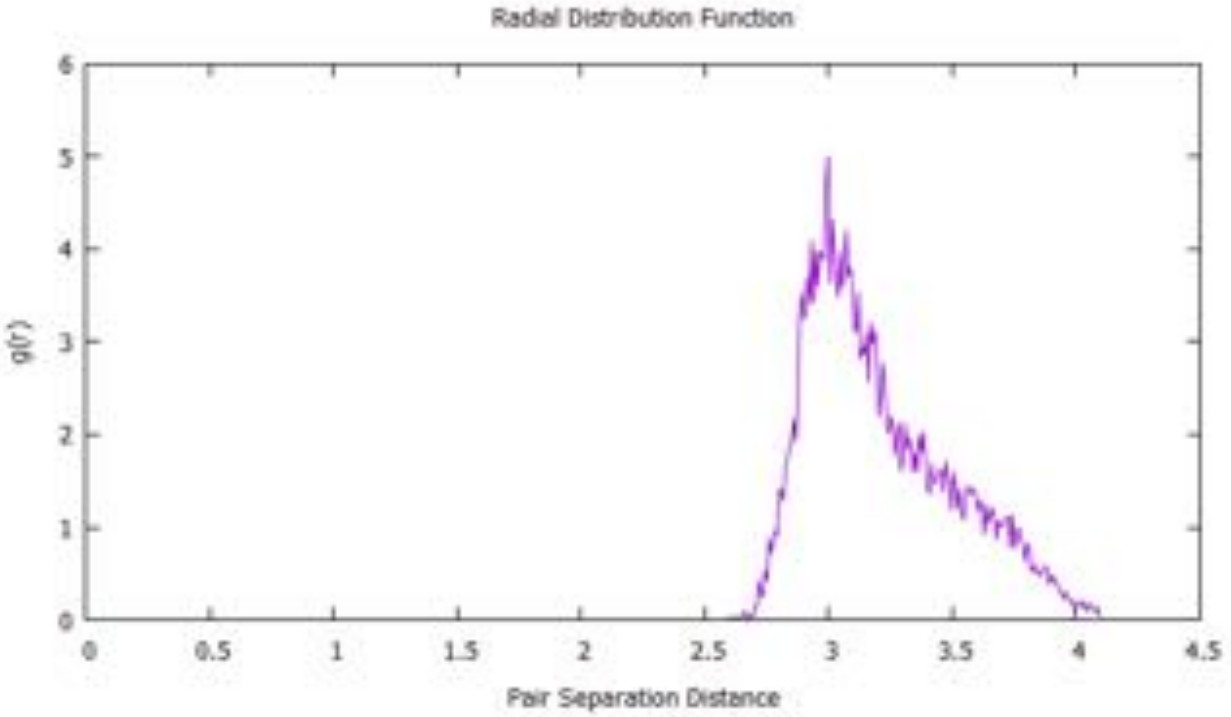

Figure 46: Radial Distribution Function for Zr-10% and 800 K

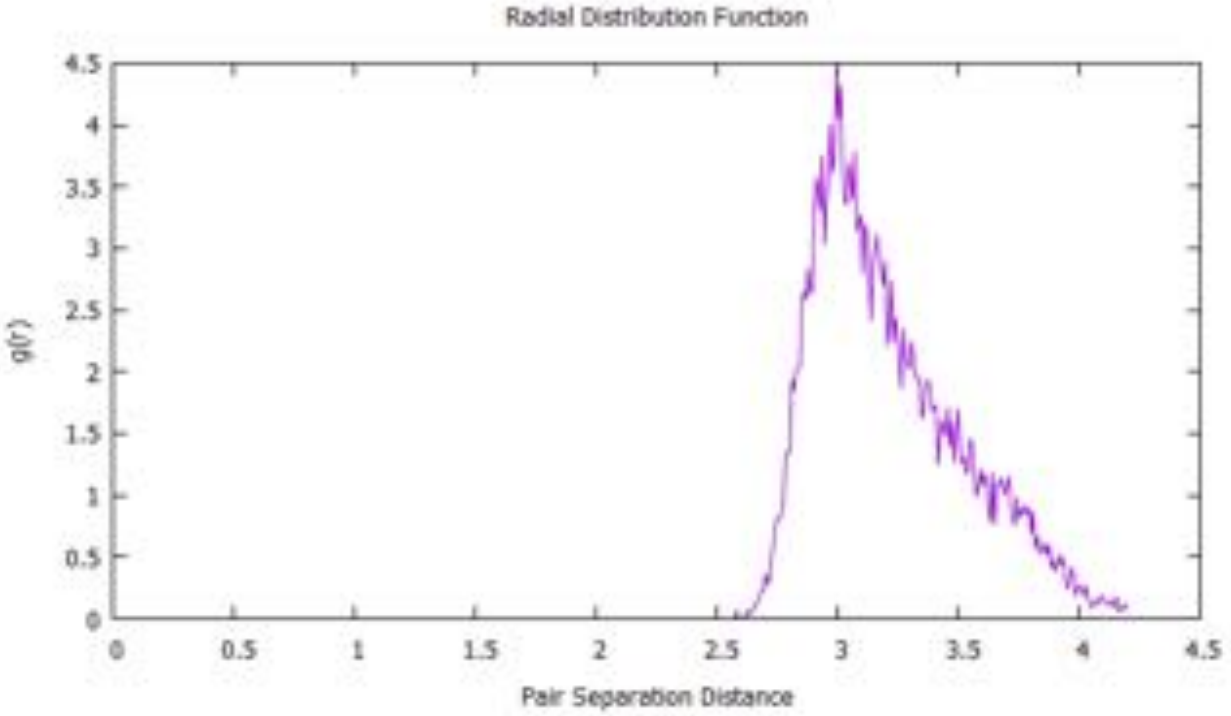

Figure 47: Radial Distribution Function for Zr-10% and 1300 K

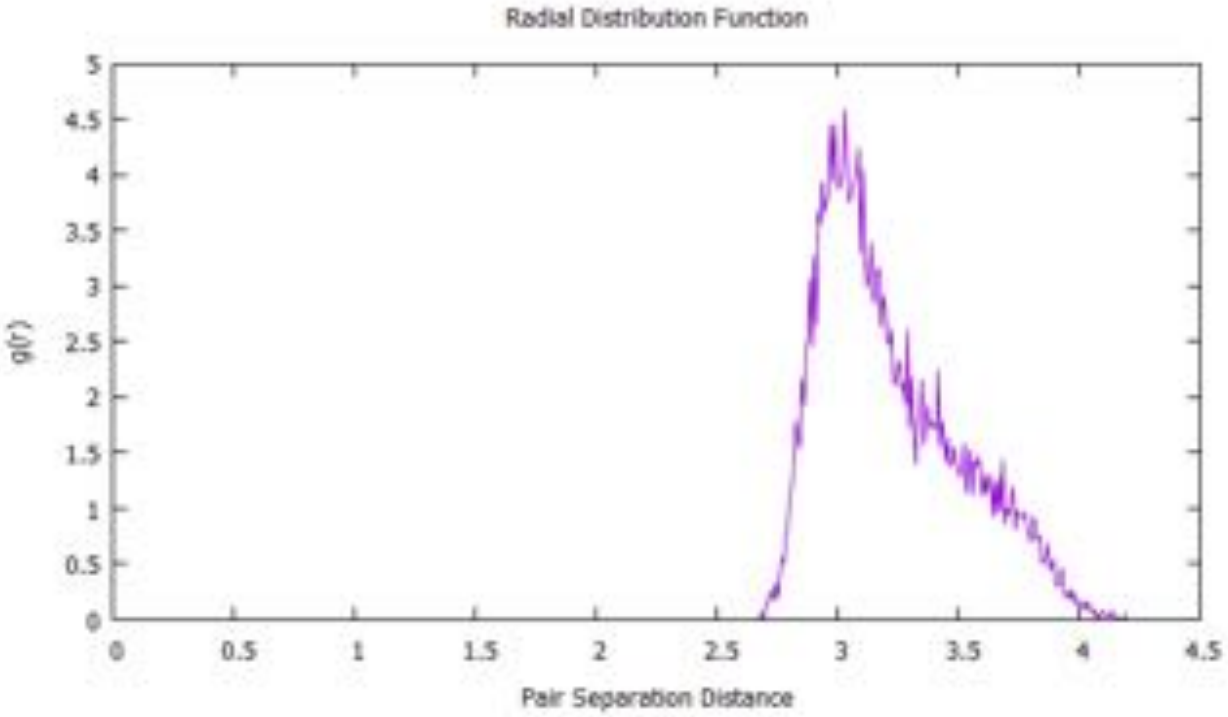

Figure 48: Radial Distribution Function for Zr-20% and 200 K

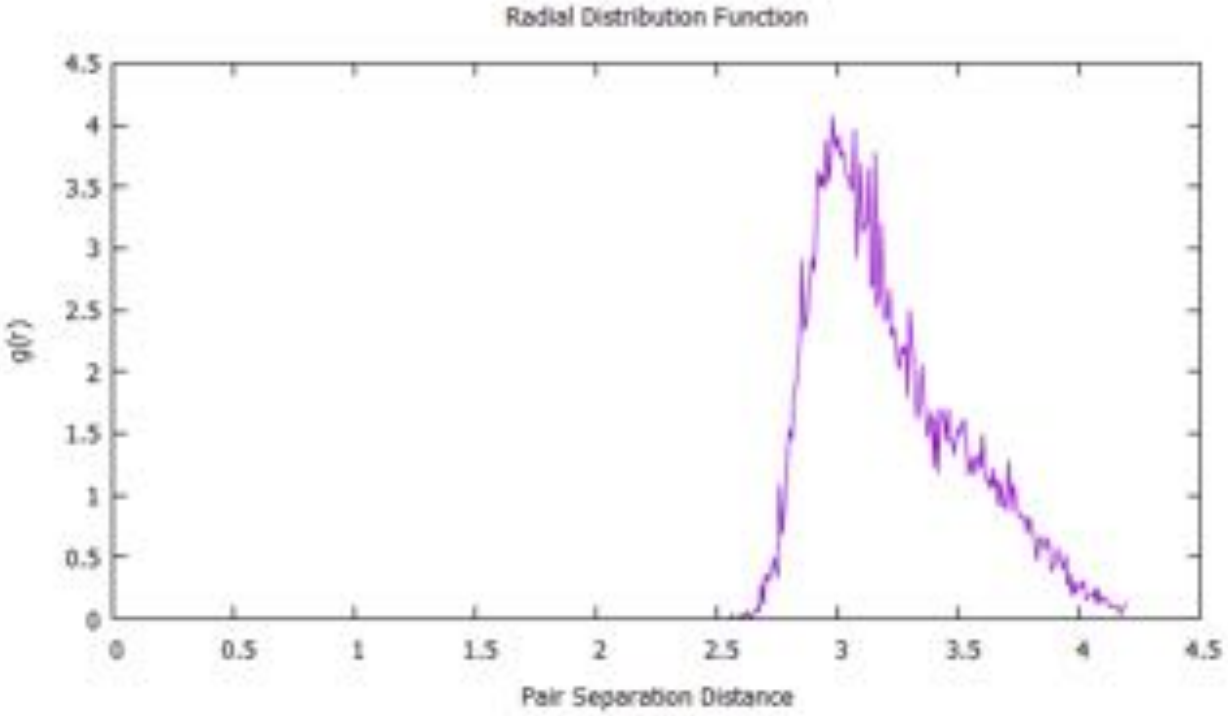

Figure 49: Radial Distribution Function for Zr-20% and 800 K

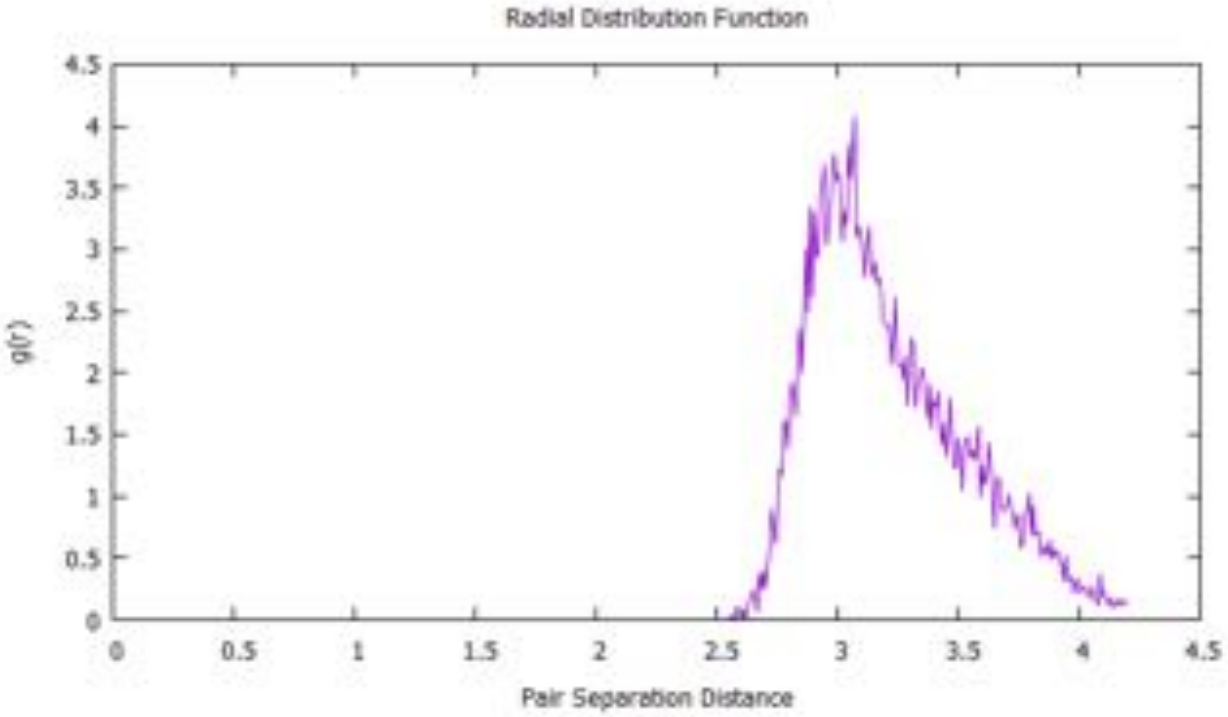

Figure 50: Radial Distribution Function for Zr-20% and 1300 K

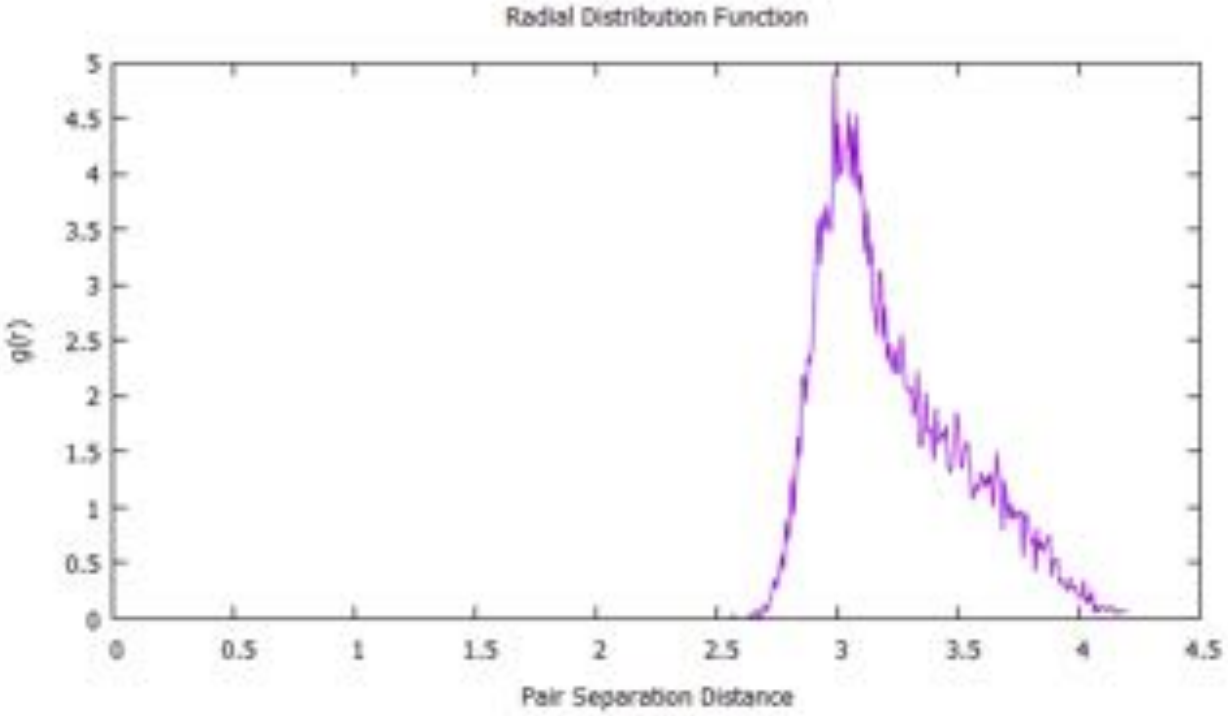

Figure 51: Radial Distribution Function for Zr-30% and 200 K

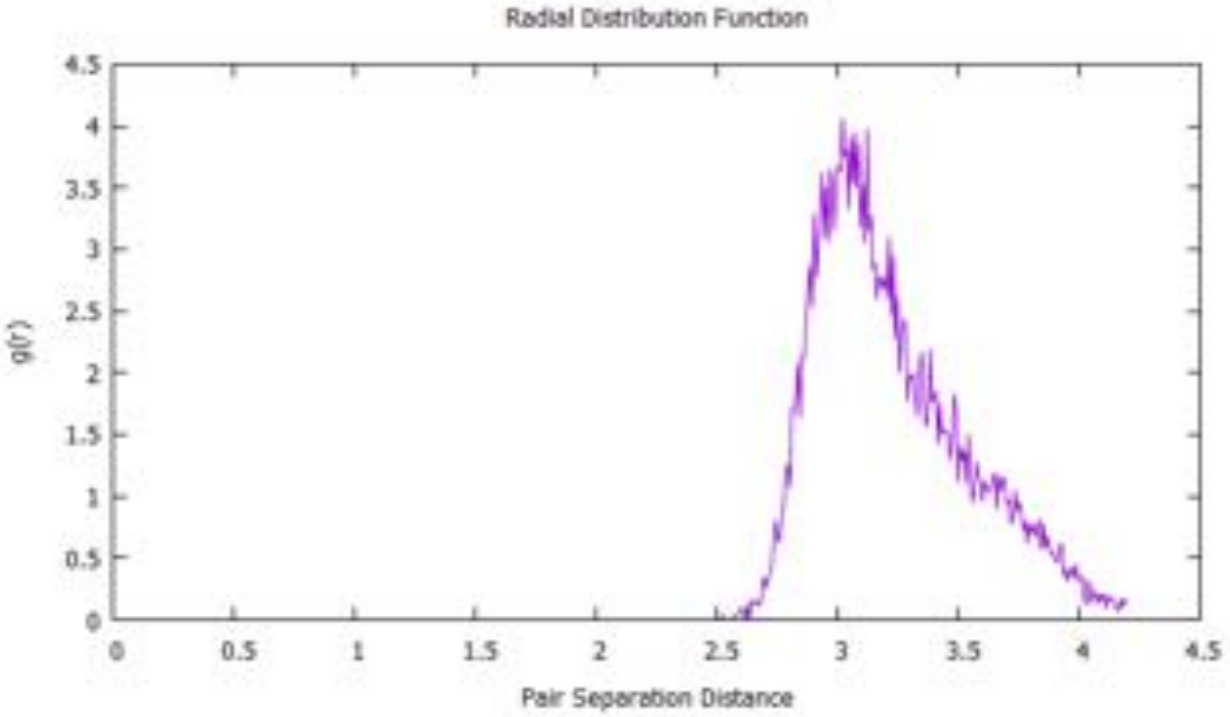

Figure 52: Radial Distribution Function for Zr-30% and 800 K

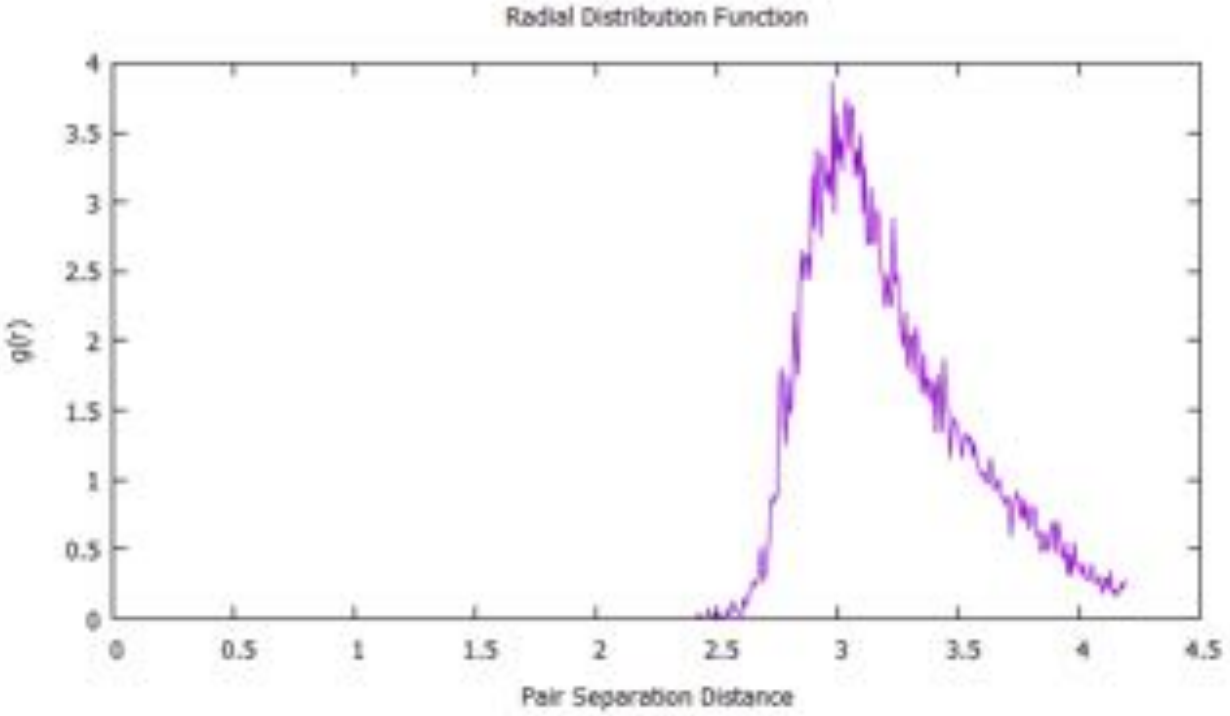

Figure 53: Radial Distribution Function for Zr-30% and 1300 K

Conclusion

With advanced reactor designs being pushed as the future of nuclear energy, finding the best fuel materials is of vital importance. One of the top candidates for advanced reactor fuel is the uranium-zirconium alloy. Despite the alloy's potential, a lot of data, even basic properties, has not yet been investigated and published. This work utilizes the Modified Embedded-Atom Method (MEAM) interatomic potential developed by Moore to continue collecting data on the BCC uranium-zirconium alloy, since reactor operating temperatures mean the alloy will be in the BCC phase. This MEAM interatomic potential is the first interatomic potential developed for the U-Zr alloy.

This work focused mostly on the U-Zr's vacancy formation energy, and found that, under the right circumstances, the MEAM interatomic potential seemed to do a good job of simulating the correct vacancy formation energy. In particular, these conditions were ones where the simulations were run at the correct temperatures for the BCC phase to exist, and also at the lowest percentages of zirconium. The vacancy formation energies found under these conditions are close to the vacancy formation energies of pure uranium and zirconium found in the literature. This follows Moore's conclusions that his MEAM interatomic potential best described majority-zirconium alloy; however, this is not much help as the alloys used in reactors will be majority uranium.

The vacancy formation energies that did not match predictions, however, did follow reasons found in literature for not following. First, at low temperatures, the BCC phase would not exist, so it makes sense the vacancy formation energy would often be negative. The other cases with a low or negative vacancy formation energy was predicted by the number of vacancy-

interstitial pairs, which affects the energy of the perfect lattice more, leading to the negative vacancy formation energy.

Besides the vacancy formation energy, several analysis techniques were performed on the simulations, giving a better idea of how well the lattice holds its phase during the short simulation. Again, lower amounts of zirconium and being at operating temperature both had an effect on the results, being attributable both to the MEAM interatomic potential's limitations and the formation of vacancy-interstitial pairs.

The MEAM interatomic potential could definitely use more work in various scenarios, but as a first step, does a good job describing other properties very well. With how important it seems the uranium-zirconium alloy will be going forward in the future, this work is a good step in the right direction for advanced reactor fuels.

REFERENCES

Beeler, Benjamin, et al. “First principles calculations of the structure and elastic constants of α, β, and γ uranium.” Journal of Nuclear Materials (2012a).

Hofman, G. L., S. L. Hayes, and M. C. Pietri. “Temperature gradient driven constituent redistribution in U-Zr alloys.” Journal of Nuclear Materials 227.3 (1996): 277-286.

Hünenberger, Philippe H. “Thermostat algorithms for molecular dynamics simulations.” Advanced Computer Simulation. Springer Berlin Heidelberg, 2005. 105-149.

L. C. Walters, B. R. Seidel and J. H. Kittel, Nucl. Technol. 65 (1984) 179.

Mendelev, Mikhail I., and Boris S. Bokstein. “Molecular dynamics study of self-diffusion in Zr.” Philosophical Magazine 90.5 (2010): 637-654.

Mendelev, Mikhail I., and Yuri Mishin. “Molecular dynamics study of self-diffusion in bcc Fe.” Physical Review B 80.14 (2009).

Moore, Alexander. *Computational Properties of Uranium-Zirconium.* MS Thesis. Georgia Institute of Technology, 2013.

Ogata, Takanari, et al. “Analytical study on deformation and fission gas behavior of metallic fast reactor fuel.” Journal of Nuclear Materials 230.2 (1996): 129-139.

Ogata, Takanari, et al. “Reactions between U-Zr alloys and Fe at 923 K.” Journal of Nuclear Materials 250.2 (1997): 171-175.

Okamoto, H. (2007). “U-Zr (Uranium-Zirconium).” Journal of Phase Equilibria and Diffusion 28(5): 499-500.

Ondracek, Gerhard, and Brigitte Shulz. “The porosity dependence of the thermal conductivity for nuclear fuels.” Journal of Nuclear Materials 46.3 (1973): 253-258.

Pahl, Porter, Crawford and Walters. Irradiation behaviors of metallic fast reactor fuels, Journal of Nuclear Materials 188 (1992) 3-9.

Pahl, R.G., et al. “Experimental studies of U-Pu-Zr fast reactor fuel pins in the experimental breeder reactor-II.” Metallurgical Transactions A 21.7 (1990): 1863-1870.

Steven L. Hayes and Douglas L. Porter, Fast Reactor Fuels, Nuclear Fuels and Materials Division Fuel Performance and Design Department, June 5, 2009.

W. M. Stacey, et al., “Resolution of Fission and Fusion Technology Integration Issues: An Upgraded Design Concept for the Subcritical Advanced Burner Reactor (SABR)”, Nuclear Technology (to be published).

Y. S. Kim, G. L. Hofman, S. L. Hayes, Y. H. Sohn, J. Nuc. Mat. 327 (2004) 27-36.